ISEL

ESCOLA SUPERIOR DE TECNOLOGIA DA SAÚDE DE LISBOA
INSTITUTO POLITÉCNICO DE LISBOA

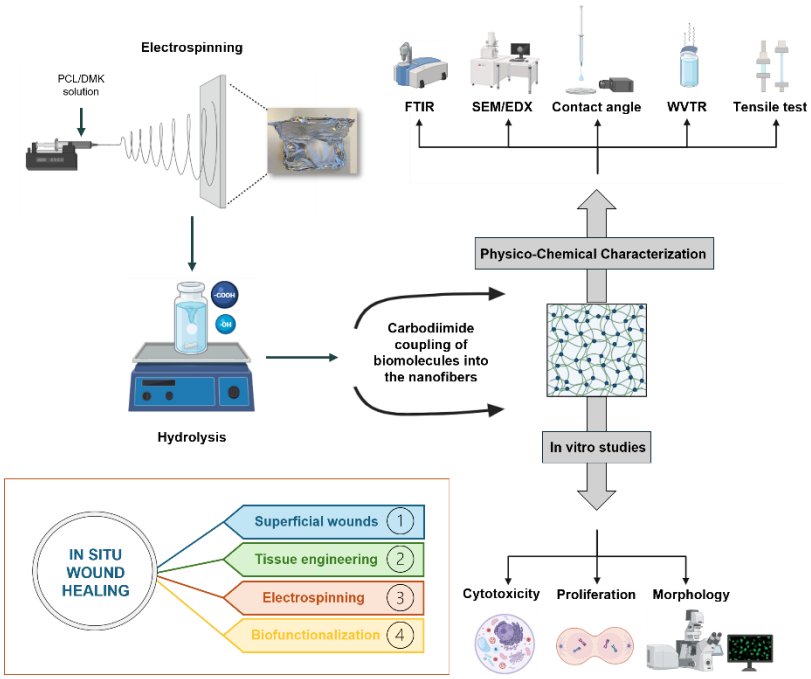

Biofunctionalization of electrospun meshes to promote skin regeneration

DANIELA ALEXANDRA CHAÍNHO GONÇALVES
(Licenciada em Biomecânica)

Dissertação para obtenção do grau de Mestre em Engenharia Biomédica

Orientadores:
Doutora Juliana Dias
Doutor Marco Araújo
Doutora Cecília Calado

Júri:
Presidente: Especialista Sérgio Rafael Reis Figueiredo
Vogais:
Doutora Tânia Vieira
Doutora Juliana Dias

Setembro de 2025

Biofunctionalization of electrospun meshes to promote skin regeneration

DANIELA ALEXANDRA CHAÍNHO GONÇALVES

(Licenciada)

Dissertação para obtenção do grau de Mestre em Engenharia Biomédica

Orientadores:

Doutora Juliana Dias, Instituto Politécnico de Leiria
Doutor Marco Araújo, i3S
Doutora Cecília Calado, ISEL - IPLisboa

Júri:

Presidente: Especialista Sérgio Rafael Reis Figueiredo, ESTeSL
Vogais:
Doutora Tânia Vieira, CENTIMFE – Centro Tecnológico da Indústria de Moldes, Ferramentas Especiais e Plásticos
Doutora Juliana Dias, Instituto Politécnico de Leiria

Setembro de 2025

Acknowledgements

To everyone who was part of this academic journey and to all the new people I met along the way as a master's student.

I am very grateful to the Centre for Rapid and Sustainable Product Development at the Polytechnic Institute of Leiria and to everyone there, as well as to the INOV.AM – WP14 project, which enabled me to complete this thesis. Special thanks to Dr Juliana Rosa Dias and her team for welcoming me with open arms, and especially to Sara Guerreiro and Nikoletta Varha for helping and motivating me on a daily basis.

To Dr. Marco Araújo for all his help during the optimization of protocols and characterization of the materials, and to Professor Dr. Cecília Calado, an excellent course coordinator who helped me throughout my master's studies.

Additionally, I would also like to thank my fiancé, Mário Jesus, for all the support and encouraging words, and for always being by my side throughout my academic career.

Thank you to all of them and many more.

Statement of integrity

I declare that this project work report is the result of my personal and independent research. Its content is original, and all sources listed in the bibliographic references were consulted and are duly mentioned in the text. I further declare that all scientific and technical references relevant to the development of the work are duly cited and included in the bibliographic references.

The author

Assinado por: Daniela Alexandra Chaínho Gonçalves
Num. de Identificação: BI15651643
Data: 08-12-2025 19:29:16 +00:00

CHAVE MÓVEL

Lisbon, September 2025

Biofuncionalização de malhas de *electrospinning* para promoção da regeneração da pele

Resumo

As malhas de poli(ε-caprolactona) produzidas por *electrospinning* têm propriedades promissoras para a cicatrização de feridas, mas evidenciam bioatividade limitada. Este estudo visa avaliar se a biofuncionalização com quitosano (CS), gelatina (Gel) ou arginina (Arg) pode otimizar o desempenho físico-químico e a resposta celular. Foram produzidas malhas por *electrospinning* e hidrolisadas para expor os grupos –COOH. Estas foram posteriormente funcionalizadas por carbodiimida com concentrações crescentes de cada biomolécula.

Procedeu-se às caracterizações físico-químicas (SEM/EDX, FTIR-ATR, taxa de transmissão de vapor de água, ângulo de contacto) e às propriedades mecânicas (módulo de Young, deformação e resistência à tração na rutura). A biocompatibilidade foi avaliada com fibroblastos L929 ao longo de 14 dias, tendo sido ainda examinadas a morfologia celular e a deposição de fibronectina.

Todas as biomoléculas foram imobilizadas com sucesso, sem afetar a porosidade da malha, que se manteve dentro da faixa pretendida (~60-90%). As taxas de transmissão de vapor de água foram mantidas em níveis relevantes. A hidrofobicidade da superfície foi melhorada, com Arg a produzir superfícies hidrofílicas em todas as concentrações e CS a 0,5 wt% a reduzir substancialmente a hidrofobicidade; Gel apresentou um efeito dependente da concentração.

Os testes mecânicos revelaram um endurecimento em concentrações moderadas de Gel e Arg, mas a deformação e resistência à tração diminuíram em relação às malhas não modificadas. Nenhuma formulação apresentou citotoxicidade. A atividade metabólica dos fibroblastos aumentou para todos os revestimentos em comparação com o ePCL, promovendo ganhos precoces no terceiro dia, enquanto o CS 0,1 wt% manteve a proliferação até ao 14º dia.

A biofuncionalização de CS, Gel e Arg no ePCL produziu estruturas com alta porosidade, permeabilidade ao vapor e interações celulares melhoradas. As malhas com CS 0,1 wt%, Gel 0,5 wt% e Arg 1 wt% foram os candidatos mais promissores para curativos avançados de engenharia de tecidos.

Palavras-chave: *electrospinning*; biofuncionalização; biomoléculas; cicatrização de feridas; poli(ε-caprolactona)

Biofunctionalization of electrospun meshes to promote skin regeneration

Abstract

Electrospun poly(ε-caprolactone) (ePCL) meshes offer promising wound-healing properties but suffer from limited hydrophilicity and bioactivity. This work explores whether covalent biofunctionalization with chitosan (CS), gelatin (Gel), or arginine (Arg) can enhance their physicochemical performance and cell response. Poly(ε-caprolactone) (PCL) was electrospun, hydrolyzed to expose –COOH groups, and functionalized using carbodiimide chemistry with increasing concentrations of each biomolecule.

Physicochemical characterization (SEM/EDX, FTIR-ATR, porosity/density, water vapor transmission rate, water contact angle) and mechanical properties (Young's modulus, elongation and tensile strength at break) were performed. Biocompatibility was assessed with L929 fibroblasts via indirect/direct contact and 14-day proliferation, as well as cell morphology and fibronectin deposition were examined by SEM/confocal microscopy.

All coatings were successfully immobilized without compromising mesh porosity, which remained within the tissue-engineering range (~60–90%). Water vapor transmission rates were preserved at clinically relevant levels. Surface wettability improved markedly, with Arg producing highly hydrophilic surfaces across all concentrations, while CS at 0.5 wt% also reduced hydrophobicity substantially; in contrast, Gel displayed a concentration-dependent effect, becoming hydrophobic at 1 wt%. Mechanical testing revealed moderate stiffening at intermediate Gel and Arg concentrations, although extensibility and tensile strength decreased relative to unmodified meshes. No formulation exhibited cytotoxicity. Fibroblast metabolic activity increased for all coatings compared with ePCL, with Gel (0.5 wt%) and Arg (1 wt%) promoting early gains at day 3, whereas CS (0.1 wt%) sustained proliferation through day 14.

Overall, biofunctionalization of CS, Gel, and Arg onto ePCL yielded scaffolds combining high porosity, favourable vapour permeability, and improved cell interactions. CS at 0.1 wt%, Gel at 0.5 wt% and Arg at 1 wt% offered the most balanced profiles, suggesting these coatings as promising candidates for advanced wound dressings.

Keywords: electrospinning; biofunctionalization; biomolecules; wound healing; poly(ε-caprolactone)

List of abbreviations

Arg	Arginine
CDRSP	Centre for Rapid and Sustainable Product Development
CLSM	Confocal laser scanning microscopy
CS	Chitosan
CuAAC	Copper-catalyzed azide–alkyne cycloaddition
DC	Direct contact
DMEM	Dulbecco's modified eagle medium
DMK	Dimethyl ketone
EDC.HCL	1-(3-Dimethylaminopropil)-3-ethylcarbodiimide hydrochloride
EDC/NHS	1-ethyl-3-(3-dimethylaminopropyl)carbodiimidehydrochloride / N-hydroxysuccinimide
EDX	Energy Dispersive X-ray Spectroscopy
ECM	Extracellular matrix
ePCL	Electrospun PCL
EB	Elongation at break
FN	Fibronectin
FTIR-ATR	Fourier Transform Infrared Spectroscopy with Attenuated Total Reflection
GA	Glutaraldehyde
Gel	Gelatin
IC	Indirect contact
LBL	Layer-by-layer

m_ePCL	Modified electrospun PCL
m_ePCL_Arg	Modified electrospun PCL with arginine
m_ePCL_CS	Modified electrospun PCL with chitosan
m_ePCL_Gel	Modified electrospun with gelatin
MIC	Minimum inhibitory concentration
NaOH	Sodium Hydroxide
NHS	N-hydroxysuccinimide
nm	Nanometres
NO	Nitric oxide
PBS	Phosphate buffered saline
PCL	Polycaprolactone
PDA	Polydopamine
RGD	Arg-Gly-Asp
SEM	Scanning Electron Microscopy
SPAAC	Strain-promoted azide–alkyne cycloaddition
TE	Tissue engineering
TSB	Tensile strength at break
WCA	Water contact angle
WHO	World Health Organization
WVTR	Water vapor transmission rate
YM	Young’s modulus

Table of contents

List of Figures

List of Tables

1. Introduction

The process of wound healing is a complex four-phase sequence of events initiated in response to injury to skin tissue. However, depending on factors such as wound size and/or the patient's health condition, therapeutic interventions may be required to support tissue regeneration [1]. The replacement, regeneration, or repair of tissue or organs due to ageing, disease, accidents, and birth defects continues to be a worldwide problem [2]. Chronic wounds are often defined as those that fail to heal within the expected time frame of 4–12 weeks, accounting for approximately 1-2% of the nation's population in developed countries [3,4]. The healing process can take several months to a year, and in certain cases, it may be even longer or may not heal completely, necessitating advanced intervention [5]. According to the World Health Organization (WHO), superficial wounds are further categorized into first- and second-degree burns. Annually, 11 million burn injuries are reported, with 12.8% classified as first-degree burns and 71.1% categorized as second-degree burns [6].

Conventional dressings for superficial wounds and burns remain the most common treatments, although they often result in delayed healing and may cause pain or even additional tissue damage [7]. Tissue engineered structures have thus been shown to possess regenerative potential in comparison to conventional approaches [1]. Electrospun meshes have been shown to have particular advantages as a wound dressing, due to their ability to mimic the native skin extracellular matrix (ECM), enhance hemostasis, absorb exudate, present semi-permeability, and provide superior wound conformity while reducing the risk of scar formation [8]. Electrospun fibers produced from synthetic polymers are typically more stable and mechanically robust in comparison to those produced from natural polymers, however, they lack the biological traces in their composition [9]. But also, producing natural fibers poses significant challenges, such as rapid degradation of the polymers and the need for additional cross-linking, which can alter the fiber morphology of the mesh [10,11]. Hereby, the objective of this work is to fabricate ePCL and to biofunctionalize their surfaces with CS, Gel, and Arg individually, leveraging their respective bioactivity to promote superior wound healing. These biomolecules of interest, CS, Gel and Arg, can confer antimicrobial activity to the mesh, enhance proliferation of the cells to the wound site, and confer hemostatic properties as well, respectively [12–14]. This strategy is designed to combine the mechanical robustness and processability of PCL with the biological cues provided by the functional polymers, thereby aiming for an ideal wound dressing material. The resulting structures were thoroughly characterized in terms of their physicochemical properties (including

fiber morphology, surface chemistry, and wettability), mechanical performance (such as Young's modulus (YM), tensile strength at break (TSB), and elongation at break (EB)), and in vitro studies (namely, cytotoxicity, proliferation and immunochemistry) in order to assess their suitability for biomedical applications.

The present project was developed at the Centre for Rapid and Sustainable Product Development (CDRSP), with the primary objective being the utilization of the electrospinning technique as a promising platform for the development of next-generation wound dressing.

2. State of the art

This chapter presents the essential concepts of skin and superficial wounds, providing an overview of their current treatments, limitations, and alternative treatments using tissue engineering principles. Superficial wounds, namely first- and second-degree burns, are the main concern of this project due to their wound healing limitation and worldwide prevalence.

2.1. Skin and superficial wounds

Skin is the largest organ of the human body in terms of surface area, and accounts for approximately 7% of total body weight [15]. This organ primarily serves to protect the body, acting as a physical and biological barrier from the external environment, namely pathogens, UV radiation, and physical trauma that can cause superficial wounds [16]. Skin has other purposes like regulating the internal body temperature, through sweat production and modulation of blood flow, as well as moisture retention, and metabolic activity through the synthesis of vitamin D, contributing to bone and immune health [15,16].

This tissue is constituted by three separate layers, as can be seen in Figure 1, each one with specific characteristics and functions.

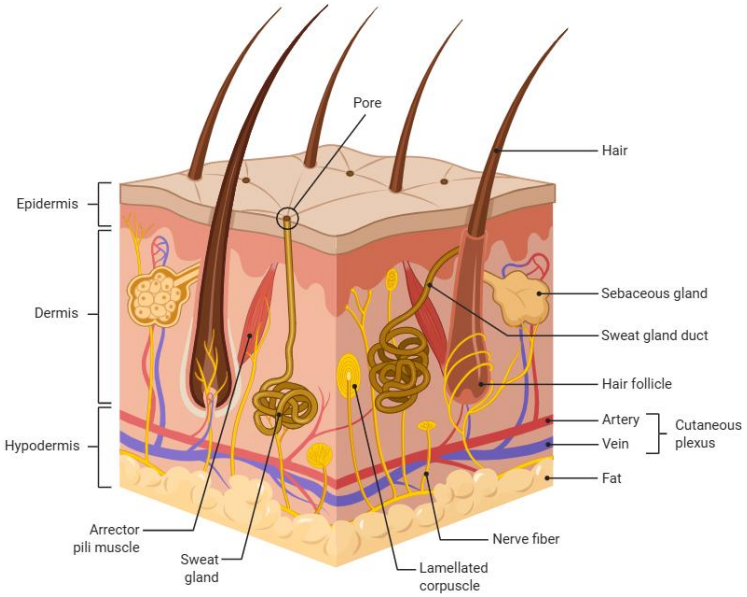

Figure 1 - Anatomy of the skin. Created by BioRender.com.

The most external layer is named the epidermis, which is a hydrophobic barrier that is rich in keratinocytes and melanocytes [17]. These cells provide defence against microbial and environmental damage, and produce melanin, giving the skin the ability to

protect itself from UV light [18]. Subjacent to the epidermis, the dermis constitutes the middle layer of the skin. The dermis is composed of collagen and elastin fibers, which provide structural integrity and elasticity. It also contains nerves that facilitate sensation, as well as blood and lymphatic vessels [19]. Additionally, the dermis is home to hair follicles and specialized glands, namely sweat and sebaceous glands, that play a role in thermoregulation, immune function, and exocrine secretion [20]. The final layer of the skin is the hypodermis, which is composed of subcutaneous tissue [17]. This deeper layer is responsible for the storage of adipose tissue, the accommodation of larger blood vessels, the maintenance of thermoregulatory functions, and the adhesion of skin to underlying tissues [17,21]

The skin is susceptible to injury due to constant exposure to the environment, so when an injury occurs, the skin as a highly coordinated sequence of biological events that restore the structural and functional integrity of the tissue, known as wound healing [15]. If the wound healing process occurs without any interruption, the sequence of events may be divided into five distinct phases: hemostasis, inflammation, migration, proliferation and maturation, which can also be called the remodelling phase, as illustrated in Figure 2 [8,21,22].

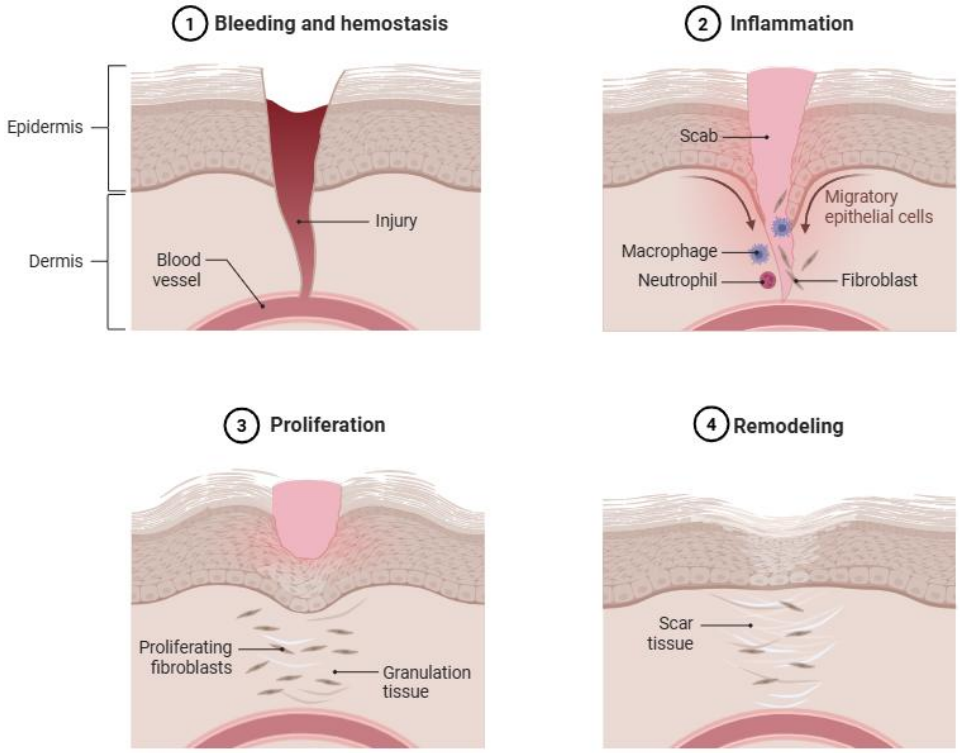

Figure 2 - Phases of wound healing: Hemostasis, Inflammation, Proliferation and Remodelling. Created by BioRender.com

There is an immediate response when an injury occurs, beginning with the hemostasis phase, where platelets aggregate to form a fibrin clot, to stop any bleeding

and establish a temporary matrix for cell migration. Furthermore, platelets also release growth factors and cytokines, which are essential for the initiation of the subsequent phases of wound healing [22,23]. During this phase, the inflammatory stage is initiated, during which neutrophils and macrophages migrate into the wound, clearing the injured area of any bacteria and dead tissue by phagocytosis. This phase is characterized by the prevention of infection and the establishment of an environment conducive to repair, which is achieved by the influx of additional immune cells. [22,24–26].

During the migration and proliferation phase, re-epithelialization occurs. This process entails the detachment of keratinocytes from the wound edge, followed by their migration over the provisional ECM to eventually cover the wound surface and re-establish the epidermal layer [15,22]. In this phase, the wound site experiences a fibroblast proliferation, leading to the synthesis of new ECM components, such as type III collagen and fibronectin. Lastly, endothelial cells are responsible for driving angiogenesis, the process by which new blood vessels are formed to supply oxygen and nutrients to the regenerating tissue [25,26].

The final phase of wound healing is intended to mature and strengthen newly formed tissue. This phase is known as the remodelling phase, and it can take weeks or even years to be fully completed [27]. Type I collagen deposition occurs, and myofibroblasts contract the wound and undergo apoptosis, leaving a more collagenous scar. In the majority of cases, the original architecture of the skin is not fully restored, which leads to the formation of scar tissue [28].

The wound healing process, from start to finish, can take 3 weeks up to a year, depending on the current health state of the patient and the environmental attributes, such as the wound's immediate surroundings, including local temperature, moisture balance, and cleanliness [25]. These attributes can lead to recurrent infections caused by microorganisms that can limit wound closure and cause more serious pathologies as well as the lack of biochemical cues [24,25].

Among the most common skin injuries are superficial wounds and burns, according to the WHO reports, 180,000 deaths occur on an annual basis as a result of burns [29]. There are several factors that can impact burn victims, such as environmental and economic attributes. According to the WHO, Asia has the highest incidence of burns globally, mainly due to population size and limited access to preventative resources [29]. Europe is one of the continents with the lowest prevalence of first- and second-degree burns, due to high safety standards, most accidents occurring from domestic incidents [29,30]. Figure 3 shows a more detailed global distribution of first- and second-degree burn incidence among all continents [29–31].

.

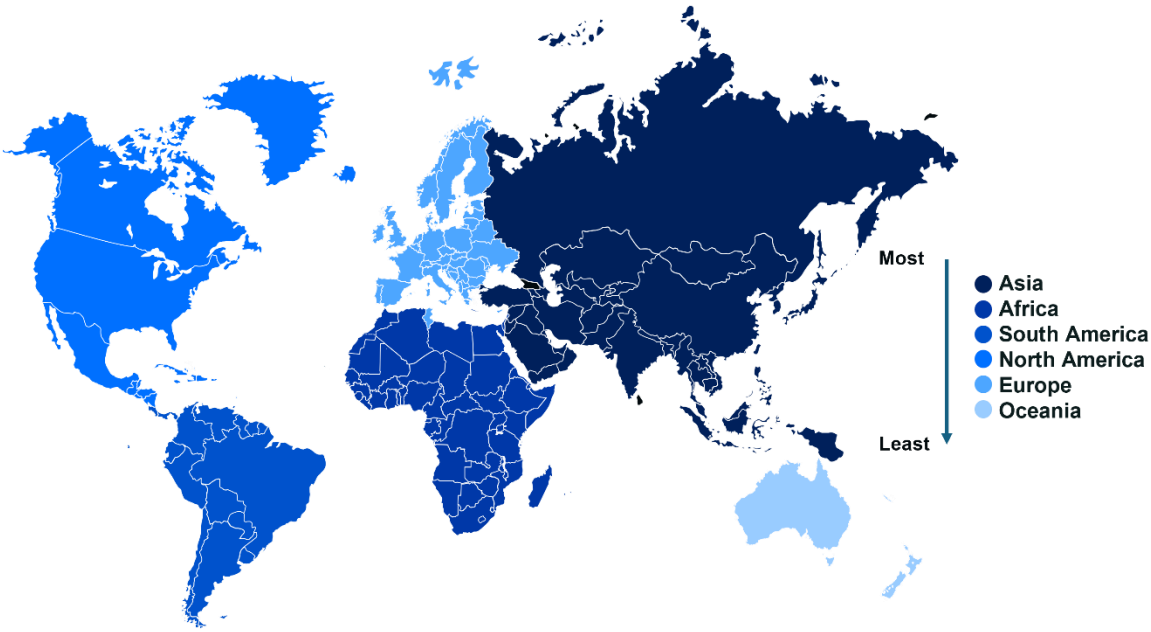

Figure 3 - Global distribution from most to least prevalence of first/second degree burns.

While often non-lethal, these injuries can have considerable ramifications for patients' well-being, quality of life, and healthcare costs [32]. Superficial wounds generally exhibit a high rate of healing efficiency, attributable to the skin's rapid regenerative capacity. Nonetheless, extensive superficial wounds of the epidermis and upper dermis cover a significant surface of the body. Extensive superficial wounds can include large abrasions or friction burns, often resulting from trauma or an accident. While not deep, their wide coverage increases the risk of fluid loss, infection, and delayed healing, and may require more intensive wound care to maintain a moist, clean, and protected environment during the healing process [33,34].

2.2. Current therapies and limitations

For superficial wounds and burns, traditional treatments, such as topical ointments and conventional dressings, are still widely used, although, they often fall short in promoting rapid and scar-free healing, especially in complicated or chronic cases [35]. Wound dressings like gauze, films, or gels are an example, although dry dressings can cause pain to the patient when removed as well as tissue damage, causing a regression in the wound healing process, since they have to be exchanged once every one or three days [25].

There are also skin regenerative products, such as skin grafts, that are used as a last resort for these types of injuries. They are harvested from a specific site on the donor and then applied to the affected area [36]. Once applied, the graft restores skin continuity and promotes essential regeneration mechanisms, such as angiogenesis release [36]. These grafts can be made from tissue taken from the patient with the wound

(autografts), from a compatible donor (allografts), or from an animal for implantation in the wounded patient (xenografts) [15].

Transplantation is the most common therapy response to the replacement, regeneration or repair of tissue. However, the application of these dressings has major limitations in terms of the extent to which they influence the wound healing process. The use of grafts is also highly dependent on their scarcity and the risk of complications during application as it often involves high costs associated with the activity and the high level of specialization required of health professionals [37]. The techniques related to transplanting tissues or organs are complex and have various limitations, including the difficulty in finding compatible donors, resulting in long waiting lists, the high rate of rejection by the recipient as well as potential disease transmission and the morbidity involved for the living donor [15,38].

2.3. Alternative therapies

Nowadays, various alternative therapy techniques are being studied across de globe for wound healing. Nevertheless, *in situ* therapy is perhaps the most suitable option [2]. *In situ* therapy is administered directly at the site of injury, offering several advantages. Primarily, it allows for the targeted delivery of healing agents or drugs, reducing the risk of systemic absorption, as is often the case with oral medications [39,40].

Tissue engineering (TE) has thus emerged over the past two decades as a promising field, involving the combination of biomaterials, cells, and growth factors to recreate functional tissue substitutes to provide structural support for cell adhesion and subsequent tissue development [41,42]. TE is a promising approach to organ and tissue regeneration, through the culture of the patient's cells in biological substitutes (scaffolds) and implantation in the patient to regenerate the new tissue. TE-based products have been rapidly growing, giving their customizability and adaptability depending on the specificities of the wound [43]. These wound dressings are made to be biocompatible, maintain the wound's moist microenvironment and prevent further skin damage.

TE-based products can be produced using a variety of biofabrication techniques, including bioprinting and electrospinning, to name a few [44]. The application of these techniques in TE depends on the type and state of the material being handled as well as the objective of the application. However, the number of techniques capable of processing materials that mimic skin tissue is limited. Given that these dressings need to be able to allow oxygen permeation, therefore, they need to be porous, due to this reason and their similarity to the ECM, as well as biomechanical properties, these dressings are produced using the electrospinning technique [24,33].

2.3.1. Electrospinning

Among the various fabrication techniques, electrospinning is distinguished by its capacity to produce nanofibrous meshes that structurally and functionally resemble the ECM of native skin, thereby offering a favourable microenvironment for cell migration and proliferation [45,46]. ECM fibers have a diameter between 10 and 300 nanometres (nm), while nanofibers produced by electrospinning have a diameter between 50 and 1100 nm, as illustrated in Figure 4.

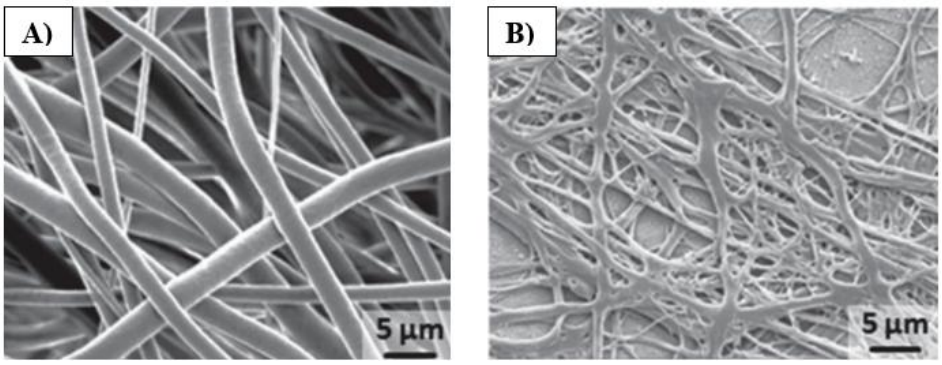

Figure 4 - A) Fibers produced using the electrospinning technique; B) Natural ECM of the human skin. Adapted from [47].

Electrospun meshes also exhibit high porosity, rendering them permeable, and a large surface area to facilitate efficient exchange of gases, fluids, and nutrients across the material, as well as moisture balance, and exudate absorption [35]. All of these attributes are essential for applications as wound dressings, as electrospun nanofiber wound dressings have been shown to enhance hemostasis and establish superior wound conformity [8].

The electrospinning technique consists of 3 main components: a high-voltage system, a syringe pump, and a collector [15]. The pump is fitted with a syringe containing a solution of polymeric material, which is pumped at a controllable feed rate through the needle. To start producing the mesh, the voltage source is connected to the needle and the collector, therefore the opposing electrostatic forces overcome the surface tension of the solution used. The polymer solution undergoes rapid solvent evaporation at the same time that polymeric entanglements occur, during its trajectory from the needle tip to the collector, enabling the continuous deposition of solid fibers. These fibers, now charged with energy, are deposited on the collector as shown in Figure 5 [48,49]. The alignment of these fibers is dependent on the particular collector used, since they may be deposited in a random (static collector) or an aligned manner (drum collector).

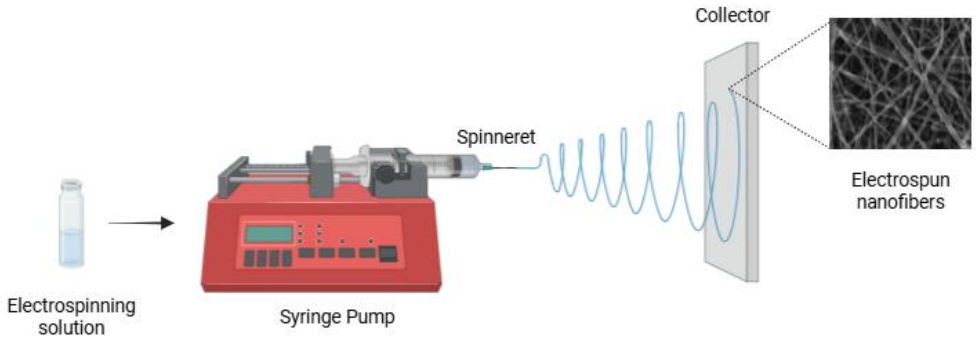

Figure 5 – Conventional electrospinning setup.

In order to obtain meshes that are homogeneous and as close as possible to human skin ECM, it is necessary to optimize several factors [50]. The three principal sets of parameters for optimizing production are the solution, processing and environmental conditions [51]. The formation and final characteristics of the fibers are strongly influenced by several solution properties, including viscosity, surface tension, electrical conductivity, and dielectric behaviour [52]. The effects of these factors range from determining fiber formation to reducing the formation of beads and drops. In the context of processing, four sub-parameters must be considered: the applied tension, the flow rate at which the solution exits, the needle diameter, and the distance from the needle to the collector [52]. The morphology, size, geometry and porosity of the meshes produced are influenced by all these factors. Finally, environmental conditions have been identified as a pivotal factor in the efficacy of the technique, with particular attention being drawn to the atmosphere, pressure, temperature, and humidity [53]. It is therefore vital to exercise control over the last two factors, since an increase in temperature accelerates the solvent's evaporation rate and elevated humidity levels have the potential to induce changes in morphology [54].

Electrospinning is a technique that has existed since the 1600s, but only in the late 1900s has it led to major discoveries, such as the use of organic polymers in the production of nanofibers [55]. However, the incorporation of natural materials during electrospinning processes often yields heterogeneous outcomes. Furthermore, several other challenges must be given due consideration [50]. These include the limited availability of solvents capable of dissolving natural materials, combating the rapid degradation of the natural polymers, and the often necessary additional cross-linking, which can deform the morphology of the structure [11,50]. Furthermore, some natural polymers are not suitable for processing via electrospinning [56].

2.3.2. Surface biofunctionalization

The objective of surface biofunctionalization is to immobilize biomolecules at the fiber interface, such as ePCL meshes, with specific biological functions while preserving

their morphology and porosity. The most efficacious routes are characterized by mild, aqueous conditions, the formation of chemically stable linkages, and the avoidance of unwanted pore occlusion or loss of activity [57,58]. The principal strategies employed in electrospun systems include catechol-based priming (polydopamine), layer-by-layer (LbL) assembly of polyelectrolytes, bioorthogonal "click" conjugations, aldehyde/Schiff-base coupling, and carbodiimide (EDC/NHS) chemistry [59,60].

Polydopamine (PDA) coatings have been demonstrated to offer a versatile method of coating that does not require the use of organic solvents or multiple chemical activation stages. Dopamine auto-oxidizes at mildly alkaline pH to form a PDA film that adheres broadly and presents catechol/quinone groups capable of Michael addition or Schiff-base reaction with amine/thiol-bearing biomolecules. On ePCL, PDA coatings have been shown to reproducibly increase wettability and support covalent immobilization of peptides, growth factors and polysaccharides. However, overdeposition has been observed to result in the darkening of fibers and the narrowing of pores. Recent studies have documented these effects and processing windows [61,62].

Layer-by-Layer (LbL) assembly immobilizes biomolecules by alternating the adsorption of oppositely charged polyelectrolytes (e.g., chitosan/alginate, gelatin/heparin), thereby enabling tunable loading/release while retaining the fibrous architecture. Electrostatic bonds are known to be susceptible to the effects of ionic strength and pH, as a result, post-stabilization techniques (for example, mild crosslinking) are frequently employed to ensure long-term stability [63].

The technique of click chemistry has also been adapted for the biofunctionalization of electrospun meshes, offering highly selective and bioorthogonal reactions that proceed under physiological conditions. Typical examples include the copper-catalyzed azide–alkyne cycloaddition (CuAAC), its catalyst-free variant strain-promoted azide–alkyne cycloaddition (SPAAC), and thiol–ene coupling. These reactions facilitate the efficient conjugation of biomolecules while preserving their bioactivity. Moreover, when ligands are site-specifically modified, they can even enable oriented immobilization. Despite these advantages, click chemistry presents several limitations in the context of ePCL scaffolds. Firstly, it is important to note that the native polymer surface does not contain azide, alkyne, or thiol groups. This means that additional pre-functionalization steps are required, which increases time and processing complexity. Secondly, CuAAC relies on copper (I) catalysts that are cytotoxic, meaning they must be thoroughly removed before biomedical use. These drawbacks make click chemistry less straightforward and more resource-intensive than alternative approaches, which can be applied directly after simple surface activation [64,65].

The process of aldehyde/Schiff-base coupling is a well-established method in this field. For instance, aldehydes resulting from glutaraldehyde (GA) treatment or

polysaccharide oxidation react with amines to form imines. They can undergo reduction, yielding secondary amines [66]. Despite its efficiency, the use of residual glutaraldehyde gives rise to concerns regarding its biocompatibility [67]. Furthermore, in the event of cessation of the Schiff base formation and subsequent absence of reduction, there is the possibility of gradual detachment of the biomolecule from the scaffold, whether in water or under cell culture conditions [66].

Carbodiimide or 1-ethyl-3-(3-dimethylaminopropyl)carbodiimidehydrochloride/N-hydroxysuccinimide (EDC/NHS) reaction is a very commonly used coupling reaction since it is highly efficient and an accessible grafting method [68]. Briefly, a carbodiimide, such as EDC, activates a carboxyl group, forming an unstable O-acylurea intermediate that reacts with an amine to produce an amide bond. The NHS is simultaneously added to improve stability and reduce side reactions [69]. This method covalently links amine-bearing ($-NH_2$) biomolecules to carboxylated fiber surfaces (e.g., after alkaline hydrolysis of PCL) via amide bond formation, as can be observed in Figure 6.

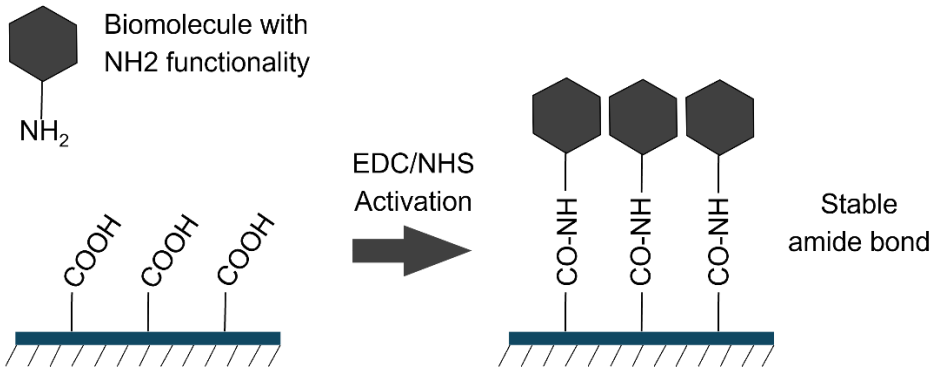

Figure 6 - Visual representation of carbodiimide coupling forming an amide bond.

However, in order to chemically attach biomolecules to the surface of an ePCL mesh, it needs to be hydrolyzed. This process, known as alkaline hydrolysis, breaks the ester bonds in the PCL chain, resulting in the formation of carboxyl groups (-COOH) and hydroxyl (-OH) groups [70].

Compared with PDA and LbL, EDC/NHS yields catalyst-free, aqueous, and hydrolytically stable amide linkages that are less susceptible to ionic instability or desorption. When compared with click reactions, it typically requires fewer preparatory steps and no metal catalysts, simplifying translation and preserving biomolecule structure when pH/time are controlled.

2.3.3. Biomolecules

In TE, the integration of biomolecules into scaffolds has emerged as a pivotal strategy to enhance biological performance and to modulate cellular responses. Biomolecules can provide specific biochemical cues that stimulate adhesion,

proliferation, differentiation, and tissue regeneration [71]. In addition to this, they can also confer additional functionalities such as antimicrobial activity, angiogenesis, or modulation of the immune response [72]. The integration of these elements into polymeric scaffolds fosters bioactive environments that more accurately replicate the ECM and thereby enhance interactions between the material and surrounding tissues [73]. A wide range of biomolecules, including polysaccharides, proteins, and amino acids, have been the subject of investigation for these purposes. Among the most widely explored are CS, Gel and Arg, each of which presents unique bioactive properties and versatile applications in regenerative medicine and wound healing [74–76].

2.3.3.1. Chitosan

CS is a biodegradable polysaccharide derived by partial chemical deacetylation, which is the second most abundant natural biopolymer found mainly in the shells of shellfish and crustaceans, known as chitin [77]. CS can promote clotting, as well as confer antimicrobial properties through its positively charged amino groups that interact with blood cells and bacteria [14,49]. CS is widely used in TE for its high adsorption capacity, excellent biodegradability, biocompatibility and non-cytotoxicity and is shown to influence all stages of wound repair by stimulating inflammatory cells, macrophages, and fibroblasts during the inflammatory phase [49,77].

2.3.3.2. Gelatin

Gel can mimic the basic constituents of the ECM [13]. Gel is a water-soluble protein derived from partial hydrolysis of collagen and typically requires crosslinking to enhance mechanical properties and stability [8]. Because it derives from collagen, it contains the Arg-Gly-Asp (RGD) sequence of amino acids that promotes the adhesion, migration, and proliferation of cells [22]. Gel stands out for its natural hydrogel structure, low cytotoxicity, excellent biocompatibility, biodegradability, commercial availability, and non-immunogenicity, making it increasingly used as a scaffold material in TE and in vitro cell culture [13,78].

2.3.3.3. Arginine

Arg has been used as a bioactive agent for wound healing due to its specific biological activity, since it plays a central role in the regulation of vascular homeostasis and wound healing by regulating immune response, promoting vasodilation, increasing vascular permeability, and promoting collagen deposition functions as well [79]. The slow release of Arg is used to achieve antimicrobial and anti-inflammatory activity and enhance angiogenesis through migration, proliferation, and differentiation of endothelial cells [22,80].

Due to these properties, Arg is highly used in oral supplementation, however, at high concentrations, it may have adverse effects [81].

3. Materials and Methods

3.1. Materials

PCL (Mw: 50.000 (g·mol−1), bulk density: 1.1 g·cm^{-3}) purchased from Perstorp (Malmo, Sweden) was dissolved in acetone (DMK, ≥99.8%, Mw: 58.01 (g·mol−1)) purchased from Carlo Erba Reagents (France) and used without any further purification. Sodium hydroxide (NaOH, Mw: 40 (g·mol−1) purchased from LabChem (Zelienople, USA).

Carbodiimide coupling was performed using 1-(3-Dimethylaminopropril)-3-ethylcarbodiimide hydrochloride (EDC.HCL, Mw: 191.70 (g·mol−1)) and N-hydroxysuccinimide (NHS, Mw: 115.09 (g·mol−1)) both obtained from Sigma-Aldrich (St. Louis, USA).

CS (Mw: 100,000–300,000 (g·mol^{-1}), ≥75% deacetylation, bulk density: 0.15 g·cm^{-3}) obtained from ACROS Organics™ (Geel, Belgium) was dissolved in hydrochloric acid (HCL, 2.5 L, Mw: 36.46 (g·mol^{-1})) obtained from Honeywell Fluka (Charlotte, USA). Gel (Porcine skin, type A, 300 Bloom, 60 mesh, bulk density: 0.72 g·cm^{-3}) purchased from Sigma Aldrich was dissolved in MilliQ Water. 2-Propanol (≥99.9%, Mw: 60.00 (g·mol^{-1})) purchased from Carlo Erba Reagents. Arg (≥98%, Mw: 174.20 (g·mol^{-1}), bulk density: 1.3 g·cm^{-3}) obtained from ThermoFisher (Kandel, Germany) was dissolved in MES hydrate (MES, ≥99.5%, Mw: 195.24 (g·mol^{-1})) obtained from Sigma-Aldrich.

Biomolecule attachment efficiency was assessed using NHN powder (Mw: 178.14 (g·mol^{-1})), also obtained from Sigma-Aldrich.

Antimicrobial activity was performed with Luria Bertini broth (L.B. Medium) was acquired from Liofilchem® (Via Scozia, Roseto degli Abruzzi, Italy). Luria Bertani Agar, Miller (Miller Luria Bertani Agar, M1151-500 G) was purchased from HiMedia® (Laboratories Private Limited, Thane West, Maharashtra). The bacteria used was *Escherichia coli* (*E. Coli*, ATCC 8739) and *Staphylococcus aureus* (*S. aureus*, ATCC 6538P).

Cell culture was performed with Dulbecco's modified eagle medium (DMEM) – high glucose, supplemented with 10 % (v/v) of fetal bovine serum (FBS), 1 % (v/v) of penicillin-streptomycin (P/S), and 1 % (v/v) of amphotericin B (Fungizone). For cell detachment, a trypsin-EDTA solution (0.25% trypsin/0.05% ethylenediaminetetraacetic acid/ 0.1% glucose in phosphate buffered saline (PBS, pH 7.4)) was used. All the reagents mentioned above were purchased from Sigma-Aldrich.

Cell line L929 (Areolar mouse fibroblast) was purchased from ATCC (Gaithersburg, USA).

Resazurin sodium salt was obtained from Sigma Aldrich. The reagents used in cell morphology analysis, including glutaraldehyde (GA; 111-30-8; Grade I; 25% in H_2O) and Triton X-100 purchased from Sigma-Aldrich. Also included bovine serum albumin (BSA, Merck, New Jersey, USA) in PBS. For fibronectin (FN) staining, rabbit anti-fibronectin (f3648, Sigma-Aldrich, Missouri, USA, 1:300) was used and goat anti-rabbit secondary antibody Alexa Fluor® 488 F(ab′)2 fragment (Molecular Probes-Invitrogen, California, USA, 1: 2000). A conjugated probe of phalloidin/Alexa Fluor® 594 (Molecular Probes-Invitrogen, California, USA, 1: 40) was used for F-actin staining. For nuclei staining, 40,6-diamidino-2- phenylindole dihydrochloride (DAPI, Sigma-Aldrich,1 mg·mL−1) in Vectashield (Vector laboratories, California, USA) was used.

3.2. Methods

3.2.1. Electrospun Mesh Preparation and Modification

The desired meshes were manufactured using the electrospinning technique. To produce them, a solution of 16 wt% PCL/DMK was prepared by dissolving the polymer and stirring it at 37°C overnight at 250 rpm. The prepared solution was placed in a syringe and released through a 22-gauge needle (inner diameter - 0.4 mm; outer diameter - 0.7 mm). The samples were produced in a homemade electrospinning equipment, with a constant flow rate of 0.8 $mL \cdot h^{-1}$ (syringe pump model SP11Elite Series, Harvard Apparatus, Stafford, USA), a distance between the syringe and the grounded cooper collector of 15 cm and 18 kV of voltage (high voltage source, Genvolt 73030 model, Bridgnorth, UK). The collector was lined with aluminium foil to facilitate the removal of the mesh. An average temperature of 22°C was maintained during the production process. A single electrospun mesh production was completed after 30 min.

Samples of ePCL were cut to 8.5 mm in diameter and selected by weight to reduce heterogeneity in the samples. The selected range was [0.7 – 1.2] mg, the measurements were performed with a microbalance (Sartorius, Goettingen, Germany). When other geometries were needed, the weight ratio per area was calculated.

After selecting the samples, the following step was the hydrolysis of the ePCL (m_ePCL) fiber's structure. Briefly, this process exposes their carboxylic (-COOH) and hydroxyl (-OH) groups. Hydrolysis was achieved by immersion in a 3M NaOH solution for 3h at 37°C, at 200/250 rpm. Modified ePCL (m_ePCL) meshes are now ready to be biofunctionalized.

3.2.2. Biofunctionalization of Electrospun Meshes

The biofunctionalization process was carried out by using three molecules: CS (m_ePCL_CS), Gel (m_ePCL_Gel), and Arg (m_ePCL_Arg). These molecules possess the capacity to bind to the carboxyl groups of the samples of ePCL that had been

previously modified. The formation of bonds is attributable to the amine groups (-NH_2) of the biomolecules through EDC-NHS; a more detailed explanation was provided above (Figure 6).

In the course of this work, biofunctionalization protocols were created and optimized for each biomolecule. Once protocols were optimized, the meshes were doped with various concentrations of each biomolecule by exposing an m_ePCL mesh to an EDC-NHS solution, followed by a biomolecule solution. In an effort to find suitable biomaterial candidates for wound dressings for TE, each of the following biomolecules was chosen in this study due to their unique advantages. An overview of the hydrolysis and biofunctionalization process can be seen in Figure 7.

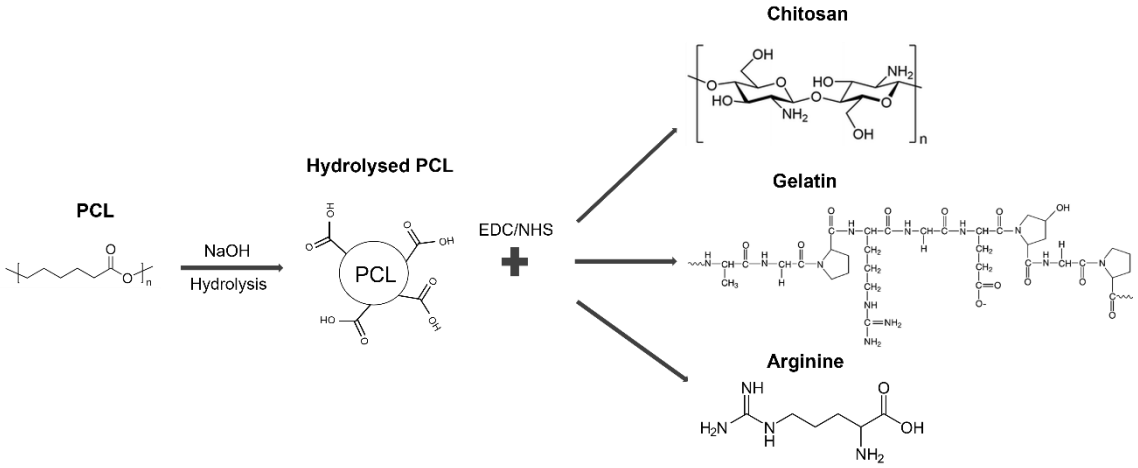

Figure 7 - Hydrolysis of the ePCL chain and subsequent biofunctionalization with each biomolecule.

For all biomolecules, the immobilization followed a carbodiimide coupling strategy using EDC and NHS. In each case, a pre-activation step was performed by incubating the meshes with an EDC/NHS solution for 15 minutes, after which the biomolecule solution was added and left to react overnight at 150 rpm and maintained at 37 °C. The following day, samples were washed three times with MilliQ water using a vortex and dried.

The preparation of the biomolecule solutions differed according to the molecule used. CS was dissolved in 0.1 M HCL at concentrations of 0.05, 0.1, and 0.5 wt%. This solution was added to the meshes, with an EDC/NHS solution prepared with MiliQ water, using 0.04441g of EDC and 0.01330g of NHS (for samples of 8.5 mm diameter).

Gel, in contrast, was dissolved in MilliQ water at concentrations of 0.1, 0.5, and 1 wt%, and the pre-activation step required the preparation of a 7:3 isopropanol:H2O solution containing EDC and NHS, before the Gel solution was added. For this solution, the same quantities of EDC/NHS were utilized as were employed for CS.

Arg, at concentrations of 0.5, 1, and 2 wt%, was prepared in a MES buffer (0.12 wt%) adjusted to pH 6.5 with 1 M NaOH. In this case, both the pre-activation solution and the biomolecule solution were prepared in the MES buffer before addition to the meshes. For this EDC/NHS solution, 0.00111g of EDC and 0.00033g of NHS were used (for a sample of 8.5 mm diameter).

3.2.3. Physico-Chemical Characterization

3.2.3.1. Apparent Density and Porosity

The high porosity of electrospun meshes is a critical factor in ensuring breathability and efficient exchange of gases across the mesh. The apparent density and porosity of the biofunctionalized ePCL meshes were subsequently calculated using equations (1) and (2), respectively [48]. The thickness of the meshes was measured with a micrometer to support these calculations.

$$\text{Apparent density } (\text{g}\cdot\text{cm}^{-3}) = \frac{\text{mesh mass (g)}}{\text{mesh thickness (cm)} \cdot \text{mesh area (cm}^2\text{)}} \quad (1)$$

$$\text{Mesh porosity } (\%) = \left(1 - \frac{\text{mesh apparent density } (\text{g}\cdot cm^{-3})}{\text{bulk density of the polymer + biomolecule } (\text{g}\cdot cm^{-3})}\right) \text{x } 100 \quad (2)$$

The dimensions of the ePCL meshes used to calculate the apparent density and mesh porosity were circular (1.5 cm in diameter).

3.2.3.2. Fourier Transform Infrared Spectroscopy with Attenuated Total Reflection

Fourier transform infrared spectroscopy with attenuated total reflection (FTIR-ATR, Alpha-P, Bruker Optik GmbH, Ettlingen, Germany) analysis is a vibrational technique that utilizes the emission of a beam of light with a wavelength in the infrared range and subsequently evaluates its absorption by the materials in question. The resulting spectrum is indicative of the composition of the material, thus enabling the identification of any chemical alterations that may occur. This technique was used to identify the functional groups on the surface of the samples, in the range of 4000–400 cm^{-1}, at a resolution of 4 cm^{-1} with 64 scans.

3.2.3.3. Scanning Electron Microscopy Analysis and Energy Dispersive X-ray Spectroscopy

The morphology of ePCL meshes were evaluated by Scanning Electron Microscopy (SEM, TESCAN, Vega3, Brno, Czech Republic) at a high voltage of 15kV. The surface composition of the meshes is determined through the observation of an electron beam that reflects off the sample and consequently produces an image. Through Energy Dispersive X-Ray Spectroscopy (EDX, Bruker, XFlash Detector 6|30,

Karlsruhe, Germany) analysis, a mapping was conducted to assess the presence of the biomolecule over the fiber's surface, through nitrogen (N) presence. A ratio was calculated with the EDX data that was retrieved, normalizing it through carbons (C), using equation 3:

$$\mathrm{N/C\ ratio} = \frac{\text{Atom (\%) of nitrogen}}{\text{Atom (\%) of carbon}} \quad (3)$$

Before the analysis, the meshes were coated with a thin layer of gold/palladium (Au/Pd) by sputter-coater equipment (Quorum Technologies, Lewes, UK). This procedure renders the mesh conductive, thus allowing for analysis and consequently serving to avert damage from the electron beam.

SEM images were also used to evaluate the different fiber diameters using ImageJ software (Fiji, version J1.46r, NIH, Bethesda, MD, USA) at 5000x magnification. For each condition, three individual samples were analyzed in three different zones each. For each image, 50 manually acquired measurements were performed.

3.2.3.4. Water vapor transmission rate

To evaluate the water vapor transmission rate (WVTR) of the ePCL meshes, five identical glass bottles were filled with 5 mL of phosphate-buffered saline (PBS) solution for each sample condition. The meshes were securely attached to the openings of the vials, allowing a defined vapor permeation area, 0.90 cm². The bottles were incubated at 32 °C for 24 hours. Water vapor transmission rate was assessed by recording the weight of each vial before and after incubation, and the evaporation of water through the meshes was determined based on the weight loss. The water vapor transmission rate was then calculated using the following equation (4):

$$\mathrm{WVTR} = \frac{\Delta W}{t\ A} \quad (4)$$

Where ΔW is the change in water weight (g), *t* is the time (days), and *A* is the effective permeation area (m²). This procedure follows the standard test methods for water vapor transmission [82].

3.2.3.5. Contact angle measurements

The wettability of the ePCL meshes was evaluated to determine whether the material surface is hydrophilic or hydrophobic. This was assessed using the static water contact angle (WCA) method, employing an optical tensiometer (model Theta Lite; Biolin Scientific, Manchester, UK). In this method, a 20 µL droplet of deionized water was gently deposited onto the surface of the electrospun mesh. The contact angle formed between the water droplet and the mesh surface was recorded using a high-resolution camera over 10 seconds (sec). For each condition, 5 different samples were analyzed.

Measurements were performed before and after modifications to the meshes to evaluate changes in surface affinity to water. A contact angle less than 90° indicates a hydrophilic surface, whereas an angle greater than 90° indicates a hydrophobic one [83].

3.2.3.6. Biomolecule attachment quantification

The ninhydrin (NHN) assay was utilized to determine the quantity of available amino groups in the liquid obtained from the biofunctionalization process, after carefully washing the meshes. This assay was utilized exclusively in the ePCL biofunctionalized with Arg, and the quantification was performed through UV–vis spectrometry. For meshes biofunctionalized with CS, the NHN assay was not employed because the CS/HCL solution presents an acidic pH, under which the assay is not effective. For the meshes biofunctionalized with Gel, the NHN assay could not be considered reliable, as repeated measurements yielded inconsistent and irreproducible results that did not correspond to the expected trends.

The liquid retained in the well after biofunctionalization was diluted with 4 mL of MES buffer and heated with NHN solution (2 g/100 mL) for 8 min in an incubator at 85 °C. Afterwards, 5 mL of ethanol was added to 100 µL of each sample, and the absorbance was recorded on a spectrophotometer (Lambda 35 from Perkin Elmer, USA) at a wavelength of 570 nm with Arg as a standard curve. A calibration curve was performed with solutions of Arg and MES buffer in varying concentrations, following the same procedure of heating and consecutive dilution with ethanol. Linear regression was performed with a correlation of 0.996. The extent of biomolecule attachment efficiency was defined by substituting the obtained absorbances into the line equation.

3.2.4. Mechanical performance – Tensile test

Mechanical characterization of the electrospun meshes was performed through tensile tests to determine YM, TSB, and EB, providing insight into the elasticity and mechanical integrity of the electrospun meshes. These properties are critical, as the meshes are designed to mimic skin, which experiences tensile forces regularly. Before testing, samples were cut to dimensions of 1.5 × 2.5 cm, and at least three measurements of each sample's thickness were taken using a micrometer. The tensile tests were conducted using a texture analyzer (TA.XT Plus model; Stable Micro System, Surrey, UK) using a 50 N load cell, with a fixed gauge length of 5 mm and a test speed of 1 mm/s until failure. The samples were incubated in deionized water for 20 minutes before being tested in a wet state. A minimum of 5 individual samples per group were tested to ensure statistical relevance.

3.2.5. Antimicrobial activity – Disk diffusion

Due to its prevalence in wounds, the reference strains used *were S. aureus* as a gram-positive bacteria and *E. Coli* as a gram-negative [84]. In brief, *S. aureus* and *E. Coli* were freshly cultured overnight in L.B. Agar (35g/L), at 37ºC. Afterward, colonies of bacteria were resuspended in an erlenmeyer with L.B. Medium (20g/L) and cultured for 2h at 37ºC in an orbital shaker until the optical density (OD) reached 0.15 – 0.20 at 600 nm. Then, the inoculum was spread with a swab on L.B. Agar plates. Meshes of 8.5 mm in diameter, previously sterilized with UV-light (270 nm) for 15 min on each side, were placed in the above L.B. Agar plate. After 18 h of incubation at 37 ºC, the formation of a "halo" was evaluated. The experiment was carried out three times.

3.2.6. *In vitro* studies

In vitro studies were performed using the L929 mouse fibroblast cell line, which is a reference model for in vitro cytotoxicity assays, following international standards as ISO 10993, and is also routinely used to test their proliferation in composite materials [85]. This cell line was cultured, expanded, and incubated at 37 °C in a 5% CO_2 humidified atmosphere incubator. When the cells reached 80–90% of confluence, they were detached. For this study, five samples of each condition were cut into a circular shape (0.85 cm) and sterilized using UV-light (270 nm) for 15 min (both sample sides) in a flow chamber. Following this procedure, the samples were left to soak in MilliQ Water for 24 hours to eradicate any residual impurities before the *in vitro* experiments. *In vitro* studies used cells from passages between 18 and 26.

The assessment of cell metabolic activity was conducted through the implementation of the resazurin assay. This method relies on the ability of viable cells to convert the fluorescent blue dye resazurin into the fluorescent pink compound resorufin, which can be quantified spectroscopically. The assay was performed by adding resazurin to the cell cultures at a final concentration of 20% (v/v) and incubating for 2 hours at 37°C in a humidified atmosphere containing 5% CO_2. After the incubation period, 100 µL of the reaction mixture was transferred to a black 96-well plate, and the degree of fluorescence was measured using a BMG LABTECH fluorimeter (FLUOstar Omega, Ortenberg, Germany) with excitation/emission wavelengths of 530/590 nm, respectively. The data presented are the mean of three independent experiments, each of which was performed in triplicate.

3.2.6.1. Cytotoxicity

The assessment of cellular toxicity was conducted employing both direct (DC) and indirect contact (IC) methodologies. For both approaches, 2×10^4 cells in 20 µL were seeded into 24-well plates containing 480 µL of DMEM per well. The plates were then incubated for 24 hours at a temperature of 37°C, within a 5% CO_2 humidified

atmosphere. For the IC configuration, the test meshes were positioned in distinct 24-well plates, with 500 µL of fresh culture medium per well, and subjected to incubation under identical conditions. After 24 hours, the medium from the cell cultures was substituted with the conditioned medium from the mesh incubated wells for the IC test. In the DC test, cells were exposed to fresh medium, and the meshes were placed in DC with them. Subsequently, both setups were subjected to an additional 24-hour incubation period. To facilitate comparisons, a control group was incorporated, comprising cells that were cultivated exclusively in fresh medium. Following the conclusion of the exposure period, the cell viability was measured using the resazurin assay.

3.2.6.2. Cell metabolic activity and proliferation

Cell metabolic activity and proliferation assay were conducted using 24-well plates, cells were seeded at a density of 1×10^4 in 10 µL in DMEM per sample, followed by a 2-hour incubation at 37 °C in a 5% CO_2 atmosphere, to ensure adequate cell penetration into the scaffolds. Subsequently, 500 µL of fresh medium was added. Metabolic activity and cell proliferation were monitored over 14-days with control time points at days 1, 3, 7, and 14. Additionally, a control group was incorporated, consisting of a sample of ePCL without cells in fresh medium. Following the conclusion of each exposure period, cell metabolic activity was measured using the resazurin assay. After metabolic activity was evaluated, the meshes were washed using PBS, 2 times for 5 minutes. A solution of GA 2.5% in PBS was added to each washed mesh for 30 minutes in order to ensure the fixation of the cells. The samples were washed again using PBS, 2 times for 5 minutes, and stored in PBS at 4 °C until further use.

3.2.6.3. Cell morphology and fibronectin deposition

The cell distribution and adhesion within the meshes of the 14-day period proliferation assay were characterized through confocal laser scanning microscopy (CLSM, Leica SP2AOBS, Leica Microsystems, Wetzlar, Germany) using LCS software (Leica Microsystems). For this means the ePCL meshes were stained for filamentous actin (F-actin), nuclei (DAPI), and fibronectin (FN) deposition. Samples were washed with PBS, fixed for 30 min in 2.5 wt% GA and permeabilized with 0.2% Triton X-100 for 7 min. Samples were then incubated for 1 h with 1 wt% BSA/PBS. For FN staining, the meshes were incubated overnight at 4 °C with rabbit anti-fibronectin (1:300). Later, the meshes were incubated again with the goat anti-rabbit secondary antibody Alexa Fluor® 488 F(ab′)2 (1:2000) and with the conjugated probe phalloidin/Alexa Fluor® 594 (1:40) for F-actin staining, both for 2h at room temperature. After staining, the meshes were washed three times with the PBS solution and nuclei were counterstained with DAPI in Vectashield, just before confocal visualization. The morphology of the cells cultured in the ePCL meshes was also analyzed using SEM analysis. Briefly, samples were also

washed with PBS and fixed for 30 min in 2.5 wt% GA and dehydrated with a successive graded ethanol series (40, 50, 70, 90, and 100%) for 15 min each.

3.2.7. Statistical analysis

Statistical analysis was carried out using R software (R Core Team, version 4.4x) and tested using Kruskal-Wallis One-Way Analysis of Variance on Ranks that was conducted for non-parametric hypothesis analysis. In the cases where the differences in the mean values among the treatment groups were greater than would be expected by chance, Dunn's tests were used for pairwise multiple comparisons. A p-value ≤ 0.05 (*) and ≤ 0.01 (**) was considered statistically significant.

4. Results and Discussion

4.1. Unmodified and modified ePCL meshes

4.1.1. Physico-chemical characterization

4.1.1.1. Fourier Transform Infrared Spectroscopy with Attenuated Total Reflection

FTIR analysis was the first characterization method performed to evaluate the chemical composition of unmodified and modified ePCL nanofibers with NaOH. Through the analysis of Figure 8, a comparison of the initial state of the surface chemistry of the sample with the one resulting from the hydrolysis process was achieved by studying the formation of new bands and/or the loss of bands that were originally present.

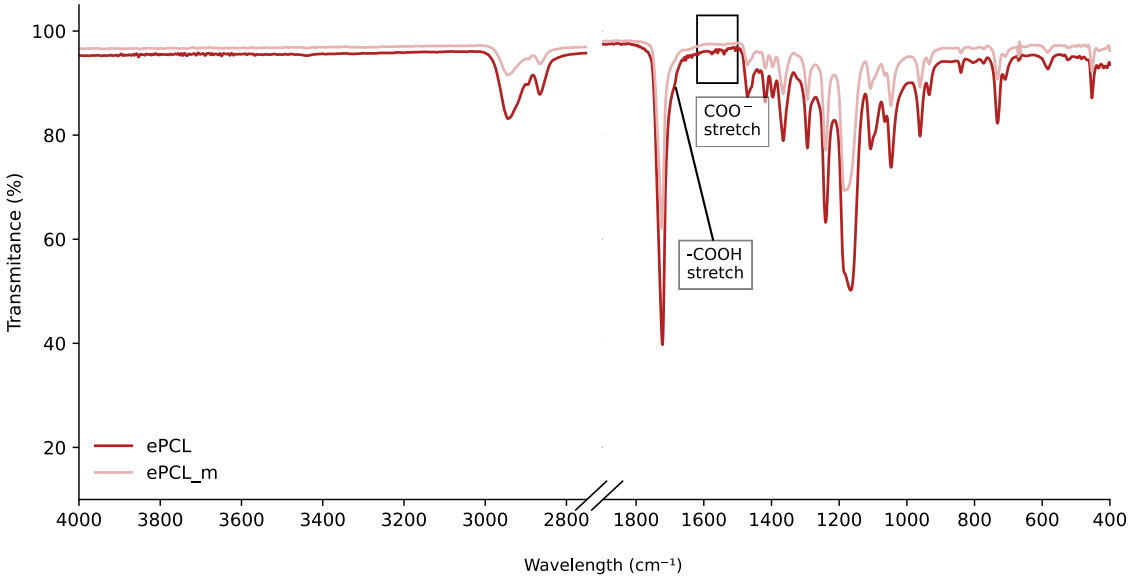

Figure 8 - FTIR spectra of unmodified and modified ePCL.

Table 1 shows the comparison of the characteristic FTIR bands of ePCL and m_ePCL, with some of the characteristic bands of PCL.

Table 1 - Comparison of characteristic FTIR bands of ePCL before and after NaOH hydrolysis according to assignments reported elsewhere [70,86–88].

	Assignment	
Bands	**ePCL**	**m_ePCL**

1720 cm^{-1}	Strong C=O	Decrease in intensity
1700 cm^{-1}	Absent	-COOH stretching vibration
~1560 - 1610 cm^{-1}	Absent	Asymmetric COO^- stretch
1180 cm^{-1}	Strong C-O-C	Decrease in intensity

A characteristic PCL band was identified at 1720 cm^{-1}, which was assigned to the carbonyl (C=O) stretching in esters [86,87]. Following the hydrolysis of the ePCL, there is a clear decrease in its intensity due to the hydrolysis of the ester bond. At 1700 $cm^{-1,}$ a new band is visible with a slightly displaced absorption, assigned to the carboxyl stretching [70,88]. Between 1560 and 1610 $cm^{-1,}$ there is an asymmetric COO^- stretch, meaning the appearance of carboxylate groups from hydrolysis [70,88]. Lastly, another strong PCL characteristic band was identified at 1180 cm^{-1}, assigned to a symmetric C-O-C stretching, which decreased in intensity, meaning that the ester linkages have broken [86,87]. Following a thorough analysis of the bands, it can be stated with confidence that the ePCL chain was successfully hydrolyzed using NaOH.

Following confirmation of the hydrolysis of the ePCL nanofibers through FTIR analysis, biofunctionalization protocols were tested and optimized. Each biomolecule and its controls were then individually characterized in a series of tests.

4.2. ePCL meshes modified with Chitosan

4.2.1. Physico-chemical characterization

4.2.1.1. Apparent Density and Porosity

The optimal scaffold for TE must feature a highly porous and interconnected network, typically with porosity exceeding 60%, to enable effective interactions and integration with host tissue [48]. The majority of cells utilized in TE are anchorage-dependent, necessitating the provision of suitable surfaces for attachment [48]. Consequently, for the use in scaffolds, this is imperative, as these provide a substantial and readily accessible surface area, thereby supporting adequate cell loading for tissue or organ repair and functionality. The promotion of cellular adhesion, migration, and nutrient diffusion is dependent on high porosity and open architecture, which enhances the potential for successful tissue regeneration [48,89].

According to the aforementioned equations (1) and (2), the theoretical values for porosity, apparent density, and thickness of the ePCL meshes biofunctionalized with CS and its controls are presented in Table 2. These properties can be directly correlated with the processing time.

Table 2 - Properties of ePCL meshes with CS at different concentrations and their controls.

Structure	Thickness (mm)	Apparent density (g/cm^3)	Mesh porosity (%)
ePCL	0.075 ± 0.001	0.25 ± 0.01	77.16 ± 1.32
m_ePCL	0.067 ± 0.002	0.22 ± 0.01	80.10 ± 1.20
m_ePCL_CS0.05	0.074 ± 0.002	0.33 ± 0.06**	73.44 ± 4.64*
m_ePCL_CS0.1	0.066 ± 0.002	0.34 ± 0.05**	72.82 ± 4.11*
m_ePCL_CS0.5	0.080 ± 0.001	0.32 ± 0.02**	73.92 ± 1.59*

** Represent statistical differences between m_ePCL_CS0.05/ 0.1/ 0.5 and m_ePCL ($p \leq 0.01$).

* Represent statistical differences between m_ePCL_CS0.05/ 0.1/ 0.5 and m_ePCL ($p \leq 0.05$).

The theoretical values for the porosity of the produced meshes range between 77.16 ± 1.32% (ePCL) and 80.10 ± 1.20% (m_ePCL) for the controls. As for the meshes after biofunctionalization with CS, the ranges for porosity are between 73.44 ± 4.64% (0.05 wt%), 72.82 ± 4.11% (0.1 wt%), and 73.92 ± 1.59% (0.5 wt%). All the meshes have very similar values for their porosity, which are in line with the porosity in the optimal range required for tissue regeneration.

4.2.1.2. Fourier Transform Infrared Spectroscopy with Attenuated Total Reflection

FTIR analysis was performed to evaluate the chemical composition of fibers and evaluate the interaction between ePCL and CS, using modified ePCL nanofibers as well as CS in powder as a control. The obtained spectra are shown in Figure 9.

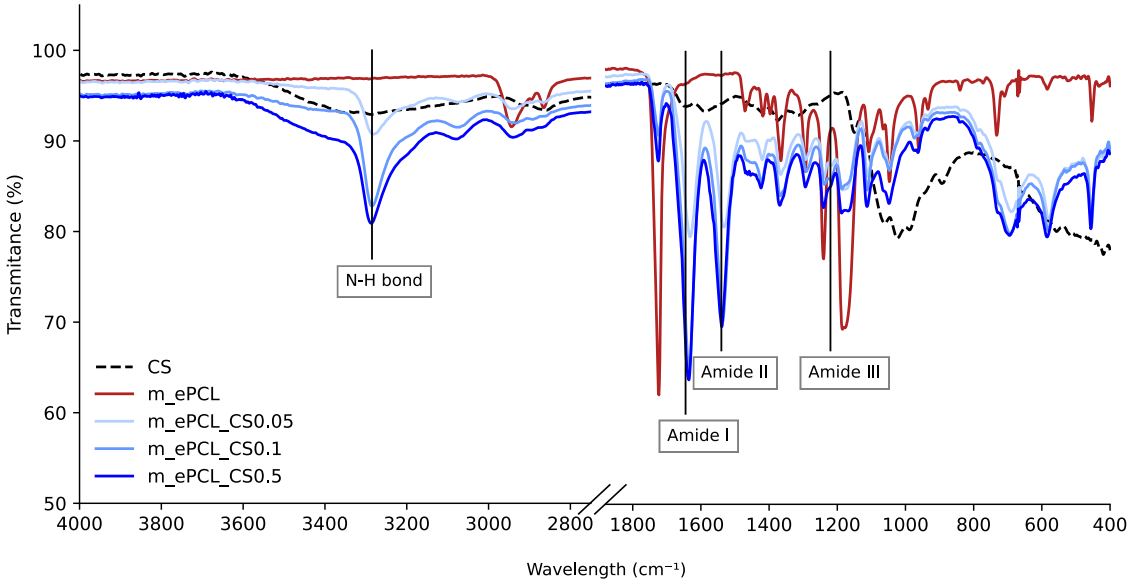

Figure 9 - FTIR spectra of modified ePCL with different concentrations of CS and controls.

Even though FTIR is a semi-quantitative technique, the analysis was conducted to compare samples biofunctionalized with CS to electrospun meshes modified before biofunctionalization, and not to quantify the amount of CS incorporated. Table 3 shows the comparison of the characteristic FTIR bands of m_ePCL and m_ePCL with CS incorporation, with some of the characteristic bands of CS identified.

Table 3 - Comparison of characteristic FTIR bands of modified ePCL before and after CS incorporation according to assignments reported elsewhere [90–94].

	Assignment	
Bands	**m_ePCL**	**m_ePCL_CS**
3285 cm^{-1}	Absent	O-H and N-H stretching vibration
1720 cm^{-1}	Moderate C=O	Decrease in intensity
1645 cm^{-1}	Absent	C=O stretching – Amide I
1540 cm^{-1}	Absent	N-H bending – Amide II
1220 cm^{-1}	Absent	C-N stretching – Amide III
1150 cm^{-1}	Weak	C-O-C vibration

At 3285 cm^{-1}, a CS characteristic band was identified. This band can appear between 3200 – 3600 cm^{-1} and is attributed to O-H and N-H stretching vibrations [91]. The band at 1720 cm^{-1} is a characteristic PCL band that decreases in intensity due to the CS coating covering the PCL, resulting in reduced carbonyl absorption visibility [92]. The appearance of three new CS amide bands, at 1645 cm^{-1} (Amide I), 1540 cm^{-1} (Amide II), and 1220 cm^{-1} (Amide III) confirms that immobilization of CS was performed successfully. Amide I and II can normally be visible between 1655 – 1645 cm^{-1} and 1590 – 1550 cm^{-1}, respectively. These assignments are attributed to the C=O stretching of CS acetylated units and to N-H bending, respectively [90]. Lastly, amide III can normally be observed between 1320 – 1250 cm^{-1} and is assigned to C-N stretching. However, in this case, this region overlaps with the PCL C-O-C stretching in esters (1240-1170 cm^{-1}) and CS polysaccharide C-O vibrations (1150-1020 cm^{-1}), which explains why the amide III feature appears more as a shoulder than a distinct band and why it is observed at 1220 cm^{-1} [93,94]. At 1150 cm^{-1}, a strong band of glycosidic C-O-C vibrations of CS was also identified [93]. The observed spectrum and the bands that were identified confirm that CS was successfully biofunctionalized at all concentrations on the surface of the modified ePCL.

4.2.1.3. Scanning Electron Microscopy Analysis and Energy Dispersive X-ray Spectroscopy

SEM morphological images of ePCL meshes for the different concentrations of CS and controls are shown in Figure 10 ((A)-(E)).

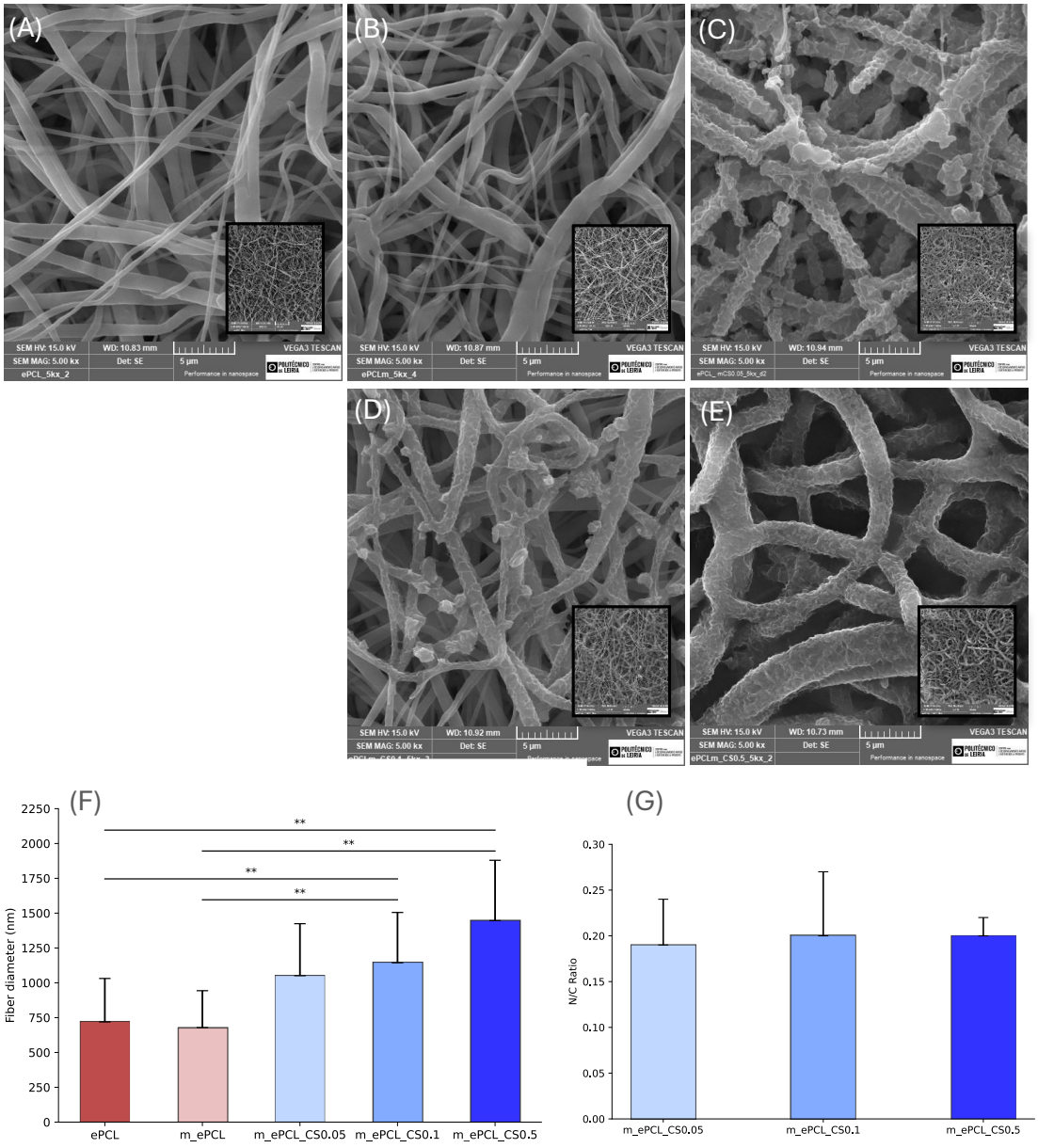

Figure 10 - SEM of ePCL (A): (B) – without biofunctionalization; (C) – with CS 0.05 wt%; (D) – with CS 0.1 wt%; (E) – with CS 0.5 wt%; (F) comparative fiber average diameter; (G) comparative EDX analysis. Statistical significance for $p \leq 0.01$ (**).

According to these images, the control samples of ePCL and modified ePCL (Figure 10 (A) and (B), respectively) show well defined continuous filaments without the presence of beads. It is also possible to observe a subtle difference in morphology between ePCL and modified ePCL, indicating a slight degradation that can be correlated with the decrease in ester groups by FTIR analyses. The different concentrations of CS,

namely 0.05 wt%, 0.1 wt%, and 0.5 wt% (Figure 10 (C)-(E), respectively), can be observed encapsulating the ePCL nanofibers with very few changes in the mesh morphology, such as the introduction of some rugosity in the mesh. Additionally, no closed pores were observed. According to the comparative study that was conducted (Figure 10 (F)), for the ePCL sample, the average fiber diameter is 719 ± 311 nm, and for the m_ePCL is 678 ± 264 nm. With the incorporation of different concentrations of CS, there is a clear increase in the average fiber diameter, from Figure 10 (C) to (E), are 1051 ± 373 nm, 1144 ± 361 nm, and 1446 ± 433 nm, respectively. Additionally, these results are statistically significant when compared with the control groups. The standard deviation exhibits a similar trend across all conditions.

The chemical biofunctionalization of CS onto modified ePCL leads to the formation of a covalent bond between the carboxyl groups of the ePCL and the protonated amines of the CS, which can promote local thickening on the nanofibers' surface, explaining why the average diameter increases [95]. Consequently, as additional CS is added, further amide bond pairings are formed until no further carboxylates remain available for reaction, rendering the nanofiber's surface fully coated.

Lastly, EDX analysis was also performed on the samples with CS. A comparative analysis can be observed of the N/C atoms ratio (Figure 10 (G)) present in each concentration on CS, namely, 0.19 ± 0.05, 0.20 ± 0.07, and 0.20 ± 0.02, for 0.05 wt%, 0.1 wt%, and 0.5 wt%, respectively. These results corroborate the previous analysis of SEM imaging. Although there is no statistical difference, there is a strong and consistent presence of N atoms, meaning that CS is present on the nanofibers’ surface.

4.2.1.4. Water vapor transmission rate

The occurrence of either a dry wound or a wound infection can result from an imbalance of moisture and secretions between the wound dressing and the wound itself. Consequently, if the WVTR of a wound dressing is too high, the wound may become dehydrated. Conversely, if the WVTR is too low, exudate can accumulate, which can lead to complications. Therefore, it is crucial to select a dressing with an appropriate WVTR in order to maintain a moist environment that supports optimal healing. The recommended range reported in literature for an ideal WVTR is 2000–2500 g/m²/day for moist wound healing in clinical settings, striking a balance between moisture retention and vapor permeability [96]. Although values for electrospun produced wound dressings that can be found in literature are between 3500–4500 g/m²/day [97,98]. These values are in line with the results obtained for WVTR of ePCL with different concentrations of CS and controls that can be observed in Table 4.

Table 4 - WVTR of ePCL with different concentrations of CS and controls.

Structure	WVTR (g/m^2/day)
ePCL	3302.00 ± 24.00
m_ePCL	3369.88 ± 47.35
m_ePCL_CS0.05	3384.08 ± 14.12
m_ePCL_CS0.1	3422.49 ± 45.77
m_ePCL_CS0.5	3510.35 ± 28.43 **

Represent statistical differences between m_ePCL_CS0.5 and ePCL for $p \leq 0.01$ (**).

The values of WVTR for the produced meshes range between 3302.00 ± 24 g/m²/day (ePCL) and 3369.88 ± 47.35 g/m²/day (m_ePCL) for the controls. As for the meshes after biofunctionalization with CS, the ranges for WVTR are between 3384.08 ± 47.35 g/m²/day (0.05 wt%), 3422.49 ± 45.77 g/m²/day (0.1 wt%), and 3510.35 ± 28.43 g/m²/day (0.5 wt%). There is also statistical significance between the ePCL mesh and the ePCL with CS at 0.5 wt%. All the meshes have very similar values for their WVTR, these are typical for TE applications, meaning they are higher than most market hydrocolloid or foam products, but similar to published values for ePCL, and CS-based wound dressings [97,98].

Although these values exceed the optimal range recommended for general wound dressings, a higher WVTR is a common feature in electrospun materials. This behavior is attributed to the highly porous and thin fibrous structure of the material, which facilitates water vapor diffusion, and to the hydrophilic nature of CS, which enhances moisture exchange. Furthermore, higher WVTR values can be advantageous for wounds with moderate to high exudation, as they prevent excessive moisture accumulation and maceration while maintaining adequate hydration at the wound interface [99]. Consequently, the elevated WVTR values observed in this study are not necessarily detrimental, instead, they reflect the open microstructure and bioactive composition of the electrospun CS-modified meshes, which promote a balanced moist environment favorable for tissue regeneration.

4.2.1.5. Contact angle measurements

The WCA assay was employed to evaluate the water affinity of the meshes. In this assay, a single drop of water is deposited onto the surface of the mesh, and the contact angle is subsequently measured. If the recorded contact angle is less than 90°, it is indicative of a hydrophilic surface, whereas a contact angle greater than 90° suggests a hydrophobic surface [83]. WCA was observed at 0 and 10 sec marks with corresponding images in each condition, as shown in Figure 11 (A) and (B), respectively.

According to contact angle analysis, ePCL resulted in more hydrophobic surfaces with reduced water uptake capacity in both short-time (0 sec) (104.64 ± 2.01°) and long-time response (10 sec) (102.71 ± 2.06°). On the other hand, hydrolyzed ePCL resulted in more hydrophilic surfaces after 10 sec absorption (77.78 ± 14.94°), as it was expected, given the break in the mesh surface, which introduces -OH and -COOH groups, that increases polarity [100]. The incorporation of CS, namely ePCL with CS at 0.05 wt% and 0.1 wt%, resulted again in slightly more hydrophobic surfaces after both 0 sec (108.06 ± 7.27° and 109.71 ± 3.78°, respectively) and 10 sec (89.5 ± 9.15° and 90.80 ± 16.63°, respectively) when compared with hydrolyzed ePCL meshes.

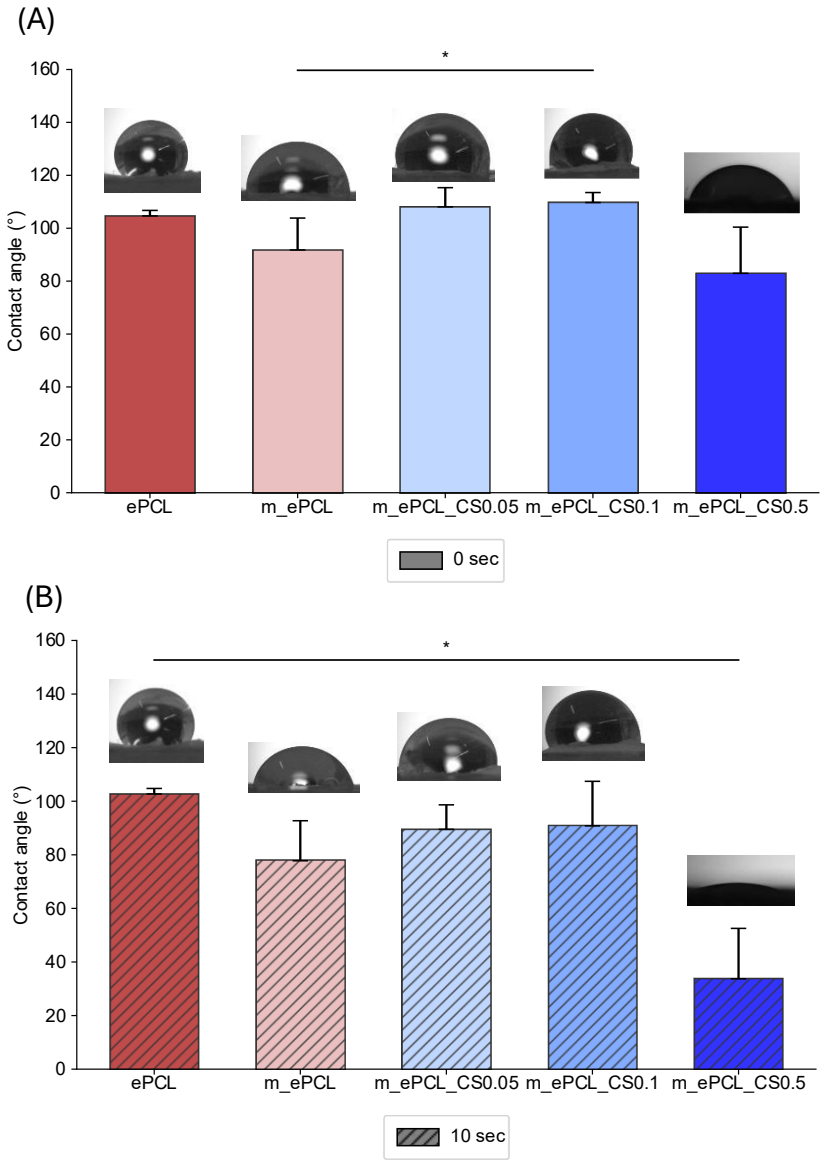

Figure 11 - WCA of ePCL with different concentrations of CS and controls with corresponding images: (A) - at 0 sec; (B) - at 10 sec. Statistical significance for $p \leq 0.05$ (*).

Although CS is extremely hydrophilic, the results can be explained by the fact that the incorporation of CS is attached to ePCL through the -COOH groups, which reduces de free ionic groups that attract water [101]. So, adding a small amount of CS

is insufficient to render the structure hydrophilic and can also neutralize some highly hydrophilic groups of the m_ePCL, thereby reducing surface wettability.

At a higher concentration of 0.5 wt% of CS, after a short-time response (82.93 ± 17.49°), the structure appears to be more hydrophilic. After 10 sec (33.73 ± 18.81°), a significant reduction in contact angle is observed, resulting in the almost complete dispersal of the droplet throughout the structure, meaning a high hydrophilicity. In this case, CS likely covers a more extensive area of the surface, consequently exposing the polar groups of the CS. This exposure facilitates the spread of water, thereby reducing the WCA [102]. Material hydrophilicity is a crucial factor, as it substantially enhances cell adhesion, proliferation, and migration, processes essential for tissue development and repair [100].

4.2.2. Mechanical performance – Tensile test

The mechanical properties of ePCL meshes with different concentrations of CS were assessed in relation to different structural compositions. Given the heterogeneity of the human skin, its mechanical characteristics cover a broad spectrum, as reference values, the YM ranges from 0.05 to 150 MPa, TSB from 1 to 32 MPa, and EB from 17 to 207% [103–106]**.**

Representative stress-strain curves are shown in Figure 12 (A), YM (MPa) in Figure 12 (B), EB (%) in Figure 12 (C), and lastly TSB (MPa) in Figure 12 (D).

Modified ePCL and ePCL meshes were used as controls. The ePCL possesses optimal mechanical properties (YM = 0.02 ± 0.0 MPa; EB = 323.16 ± 15.08 %; TSB = 1.82 ± 0.10 MPa), rendering it a promising candidate for use as a skin substitute. The integration of CS into the ePCL is anticipated to enhance its structural integrity, thereby approaching the properties exhibited by the ePCL. The stress–strain curves demonstrated that ePCL exhibited higher stress values throughout deformation. The quantitative analysis confirmed that the incorporation of CS (0.05 wt%; 0.1 wt%; 0.5 wt%), did not have a significant effect on YM (0.04 ± 0.02 MPa; 0.03 ± 0.01 MPa; 0.03 ± 0.01 MPa, respectively), suggesting that the stiffness remained unchanged. However, a tendency for 0.05 wt% CS to appear with low elasticity was observed. In contrast, both EB and TSB were significantly higher in ePCL compared to all modified samples. In EB, the ePCL sample exhibited statistically significant changes in conjunction with all the other samples. However, in TSB, ePCL only demonstrated statistical significance in relation to the CS 0.1 wt% sample. Of particular significance was the observation that no statistical differences were detected among the various CS concentrations, such as 0.05 wt% (EB = 160.59 ± 23.74 %; TSB = 1.24 ± 0.25 MPa), 0.1 wt% (EB = 147.42 ± 52.29 %; TSB = 0.96 ± 0.05 MPa) and 0.5 wt% (EB = 193.14 ± 42.67 %; TSB = 1.19 ± 0.25 MPa), indicating that the reduction in ductility and strength was not influenced by the different CS concentrations, with mechanical properties remaining relatively stable. This

further suggests that CS incorporation does not compromise the mechanical properties of the material.

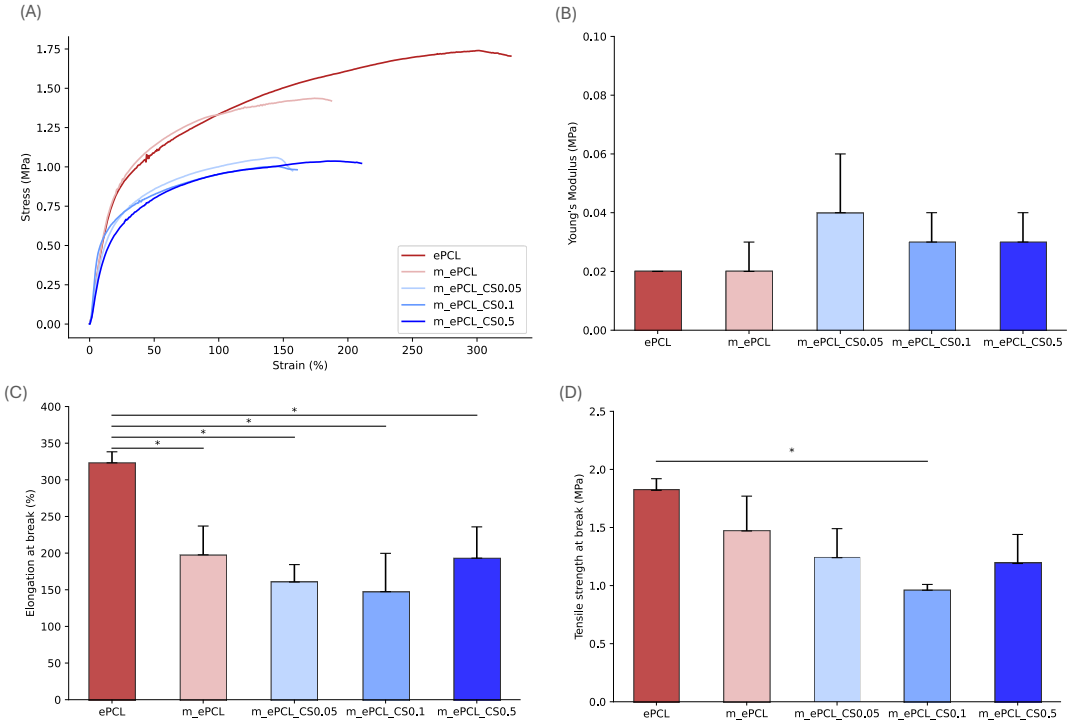

Figure 12 - Mechanical behaviour at wet state of ePCL with different concentrations of CS and controls, (A) – Stress-strain representative curves; (B) – Young's Modulus (MPa); (C) – Elongation at break (%); (D) – Tensile strength at break (MPa). Statistical significance for $p \leq 0.05$ (*)

Modified ePCL and ePCL meshes were used as controls. The ePCL possesses optimal mechanical properties (YM = 0.02 ± 0.0 MPa; EB = 323.16 ± 15.08 %; TSB = 1.82 ± 0.10 MPa), rendering it a promising candidate for use as a skin substitute. The integration of CS into the ePCL is anticipated to enhance its structural integrity, thereby approaching the properties exhibited by the ePCL. The stress–strain curves demonstrated that ePCL exhibited higher stress values throughout deformation. The quantitative analysis confirmed that the incorporation of CS (0.05 wt%; 0.1 wt%; 0.5 wt%), did not have a significant effect on YM (0.04 ± 0.02 MPa; 0.03 ± 0.01 MPa; 0.03 ± 0.01 MPa, respectively), suggesting that the stiffness remained unchanged. However, a tendency for 0.05 wt% CS to appear with low elasticity was observed. In contrast, both EB and TSB were significantly higher in ePCL compared to all modified samples. In EB, the ePCL sample exhibited statistically significant changes in conjunction with all the other samples; however, in TSB, ePCL only demonstrated statistical significance in relation to the CS 0.1 wt% sample. Of particular significance was the observation that no statistical differences were detected among the various CS concentrations, such as 0.05

wt% (EB = 160.59 ± 23.74 %; TSB = 1.24 ± 0.25 MPa), 0.1 wt% (EB = 147.42 ± 52.29 %; TSB = 0.96 ± 0.05 MPa) and 0.5 wt% (EB = 193.14 ± 42.67 %; TSB = 1.19 ± 0.25 MPa), indicating that the reduction in ductility and strength was not influenced by the different CS concentrations, with mechanical properties remaining relatively stable. This further suggests that CS incorporation does not compromise the mechanical properties of the material.

4.2.3. Antimicrobial activity – Disk diffusion

As previously mentioned, CS has been shown to confer antimicrobial properties [14,49]. Therefore, the antimicrobial activity of ePCL scaffolds modified with 0.5 wt% was evaluated using disk diffusion assays against *S. aureus* and *E. coli*, as shown in Figures 13 and 14, respectively. For both images, (A) represents a plate with the meshes and (B) represents the same plate without the meshes to evaluate the effect of the mesh on the bacteria. None of the samples produced inhibition zones, confirming the lack of intrinsic antibacterial activity, even with the incorporation of CS. Although only the single droplet of CS 0.5 wt% solution (with the equivalent amount of CS, in grams, as 0.5 wt% CS electrospun mesh) seems to have some antimicrobial activity for both bacteria, the mesh with 0.5 wt% CS concentration is still insufficient to generate a detectable inhibitory halo. The enhanced antibacterial efficacy of the free CS solution in comparison to CS incorporated within ePCL can be attributed to its rapid diffusion and immediate availability within the agar medium. In contrast, the release of CS from the ePCL scaffold is characterized by a more delayed and localized release, resulting in a reduced effective concentration in the surrounding medium and, consequently, reduced antibacterial activity.

Overall samples in Figure 13 showed more of an inhibitory halo than just the inhibition below the mesh that is captured in Figure 14. This occurrence can be attributed to the variability of the CS antimicrobial effect across different bacterial strains. Studies show that Gram-positive strains, such as *S. aureus*, are often more sensitive than Gram-negative strains, such as *E. coli* [107,108]. This is primarily due to the outer membrane of *E. coli* functioning as a barrier, whilst the cell wall of *S. aureus* is more exposed, allowing interaction with the amine groups of the CS. Consequently, the results observed in this study may be indicative of a more pronounced effect against *S. aureus* in comparison to *E. coli*. Minimum inhibitory concentration (MIC) assay should be performed in future work to better define the threshold concentration of CS required to inhibit bacterial growth. Such assays would clarify whether the non-existent antibacterial effect is due to low concentration of CS, or because of the lack of free amino groups ($-NH_3^+$) to react with the cell wall of the bacteria.

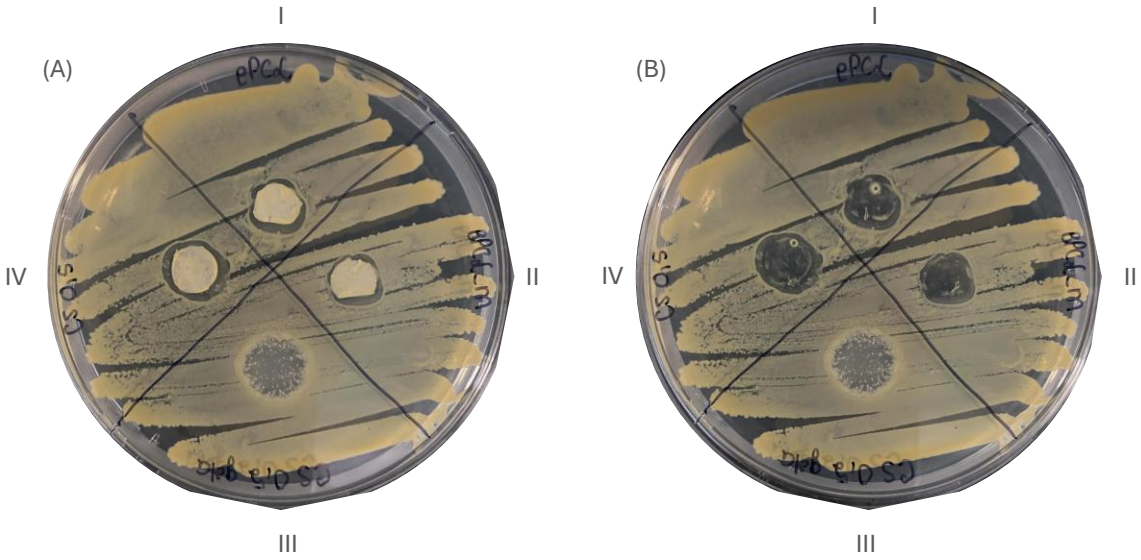

Figure 13 - Disk diffusion assay of (I) ePCL, (II) m_ePCL, (III) solution of CS 0.5 wt%, (IV) ePCL with CS 0.5 wt%, against *S. aureus*. (A) shows the plate with the mesh, and (B) shows the same plate without the mesh.

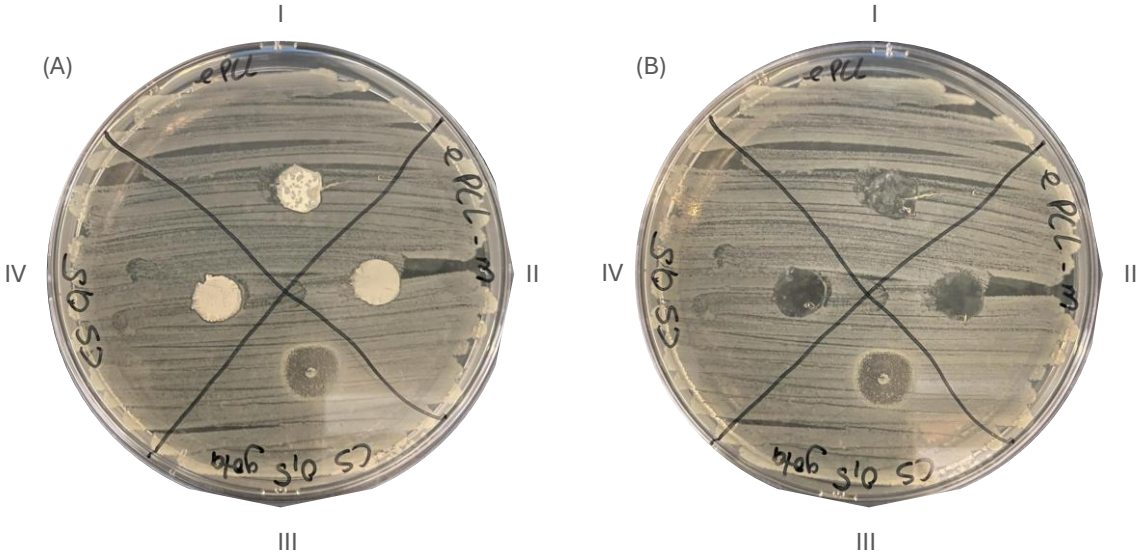

Figure 14 - Disk diffusion assay of (I) ePCL, (II) m_ePCL, (III) solution of CS 0.5 wt%, (IV) ePCL with CS 0.5 wt%, against *E. coli*. (A) shows the plate with the mesh, and (B) shows the same plate without the mesh.

4.2.4. *In vitro* studies

4.2.4.1. Cytotoxicity

The cytotoxicity of the produced ePCL meshes was assessed only at the highest concentration of CS incorporation, ePCL, and modified ePCL as controls, since testing the maximum concentration is sufficient to determine whether CS incorporation poses any cytotoxic effect, and lower concentrations can therefore be considered non-cytotoxic. Cytotoxicity was evaluated at IC and DC, the results of this assay can be observed in Figure 15 (A) and 15 (B), respectively. The process of IC involves the

exposure of cells to a culture medium that has been pre-conditioned by the test material in this case, the meshes. This medium has been incubated separately, ensuring that the material does not come into direct contact with the cells. DC is defined as the placement of the meshes in physical contact with the cells in the culture wells during the incubation period. The determination of a sample as cytotoxic is dependent upon the presence of ≤ 70% metabolic activity.

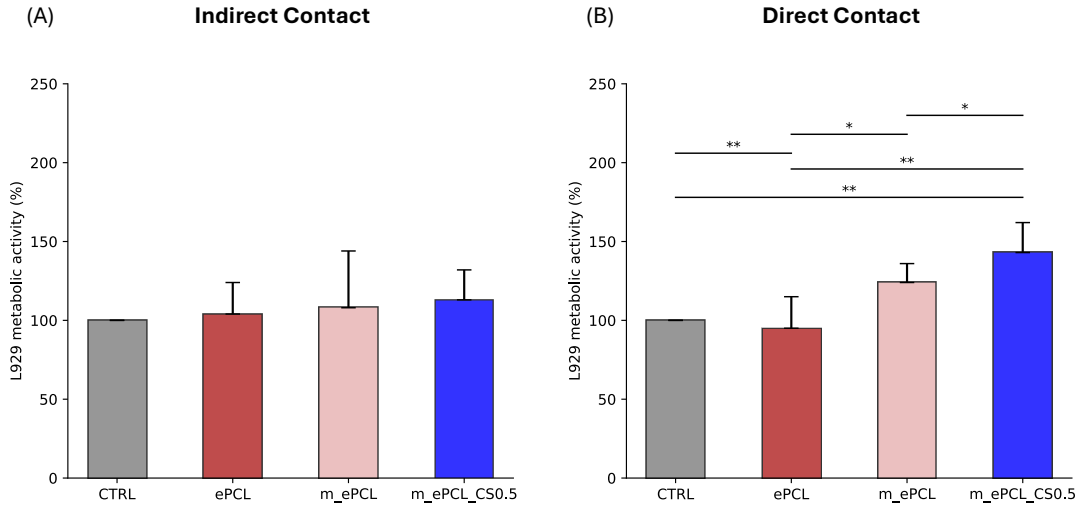

Figure 15 - Cytotoxicity assessment of ePCL with CS at 0.5 wt% and controls. (A) IC and (B) DC with L929 cell line, for 24h. The positive control consisted of cells growing in the well without samples. Statistical significance for p ≤ 0.05 (*) and p ≤ 0.01 (**).

According to the results obtained, fibroblasts remained metabolically active in all conditions tested. In the IC assay (Figure 15 (A), no sample has presented any cytotoxicity. Considering the positive control as having 100% metabolic activity, the remaining values were calculated accordingly. For ePCL, metabolic activity has been recorded at 104 ± 20%, and for modified ePCL at 108 ± 36%. These results indicate that neither of the control samples demonstrates cytotoxicity. The sample with 0.5 wt% CS demonstrated 113 ± 19% of metabolic activity, which was also non-cytotoxic. In the DC assay (Figure 15 (B)), no cytotoxicity was observed for all the tested samples. Both controls, ePCL and modified ePCL, exhibit metabolic activity of 95 ± 20% and 124 ± 12%, respectively. For the ePCL biofunctionalized with CS at 0.5 wt%, the increase in metabolic activity was evident at 143 ± 19%, having exhibited a ~43% increase in metabolic activity when compared with the positive control sample. This suggests that the direct interaction with CS strongly stimulated fibroblast metabolism, possibly due to CS's known biocompatibility and ability to support cell adhesion and proliferation [109]. Statistical significance was observed in DC. Even though statistical significance was not observed in IC, a trend is visible that suggests CS positively affects cell metabolism in both setups.

4.2.4.2. Cell metabolic activity and proliferation

The proliferation of L929 cells after 1, 3, 7, and 14 days of culture on ePCL meshes biofunctionalized with CS (for all conditions) was assessed using a metabolic activity assay (Figure 16).

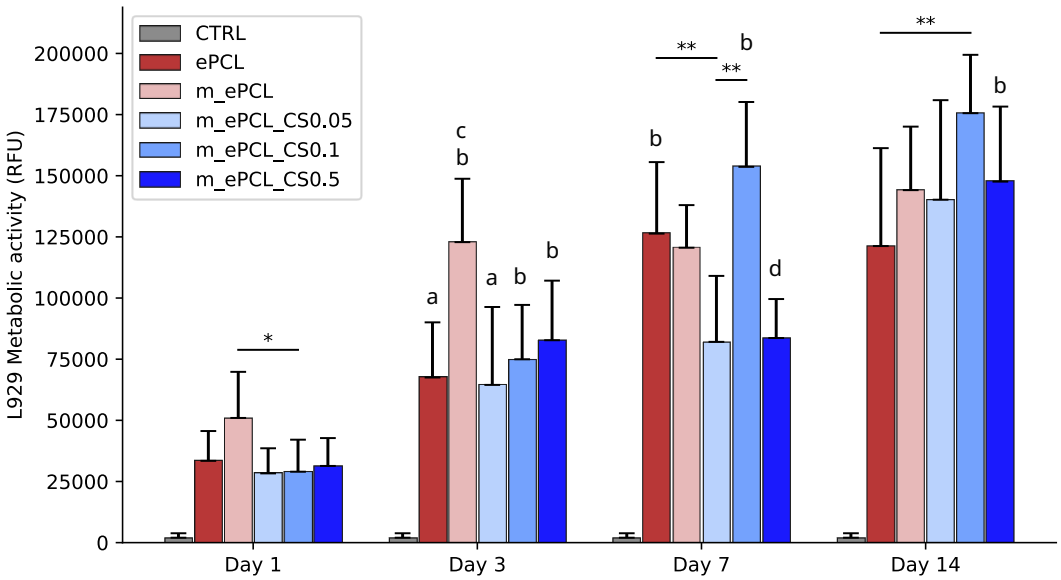

Figure 16 - Metabolic activity of L929 cells on ePCL with different concentrations of CS and controls through 1, 3, 7 and 14 days after seeding, using an ePCL mesh without cells as a control for the experiment. Statistical significance for $p \leq 0.05$ (*) and $p \leq 0.01$ (**); Statistical significance with the previous time-point of $p \leq 0.05$ (a); Statistical significance with the previous time-point of $p \leq 0.01$ (b); Statistical significance with all other conditions is $p \leq 0.05$, except to m_ePCL_CS0.5, which is $p \leq 0.01$ (c); Statistical significance with ePCL (**), m_ePCL_CS0.1 (**) and m_ePCL (*) (d).

Throughout the 14 days, the cells remained metabolically active and increased their activity between time points. All samples showed statistical significance at day 3 compared to day 1 within their own condition. Only samples with 0.1 wt% CS and ePCL presented differences at day 7 compared to the previous time-point. Additionally, only the sample with 0.5 wt% CS showed statistical significance at day 14 compared to day 7. These results may be explained by the fact that, up to day 7, cells prefer samples with higher mechanical properties, whereas after that point, the samples containing biological cues provided by CS seem to be more attractive, leading to higher metabolic activity. On day 1, comparing all conditions, the metabolic activity is generally low, likely cells are still adhering and adapting to the fiber surface. According to the literature, PCL does not have affinity to the cells due to its hydrophobic character, which can be observed in this case, having statistically significantly less metabolic activity than the other structures [110]. In contrast, the modified ePCL has been shown to exhibit enhanced cell affinity,

attributable to its polar groups that render the mesh hydrophilic. This observation is corroborated by the results, which demonstrate that the modified ePCL exhibits augmented metabolic activity of the cells when compared with the ePCL, both between time points and within each time point. When CS is incorporated into the mesh on day 1, there is minimal metabolic activity, particularly in comparison with the modified ePCL. These findings can be explained and corroborated by the results of the WCA, where the structures exhibited hydrophobic behaviour, likely occurring because the polar groups were being covered by CS. However, it has been demonstrated that, in the context of WCA analysis, it is the lower concentrations of CS that render the structure hydrophobic. It is only at concentrations of 0.5 wt% that the structure becomes hydrophilic. The results previously obtained can be correlated with the slight tendency for an increase in metabolic activity on days 1 and 3. At day 7, the sample with CS at 0.1 wt% presents statistically higher metabolic activity when compared with the other concentrations and controls, and this trend is maintained up to 14 days. At 0.1 wt%, CS likely provides an optimal balance of bioactive sites such as amino groups that enhance cell adhesion and proliferation without causing structural or potential cytotoxic issues that can be associated with higher concentrations. This concentration seems to improve the overall scaffold and mimic the ECM cues, creating a favourable environment for sustained increase in cell activity up to 14 days. Moreover, from day 7 to day 14, this increase slows down, as no statistical significance was observed, which might be due to the upper limit of the structure to accommodate additional cells. Lower or higher CS levels may either lack sufficient bioactivity or cause aggregation that impairs cell interactions, making the ePCL biofunctionalized with 0.1 wt% CS the most effective concentration for promoting fibroblast metabolism over time. Overall, after 14 days, the samples combining mechanical and biological cues showed the best performance, in agreement with previous studies [110]

4.2.4.3. Cell morphology and fibronectin deposition

ePCL meshes biofunctionalized with CS were further analyzed by SEM (Figure 17) and confocal microscopy (Figure 18) after 14 days of culture. The observed cell distribution was found to depend on the hydrophilic or hydrophobic properties of the sample (Figure 17). The process of seeding was performed centrally, with hydrophilic structures rapidly absorbing the cell suspension. This facilitated even dispersal of the cells throughout the scaffold. In contrast, hydrophobic surfaces delay the initial spreading process, resulting in a higher cell concentration at the centre of the sample. However, over time, these cells gradually migrate, ultimately resulting in their distribution across the entire structure.

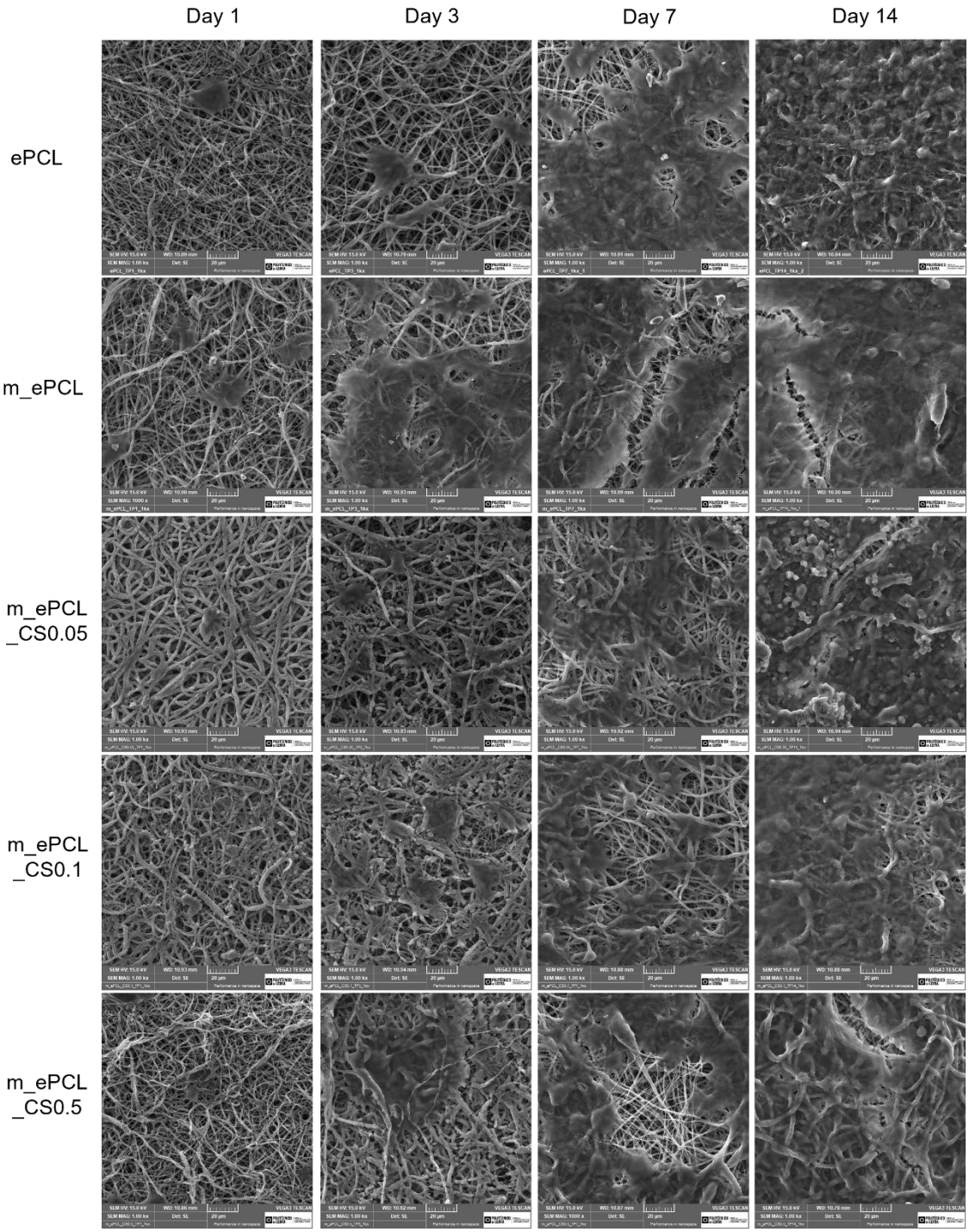

Figure 17 - Representative proliferation SEM images of L929 cells evaluated at 1, 3, 7 and 14 days of study after seeding in ePCL with different concentrations of CS and controls. Scale bars correspond to 20 µm.

As observed in SEM imaging, on day 1, all scaffolds exhibited sparse cellular attachment, indicative of the initial phase of cell seeding and adaptation. By day 3, an increase in cell number and spreading was evident, with biofunctionalized meshes demonstrating greater cell coverage and interaction compared to the controls. Days 7 and 14 are characterized by robust cell proliferation, with thick cellular layers forming by day 14, mainly in meshes containing 0.1 and 0.5 wt% CS. At day 7, some cell infiltration

into the mesh was observed, particularly in the modified ePCL sample, which presents higher porosity that facilitates cellular migration.

Figure 18 presents the confocal microscopy analysis of ePCL meshes biofunctionalized with CS over 14 days.

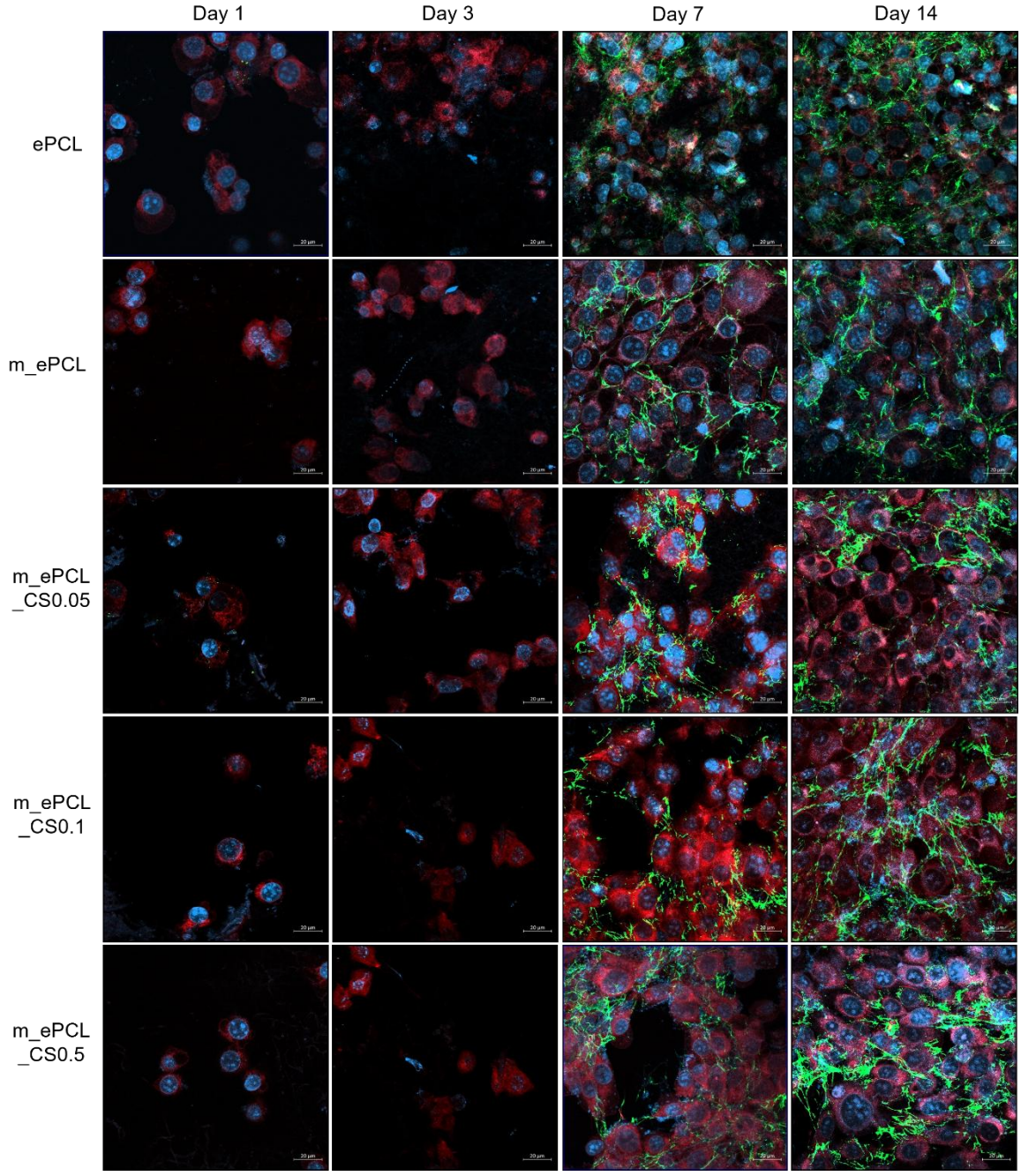

Figure 18 - Representative proliferation confocal images of L929 cells evaluated at 1, 3, 7 and 14 days of study after seeding in ePCL with different concentrations of CS and controls (blue: nuclei; red: actin; green: FN). Scale bars correspond to 20 µm.

The nuclei, stained blue, appear as distinct, rounded structures indicating the presence of cells. The red staining highlights the F-actin (cytoskeleton), whose evaluation is crucial to understand cell morphology, adhesion, migration and proliferation. The FN deposition (green) is associated with the early stages of ECM

formation and tissue remodeling, as it represents a provisional matrix that supports cell adhesion, migration, and the subsequent deposition of other ECM components [111].

At day 1, few cells with well-defined nuclei and actin filaments are observed across all samples, showing initial cell attachment. By day 3, both nuclei and actin staining increase, indicating active cell spreading and cytoskeletal organization. However, in the first three days, FN deposition was not observed, since cells were mainly adapting to the substrate, establishing stable adhesion, and had not yet achieved the metabolic activity and density required to begin FN production and fibril organization. Extensive networks of actin filaments surrounding numerous nuclei were evident at days 7 and 14, particularly on modified ePCL and CS functionalized meshes, together with pronounced FN matrix formation. On day 14, ePCL samples presented some cells with a rounded morphology and reduced FN deposition, which corroborated the SEM images and metabolic activity results, suggesting that the structure is not able to support cellular proliferation over time. Although the mechanical and physical properties are favorable to promote new tissue formation, the lack of biological cues seems to be crucial at that stage to sustain tissue ingrowth. Confocal images of the individual staining for nuclei, actin, and FN are also presented in Figures 37A - 41A in the appendix section.

These findings demonstrate that CS biofunctionalization enhances cellular adhesion and cytoskeletal development, both essential for robust proliferation and extracellular matrix synthesis. The well-organized actin cytoskeleton suggests strong anchorage, supporting cell viability and scaffold integration. The nuclear morphology throughout culture remains consistent with a healthy proliferative phenotype, corroborating the quantitative metabolic assays previously performed. Collectively, these observations imply that the bioactive modifications facilitate improved cellular responses, matrix assembly, and ultimately scaffold functionality for TE.

According to SEM and the appropriate porosity of the biofunctionalized CS nanofibers, these structures can be considered to have great potential for skin TE due to their interconnected pore network with CS coating and suitable WVTR and WCA. Among the tested concentrations, 0.1 wt% CS provided the most favourable balance of properties. While 0.5 wt% CS significantly enhances wettability, this improvement does not translate into superior long-term cell proliferation. Conversely, 0.1 wt% CS sustains higher metabolic activity over 14 days without further compromising the mechanical properties of the scaffold. Consequently, 0.1 wt% CS can be regarded as the optimal concentration for achieving both biological performance and material stability.

4.3. ePCL meshes modified with Gelatin

4.3.1. Physico-chemical characterization

4.3.1.1. Apparent Density and Porosity

As aforementioned, an ideal TE scaffold should be porous and interconnected to promote cell attachment, migration and nutrient diffusion, as well as provide an extensive surface area to support tissue repair and regeneration [48,89].

Similarly to the previous biomolecule, equations (1) and (2) were used to obtain the theoretical values for porosity, apparent density, and thickness for the ePCL meshes biofunctionalized with Gel and their respective controls, which are presented in Table 5.

Table 5 - Properties of ePCL meshes with Gel at different concentrations and their controls.

Structure	Thickness (mm)	Apparent density (g/cm^3)	Mesh porosity (%)
ePCL	0.075 ± 0.001	0.25 ± 0.01	77.16 ± 1.32
m_ePCL	0.067 ± 0.002	0.22 ± 0.01	80.10 ± 1.20
m_ePCL_Gel0.1	0.063 ± 0.001	0.23 ± 0.04	87.14 ± 2.13**
m_ePCL_Gel0.5	0.062 ± 0.002	0.23 ± 0.03	87.47 ± 1.74**
m_ePCL_Gel1	0.080 ± 0.001	0.25 ± 0.01	86.51 ± 0.49

** Represent statistical differences between m_ePCL_Gel0.0.1/ 0.5 and ePCL ($p \leq 0.01$).

The porosity of the fabricated meshes was consistently high, ranging from 77.16 ± 1.32% (ePCL) to 80.10 ± 1.20% (m_ePCL) for the control groups. After biofunctionalization with Gel, porosity increased compared to the control samples but remained similar among the different conditions: 87.14 ± 2.13% (0.1 wt%), 87.47 ± 1.74% (0.5 wt%), and 86.51 ± 0.49% (1 wt%). All samples demonstrated porosity within the optimal range reported in the literature for TE scaffolds, supporting efficient cell infiltration and nutrient diffusion.

4.3.1.2. Fourier Transform Infrared Spectroscopy with Attenuated Total Reflection

FTIR analysis was performed on modified ePCL nanofibers and Gel powder as a reference to assess the chemical composition of the fibers and examine the interaction between ePCL and Gel. The resulting spectra are presented in Figure 19.

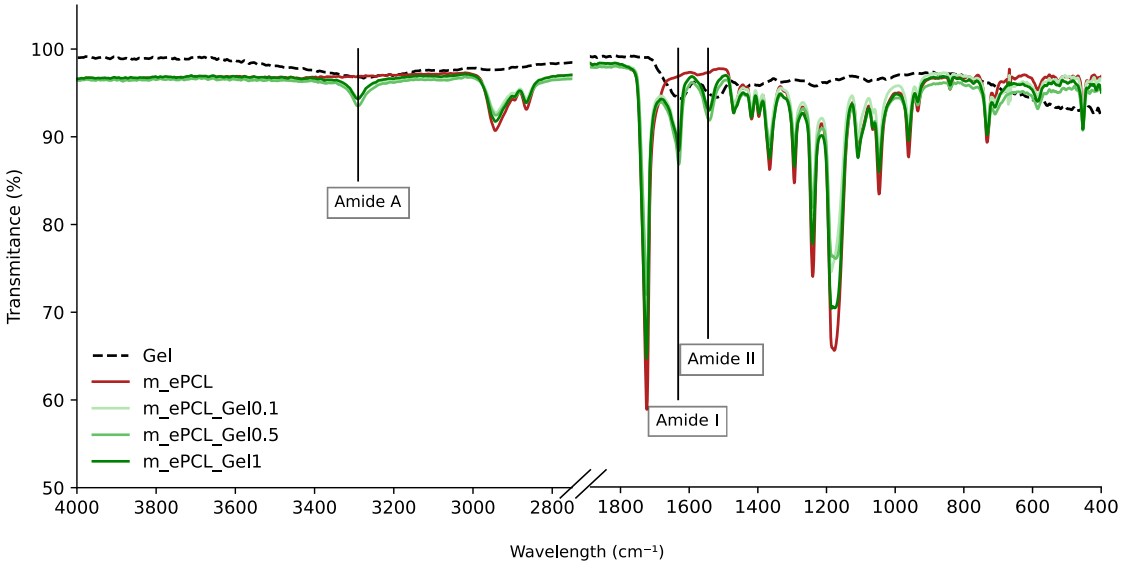

Figure 19 - FTIR spectra of modified ePCL with different concentrations of Gel and controls.

Although FTIR provides semi-quantitative information, the analysis was used to compare Gel biofunctionalized samples with ePCL meshes modified before biofunctionalization, rather than to determine the precise amount of Gel incorporated. Table 6 shows the characteristic FTIR bands of m_ePCL alongside those of m_ePCL_Gel and highlights several key bands that are attributable to Gel.

Table 6 - Comparison of characteristic FTIR bands of modified ePCL before and after Gel incorporation according to assignments reported elsewhere [90–94].

	Assignment	
Bands	**m_ePCL**	**m_ePCL_Gel**
3290 cm^{-1}	Absent	N-H stretching vibration – Amide A
1720 cm^{-1}	Moderate C=O	Decrease in intensity
1632 cm^{-1}	Absent	C=O stretching – Amide I
1545 cm^{-1}	Absent	N-H bending – Amide II
1240 cm^{-1}	Absent	C-N stretching – Amide III
1150 cm^{-1}	Weak	C-O-C vibration

The FTIR spectra displayed key characteristic bands of Gel, such as the broad peak around 3290 cm^{-1} attributed to N–H stretching vibrations linked to the amide bonds, known as Amide A. As previously noted, the typical PCL carbonyl band can be observed

at 1720 cm^{-1}, which diminished due to Gel coating. This can indicate coverage of the nanofiber's surface. Successful immobilization of Gel was further confirmed by the presence of the amide bands at 1632 cm^{-1} (Amide I), 1545 cm^{-1} (Amide II), and the shoulder at 1240 cm^{-1} (Amide III), the latter overlapping with PCL ester and polysaccharide vibrations. The strong glycosidic C–O–C signal at 1150 cm^{-1} also supported effective biofunctionalization across all Gel concentrations.

4.3.1.3. Scanning Electron Microscopy Analysis and Energy Dispersive X-ray Spectroscopy

SEM imaging of the ePCL meshes with varying Gel concentrations and their corresponding controls is presented in Figure 20 (A)–(E).

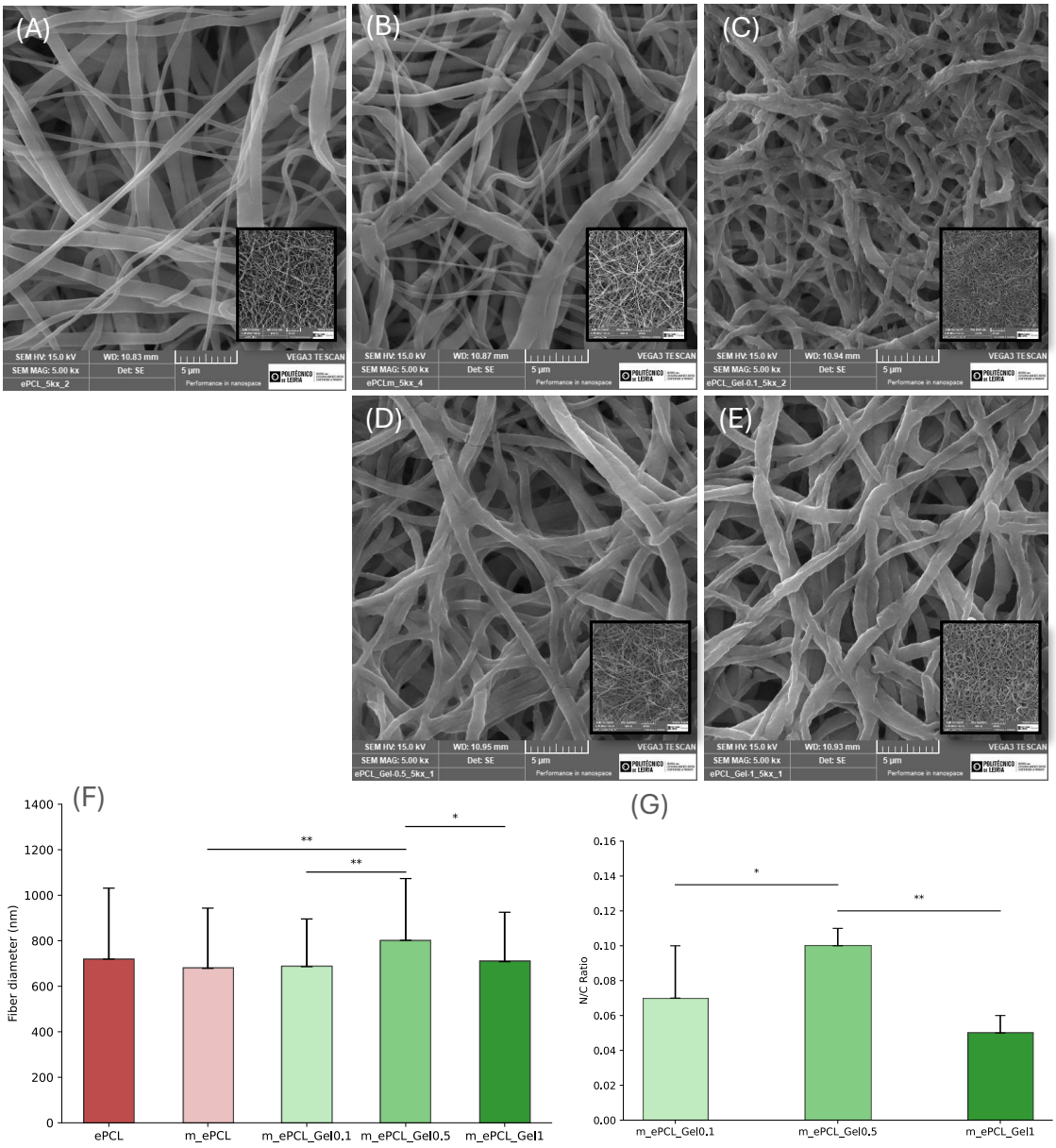

Figure 20 - SEM of ePCL (A): (B) – without biofunctionalization; (C) – with Gel 0.1 wt%; (D) – with Gel 0.5 wt%; (E) – with Gel 1 wt%; (F) comparative fiber average diameter; (G) comparative EDX. Statistical significance for $p \leq 0.05$ (*) and $p \leq 0.01$ (**).

Consistent with the previously described morphology, the control samples, ePCL and m_ePCL (Figure 20 (A) and 20 (B), respectively), displayed continuous bead-free fibers, with m_ePCL showing the slight surface changes already noted in the previous section. The meshes containing different Gel concentrations (0.1 wt%, 0.5 wt%, and 1 wt%; Figure 20 (C)–(E), respectively) demonstrate successful encapsulation of ePCL fibers without altering the overall mesh morphology or producing closed pores.

The comparative analysis (Figure 20 (F)) revealed an average fiber diameter of 719 ± 311 nm for ePCL and 678 ± 264 nm for m_ePCL. Incorporation of Gel increased fiber diameter, with values of 686 ± 209 nm, 801 ± 271 nm for 0.1 wt% and 0.5 wt%, respectively and then a decrease with a value of 708 ± 217 nm for 1 wt%, The increase in diameter in the 0.5 wt% condition was statistically significant compared with the control samples (m_ePCL), as well as with the other concentrations of Gel.

Lastly, EDX analysis was performed on the Gel biofunctionalized samples. The comparative assessment of N content (Figure 20 (G)) confirmed the presence of N atoms at 0.07 ± 0.03, 0.10 ± 0.01, and 0.05 ± 0.05 for 0.1 wt%, 0.5 wt%, and 1 wt% CS, respectively. These findings provide support for the SEM observations (higher fiber diameter for 0.5 wt% Gel) as the ePCL sample with 0.5 wt% Gel demonstrated a statistically significant N ratio in comparison with the other concentrations. At the highest concentration (1 wt%), the excess of gelatin may have promoted molecular aggregation and partial destabilization of reactive sites, reducing the number of amine groups available for covalent bonding. This results in heterogeneous deposition, and subsequent washing and drying leads to partial loss of the coating. This is consistent with the lower nitrogen signal detected by EDX and the reduced fibre diameter when compared to 0.5 wt%. Overall, the presence of N confirms the successful incorporation of Gel onto the fiber surfaces.

4.3.1.4. Water vapor transmission rate

As previously mentioned, the water vapor transmission rate (WVTR) plays a critical role in wound healing, and the produced meshes displayed values consistent with those reported for electrospun materials [96]. Results obtained for WVTR of ePCL with different concentrations of Gel and controls can be observed in Table 7.

Table 7 - WVTR of ePCL with different concentrations of Gel and controls.

Structure	WVTR (g/m^2/day)
ePCL	3302.00 ± 24.00
m_ePCL	3369.88 ± 47.35
m_ePCL_Gel0.1	3375.14 ± 17.97 **
m_ePCL_Gel0.5	3280.43 ± 77.03

m_ePCL_Gel1	3299.90 ± 27.44

** Represent statistical differences between m_ePCL_Gel0.1 and m_ePCL_Gel0.5 ($p \leq 0.01$).

The WVTR of the control meshes ranged from 3302.00 ± 24 g/m²/day (ePCL) to 3369.88 ± 47.35g/m²/day (m_ePCL), while biofunctionalization with Gel resulted in values of 3375.14 ± 17.97 g/m²/day (0.1 wt%), 3280.43 ± 77.03 g/m²/day (0.5 wt%), and 3299.90 ± 27.44 g/m²/day (1 wt%). A statistically significant difference was observed between ePCL with 0.1 wt% and 0.5 wt% Gel. Overall, the WVTR values remained within the expected range for TE scaffolds and were consistent with previous literature findings on ePCL and Gel-based wound dressings [98,112]. Although the WVTR values for the Gel-modified meshes are above the optimal range, this behaviour is typical of electrospun materials and results from their porous, hydrophilic nature, which promotes vapor diffusion and maintains suitable moisture for wound healing.

4.3.1.5. Contact angle measurements

As previously described, WCA analysis was performed to assess the surface wettability of the meshes at both 0 and 10 sec (Figure 21 (A)–(B)).

The ePCL meshes exhibited hydrophobic behaviour, with contact angles of 104.64 ± 2.01° at 0 sec and 102.71 ± 2.06° at 10 sec, indicating limited water uptake. In contrast, the hydrolyzed ePCL exhibited an increased degree of hydrophilicity over time, as evidenced by a reduced angle of 77.78 ± 14.94° at 10 sec. This observation is consistent with the introduction of polar –OH and –COOH groups resulting from surface modification. The incorporation of Gel progressively increases the WCA. Namely, ePCL with Gel at 0.1 wt% and 0.5 wt% resulted in slightly more hydrophilic surfaces after both 0 sec (74.61 ± 5.61° and 98.44 ± 10.27°, respectively) and 10 sec (41.37 ± 14.07° and 71.23 ± 17.99°, respectively) when compared with hydrolyzed ePCL meshes.

Despite Gel's inherent hydrophilic properties, its binding to carboxyl groups (–COOH) may neutralize some highly hydrophilic sites on m_ePCL. Furthermore, Gel may form clusters of polar groups or interact with the polymer matrix, thereby limiting the enhancement of overall wettability. At the highest Gel concentration (1 wt%), the meshes displayed predominantly hydrophobic characteristics, with angles of 114.99 ± 13.08° (0 sec) and 98.65 ± 12.67° (10 sec). It has been demonstrated that an increase in Gel concentration can, paradoxically, promote hydrophobicity in nanofibrous materials if molecular orientation favours exposure of non-polar groups at the surface.

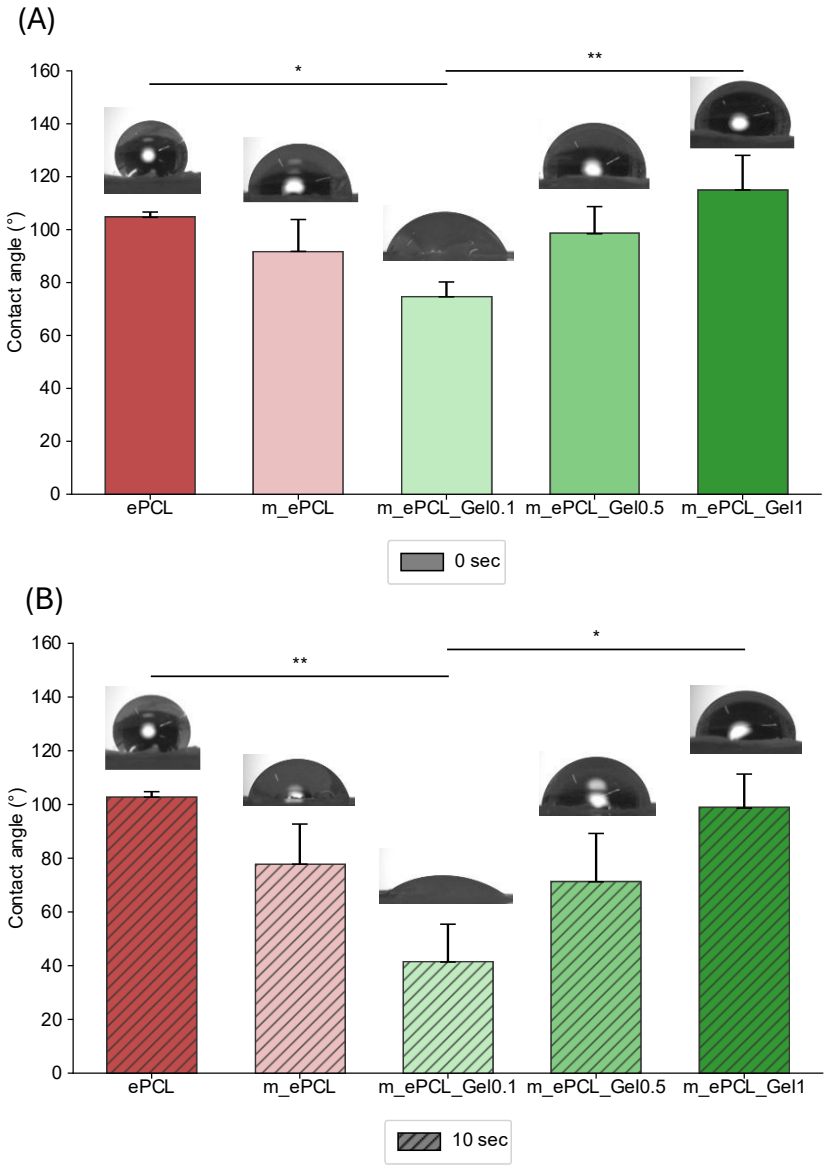

Figure 21 - WCA of ePCL with different concentrations of Gel and controls with corresponding images: (A) - at 0 sec; (B) - at 10 sec. Statistical significance for $p \leq 0.05$ (*) and $p \leq 0.01$ (**).

4.3.2. Mechanical performance – Tensile test

The mechanical performance of ePCL meshes with varying Gel concentrations was assessed by examining their structural compositions. As previously detailed, reference values for human skin mechanics span a wide range, with YM between 0.05–150 MPa, TSB from 1–32 MPa, and EB from 17–207% [103–106]. Figure 22 (A)–(D) presents the corresponding stress-strain curves and mechanical parameters, with both control and modified ePCL meshes evaluated. Notably, ePCL demonstrates favourable mechanical results (YM = 0.02 ± 0.0 MPa; EB = 323.16 ± 15.08%; TSB = 1.82 ± 0.10 MPa), making it suitable as a skin substitute from the mechanical point of view. Gel integration is primarily intended to enhance cellular adhesion, migration, and proliferation by providing biological cues.

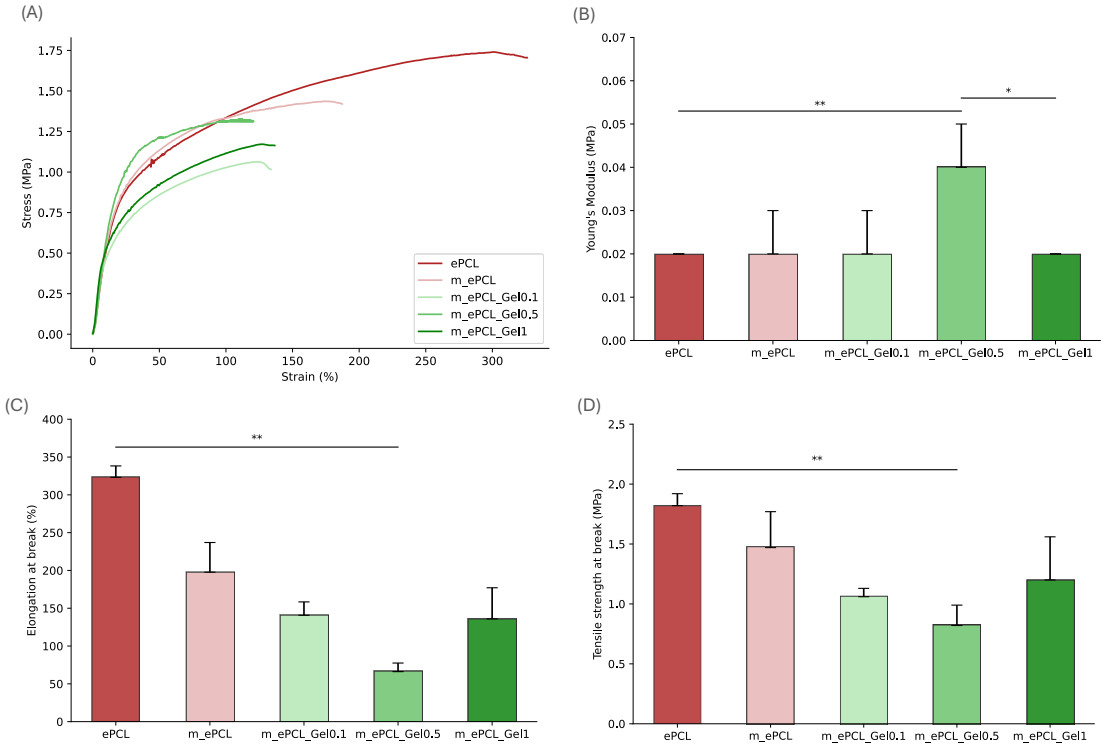

Figure 22 - Mechanical behaviour at wet state of ePCL with different concentrations of Gel and controls, (A) – Stress-strain representative curves; (B) – Young's Modulus (MPa); (C) – Elongation at break (%); (D) – Tensile strength at break (MPa). Statistical significance for $p \leq 0.05$ (*) and $p \leq 0.01$ (**).

Stress–strain profiles demonstrated that ePCL sustained higher stress values throughout deformation, whereas Gel-modified formulations exhibited curves shifted downward, indicating reduced overall mechanical performance (Figure 22 (A)). Quantitatively, YM (Figure 22 (B)) exhibited a concentration-dependent effect: at 0.1 wt% Gel (YM = 0.02 ± 0.1 MPa), elasticity was maintained when compared to ePCL, whereas at 0.5 wt% Gel (YM = 0.04 ± 0.1 MPa), the elasticity increased significantly (Figure 22 (B)). On the other hand, the 1 wt% Gel formulation exhibited a reduction in YM again (YM = 0.02 ± 0.1 MPa) compared to the 0.5 wt% formulation. This trend can be correlated with the increase in fiber diameter observed by SEM, indicating the formation of a more continuous and cohesive Gel coating at this intermediate concentration. At 0.5 wt%, the polymer-Gel interphase is likely to have promoted enhanced inter-fibre adhesion and friction, leading to a stiffer overall network. Conversely, at 0.1 wt%, the Gel content was insufficient to establish a uniform coating, resulting in a limited mechanical reinforcement. At the highest concentration (1 wt%), the excess of Gel may have promoted molecular aggregation and partial destabilization of reactive sites, reducing the number of amine groups available for covalent bonding [113]. A marked decline for all Gel-modified samples (0.1 wt%; 0.5 wt%; 1 wt%) was exhibited for the EB (140.71 ± 17.68 %; 66.16 ± 11.36 %; 135.91 ± 41.17 %, respectively) (Figure 22 (C)) and TSB (1.06 ± 0.07 MPa;

0.82 ± 0.17 MPa; 1.20 ± 0.36 MPa, respectively) (Figure 22 (D)) when compared with ePCL, with the most substantial reduction evident at 0.5 wt% Gel. Among all the conditions tested, 1 wt% Gel is the one that most closely mimics the mechanical properties of skin.

4.3.3. *In vitro* studies

4.3.3.1. Cytotoxicity

Similarly to the previous biomolecule, cytotoxicity of the produced ePCL meshes was assessed at the highest Gel concentration (1 wt%) alongside controls, including ePCL and modified ePCL, since testing the maximum incorporation is sufficient to determine whether Gel addition introduces cytotoxicity. Both IC and DC methods were employed to evaluate cell viability (Figure 23 (A)-(B)). As previously reported, the IC involved exposing cells to media pre-conditioned by the meshes, avoiding direct material-cell contact. In contrast, the DC placed the meshes in physical contact with the cells during incubation. Cytotoxicity was determined based on metabolic activity below 70%.

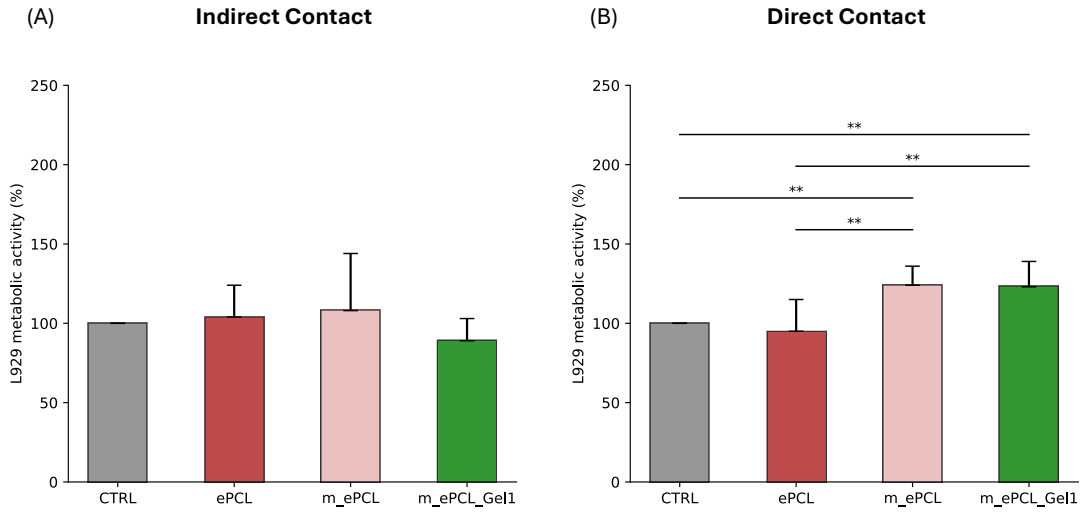

Figure 23 - Cytotoxicity assessment of ePCL with Gel at 1 wt% and controls. (A) IC and (B) DC with L929 cell line, for 24h. The positive control consisted of cells growing in the well without samples. Statistical significance for $p \leq 0.01$ (**).

Building on the previously reported non-cytotoxic controls, the 1 wt% Gel biofunctionalized ePCL mesh was further evaluated. In the IC assay (Figure 23 (A)), fibroblast metabolic activity remained above the cytotoxicity threshold, with the Gel 1 wt% sample showing 89 ± 14% viability, comparable to the control groups (ePCL: 104 ± 20%; modified ePCL: 108 ± 36%). The DC assay (Figure 23 (B)) supported these findings, with Gel 1 wt% meshes producing a notable increase in metabolic activity (123 ± 16%), exceeding both ePCL (95 ± 20%) and modified ePCL (124 ± 12%) controls,

suggesting enhanced cell proliferation or viability afforded by Gel functionalization at this concentration. Thus, concentrations of 1wt% and above were considered non-toxic.

4.3.3.2. Cell metabolic activity and proliferation

The proliferation of L929 cells after 1, 3, 7, and 14 days of culture on ePCL meshes biofunctionalized with Gel (for all conditions) was assessed using a metabolic activity assay (Figure 24).

Overall, the L929 cells demonstrated a consistent increase in activity over the 14-day period, which was statistically significant when compared with the control. Almost all samples showed statistical significance at day 3 compared to day 1 within their own condition, except 0.1 wt% Gel sample. Only the sample containing 0.1 wt% Gel and ePCL sample presented differences at day 7 compared to the previous time-point. Additionally, only the sample with 1 wt% Gel showed statistical significance at day 14 compared to day 7. These results may be explained by the fact that, up to day 7, cells prefer samples with higher mechanical properties, whereas after that point, the samples containing the RGD sequence provided by Gel seem to be more attractive, leading to higher metabolic activity.

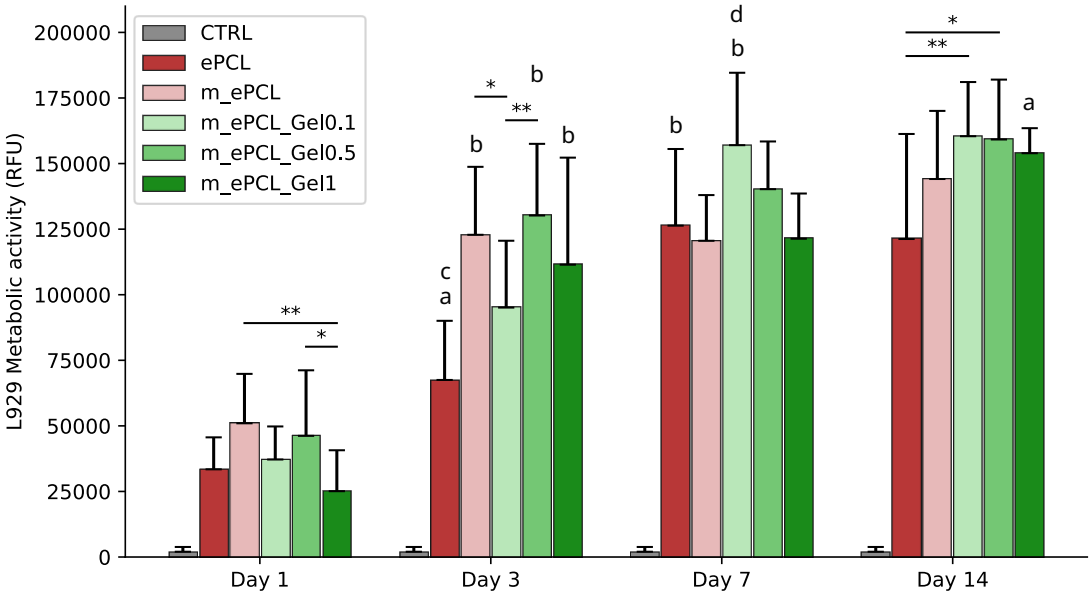

Figure 24 - Metabolic activity of L929 cells on ePCL with different concentrations of Gel and controls through 1, 3, 7 and 14 days after seeding, using an ePCL mesh without cells as a control for the experiment. Statistical significance for p ≤ 0.05 (*) and p ≤ 0.01 (**); Statistical significance with the previous time-point of p ≤ 0.05 (a); Statistical significance with the previous time-point of p ≤ 0.01 (b); Statistical significance with m_ePCL_Gel0.5/1 and m_ePCL (**)(c); Statistical significance with m_ePCL (**), m_ePCL_Gel1 (*) and ePCL (*) (d).

On day 1, comparing all conditions, the metabolic activity is generally low, likely cells are still adhering and adapting to the fiber surface. Consistent with literature, the hydrophobic nature of PCL led to lower cell activity compared to other samples [110]. In contrast, modified ePCL demonstrated enhanced cell affinity due to its polar groups, resulting in increased hydrophilicity and correspondingly higher metabolic activity at all time points relative to ePCL.

On day 1, most of Gel-containing samples showed higher metabolic activity compared to the ePCL control, highlighting an early beneficial effect of Gel on cell viability. By day 3, the 0.5 wt% Gel group exhibited the highest metabolic activity, outperforming both lower (0.1 wt%) and higher (1 wt%) Gel concentrations, as well as the control groups. At day 7, the enhanced activity was observed in the 0.1 wt% Gel, and by day 14, all Gel concentrations had demonstrated equivalent metabolic activity. This indicates that, over an extended period, all concentrations effectively promote fibroblast metabolic function. Gel has been demonstrated to provide multiple integrin-binding sites, which have been shown to enhance cellular metabolic activity [110]. Therefore, the incorporation of Gel was expected to yield greater biological activity compared to single ePCL meshes.

4.3.3.3. Cell morphology and fibronectin deposition

Representative SEM images (Figure 25) illustrate the time-course of L929 cell proliferation on ePCL meshes containing different concentrations of Gel.

In accordance with the metabolic activity observed, cell attachment was minimal for all groups on day 1, which is typical of the initial post-seeding period. By day 3, cell number increased, and it was possible to observe the development of an interconnected cellular network for all samples containing Gel and for the mPCL.Progressing to days 7 and 14, substantial cellular proliferation and a dense cell sheet become evident. The Gel functionalized samples (especially with 0.5 wt% and 1 wt%) exhibit extensively colonized surfaces with matrix-like networks, whereas the control and lower Gel concentration samples show less pronounced cell coverage. These observations corroborate earlier findings with the proliferation assay, emphasizing the role of Gel in enhancing scaffold hydrophilicity and bioactivity, thus facilitating robust cell attachment, proliferation, and matrix development over time. Additionally, the 1 wt% Gel sample, at day 14, presented a cell sheet integrated with the electrospun meshes, clearly demonstrating successful cell infiltration throughout the structure. This finding indicates that Gel modification creates a more biologically supportive microenvironment for fibroblasts, validating its application in TE structures, as evidenced by both qualitative (SEM) and quantitative assays previously discussed.

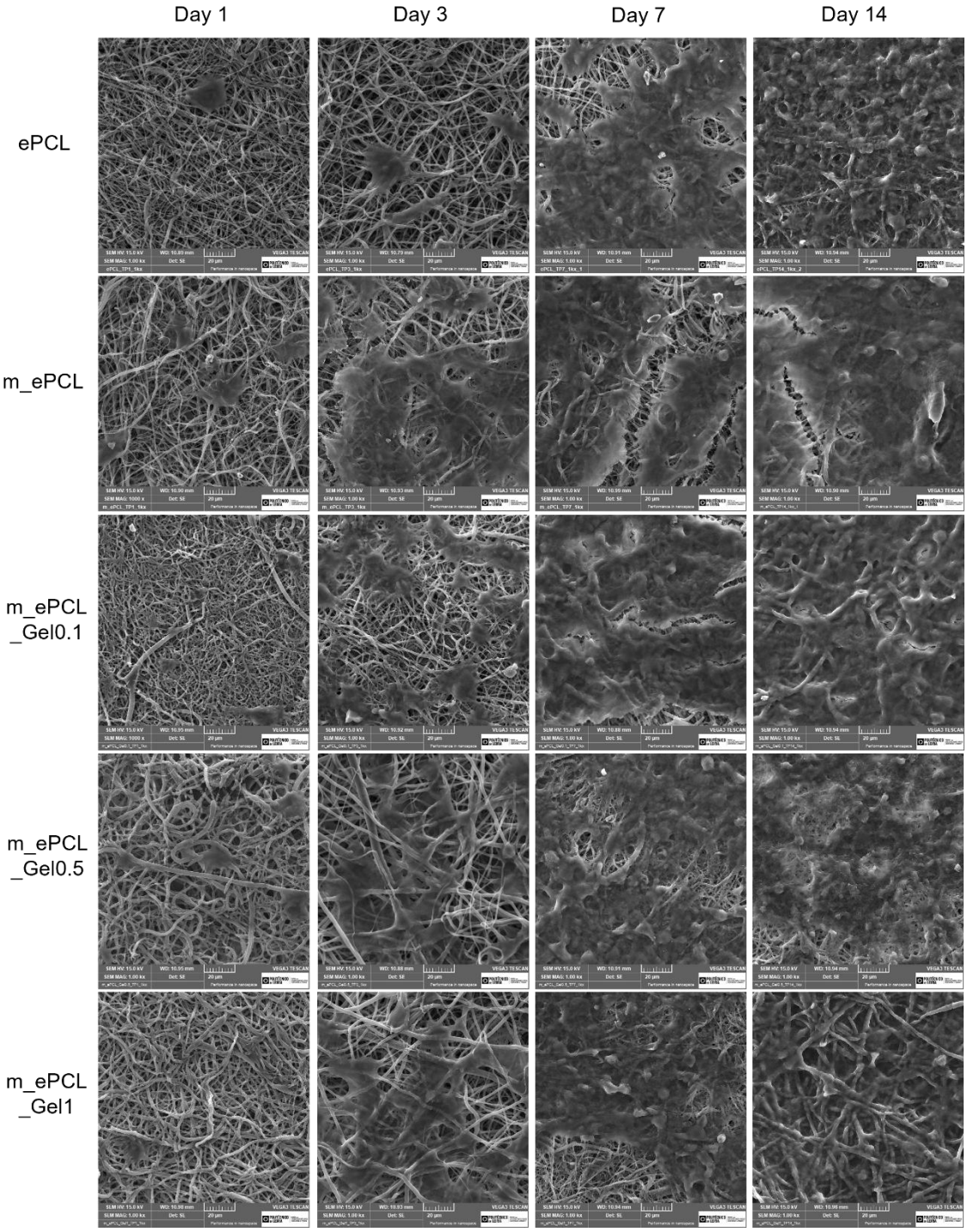

Figure 25 - Representative proliferation SEM images of L929 cells evaluated at 1, 3, 7 and 14 days of study after seeding in ePCL with different concentrations of Gel and controls. Scale bars correspond to 20 μm.

Representative confocal microscopy images (Figure 26) further validate the dynamic proliferation of L929 cells and ECM development on ePCL based scaffolds modified with different concentrations of Gel, extending observations already discussed. At day 1, cells remain relatively isolated, with distinct, blue-stained nuclei and minimal red actin filaments, reflecting early-stage adhesion. By day 3, cell numbers and spreading increase, but the FN formation remains residual for Gel samples. On days 7

and 14, Gel-functionalized meshes showed dense populations of cells, well-developed actin cytoskeletons, and strong, interconnected FN networks, consistent with improved scaffold biocompatibility and matrix synthesis.

In contrast, ePCL exhibits comparatively limited cell proliferation, cytoskeletal organization, and FN deposition throughout the period. Confocal images of individual stains for nuclei, actin, and FN can be found in Figures 37A – 37B and Figures 42B – 44B of the appendix section.

These results are congruent with prior discussion, highlighting Gel's role in promoting cell adhesion, proliferation, and ECM assembly. The visualization of nuclei, actin cytoskeleton, and FN together underscores how scaffold modification creates an optimal microenvironment for both cellular expansion and functional tissue integration, which are key indicators of successful TE scaffolds.

For Gel, 1 wt% represents the most suitable concentration. This formulation demonstrated mechanical properties that more closely resembled those of native skin, while also supporting a consistent increase in metabolic activity throughout the culture period. Notably, a clear distinction was observed between the metabolic activity on days 7 and 14. Despite being more hydrophobic, likely due to a lower relative incorporation of Gel as indicated by EDX analysis, the 1 wt% samples displayed a stable and interesting behaviour, combining hydrophobicity with elasticity values. In contrast, 0.1 wt% and 0.5 wt% resulted in only a slight enhancement of wettability and a limited increase in elasticity. The findings of this study indicate that, by aligning both mechanical performance and biological response, 1 wt% Gel can be regarded as the optimal loading.

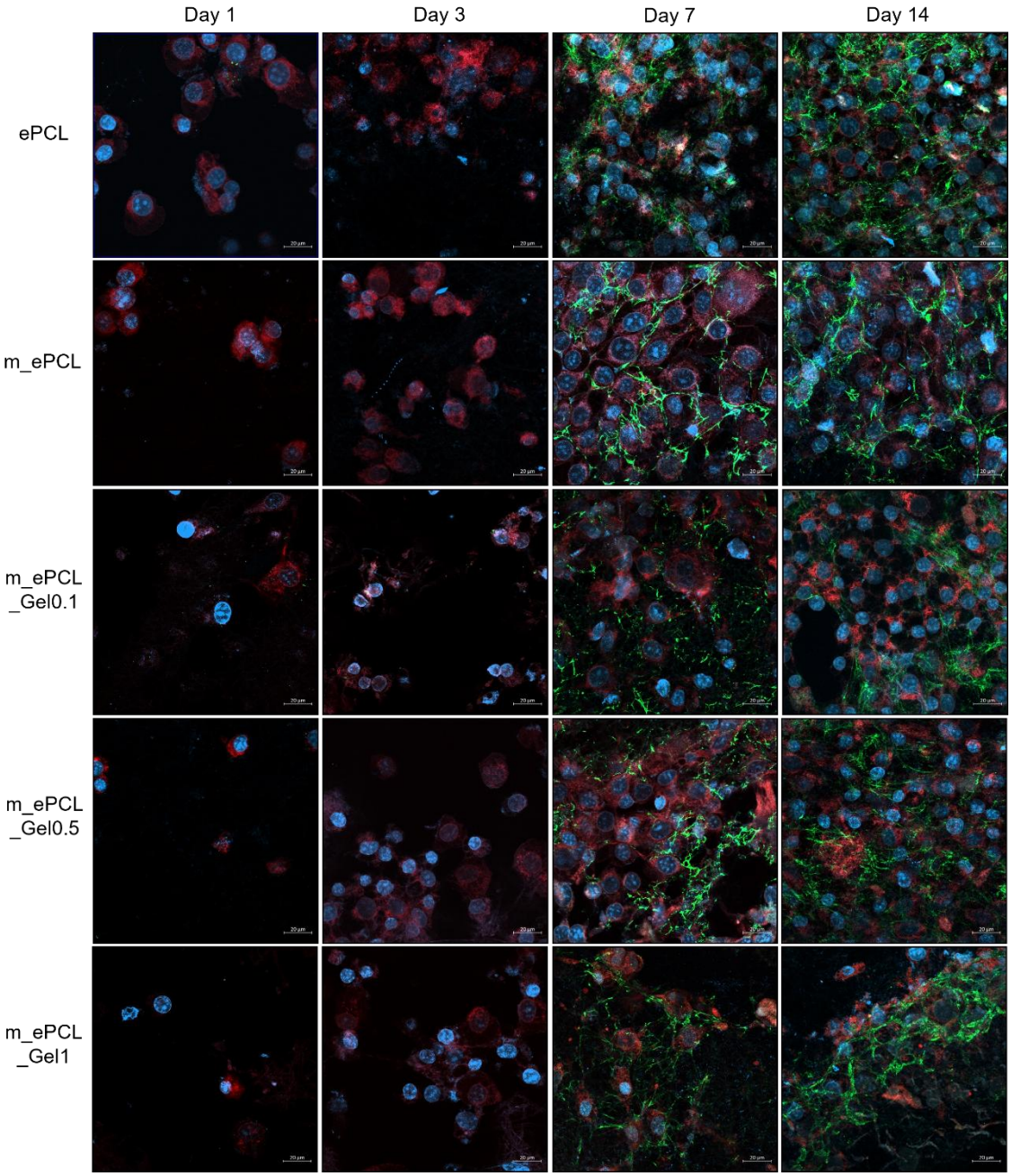

Figure 26 - Representative proliferation confocal images of L929 cells evaluated at 1, 3, 7 and 14 days of study after seeding in ePCL with different concentrations of Gel and controls (blue: nuclei; red: actin; green: FN). Scale bars correspond to 20 μm.

4.4. ePCL meshes modified with Arginine

4.4.1. Physico-chemical characterization

4.4.1.1. Apparent Density and Porosity

Equations (1) and (2) were also employed to calculate the theoretical porosity, apparent density, and thickness of the ePCL meshes biofunctionalized with Arg and their corresponding controls, and the results are summarized in Table 8.

Table 8 - Properties of ePCL meshes with Arg at different concentrations and their controls.

Structure	Thickness (mm)	Apparent density (g/cm^3)	Mesh porosity (%)
ePCL	0.075 ± 0.001	0.25 ± 0.01	77.16 ± 1.32
m_ePCL	0.067 ± 0.002	0.22 ± 0.01	80.10 ± 1.20
m_ePCL_Arg0.5	0.075 ± 0.002	0.18 ± 0.06	92.37 ± 2.62**
m_ePCL_Arg1	0.064 ± 0.000	0.20 ± 0.02	91.59 ± 0.99**
m_ePCL_Arg2	0.059 ± 0.001	0.28 ± 0.07	88.48 ± 2.76

** Represent statistical differences between m_ePCL_Arg0.5/ 1 and ePCL ($p \leq 0.01$).

The fabricated meshes exhibited consistently high porosity, ranging from 77.16 ± 1.32% (ePCL) to 80.10 ± 1.20% (m_ePCL) in the control samples. Following biofunctionalization with Arg, porosity values are higher, measuring 92.37 ± 2.62% (0.5 wt%), 91.59 ± 0.99% (1 wt%), and 88.48 ± 2.76% (2 wt%). All formulations have thus fallen within the literature-reported optimal porosity range for TE scaffolds, ensuring favourable conditions for cell infiltration and nutrient diffusion.

4.4.1.2. Fourier Transform Infrared Spectroscopy with Attenuated Total Reflection

To assess the chemical composition of the fibers and examine the interaction between ePCL and Arg, FTIR analysis was performed on modified ePCL nanofibers and Arg powder as a reference. The obtained spectra are displayed in Figure 27.

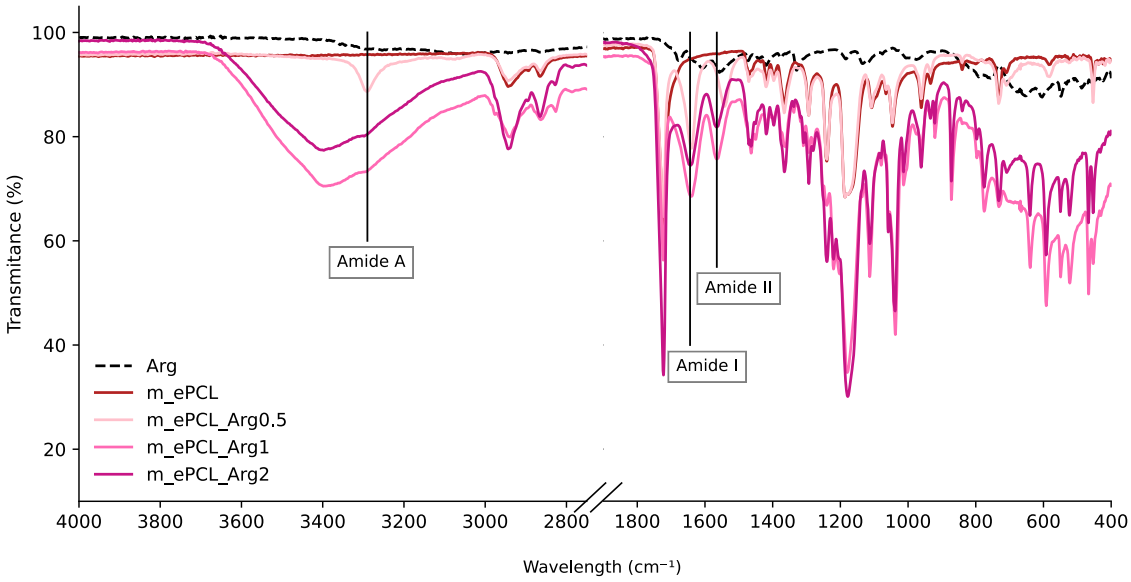

Figure 27 - FTIR spectra of modified ePCL with different concentrations of Arg and controls.

Given the qualitative nature of FTIR, the technique served to assess differences between Arg functionalized samples and ePCL meshes subjected to prior modification,

without attempting to quantify the Arg content. Table 9 summarises the characteristic FTIR bands observed for m_ePCL and m_ePCL_Arg, including Arg specific bands.

Table 9 - Comparison of characteristic FTIR bands of modified ePCL before and after Arg incorporation according to assignments reported elsewhere [90–94].

	Assignment	
Bands	**m_ePCL**	**m_ePCL_Arg**
3290 cm^{-1}	Absent	O-H and N-H stretching vibration
1720 cm^{-1}	Moderate C=O	Decrease in intensity
1644 cm^{-1}	Absent	C=O stretching – Amide I
1560 cm^{-1}	Absent	N-H bending – Amide II
1220 cm^{-1}	Absent	C-N stretching – Amide III
1150 cm^{-1}	Weak	Overlapping C-O-C and C-N stretching vibration

As previously mentioned, all the band ranges cited in the literature have already been discussed in another section [90–94]. Characteristic FTIR bands confirming Arg presence included the broad 3290 cm^{-1} peak from O–H and N–H stretching related to hydrogen bonding, and the reduced intensity of the PCL carbonyl band at 1720 cm^{-1} due to likely surface coverage by Arg. The amide I (1644 cm^{-1}), amide II (1560 cm^{-1}), and overlapping amide III region (1220 cm^{-1}) were all evident, confirming successful Arg immobilization for all concentrations despite spectral overlap with PCL ester and polysaccharide vibrations. Additionally, the prominent 1150 cm^{-1} can be attributed to overlapping C-O-C and C-N stretching vibrations, from the PCL ester groups and the guanidium group in Arg, respectively, further substantiating Arg biofunctionalization on modified ePCL surfaces at all tested concentrations [114].

4.4.1.3. Scanning Electron Microscopy Analysis and Energy Dispersive X-ray Spectroscopy

SEM morphological images of ePCL meshes for the different concentrations of Arg and controls are shown in Figure 28 (A)-(E).

As previously discussed, the control meshes (Figure 28 (A)–(B)) present continuous bead-free fibers, while the addition of Arg at different concentrations (0.5 wt%, 1 wt%, and 2 wt%; Figure 28 (C)–(E)) resulted in effective encapsulation of ePCL nanofibers without altering mesh morphology.

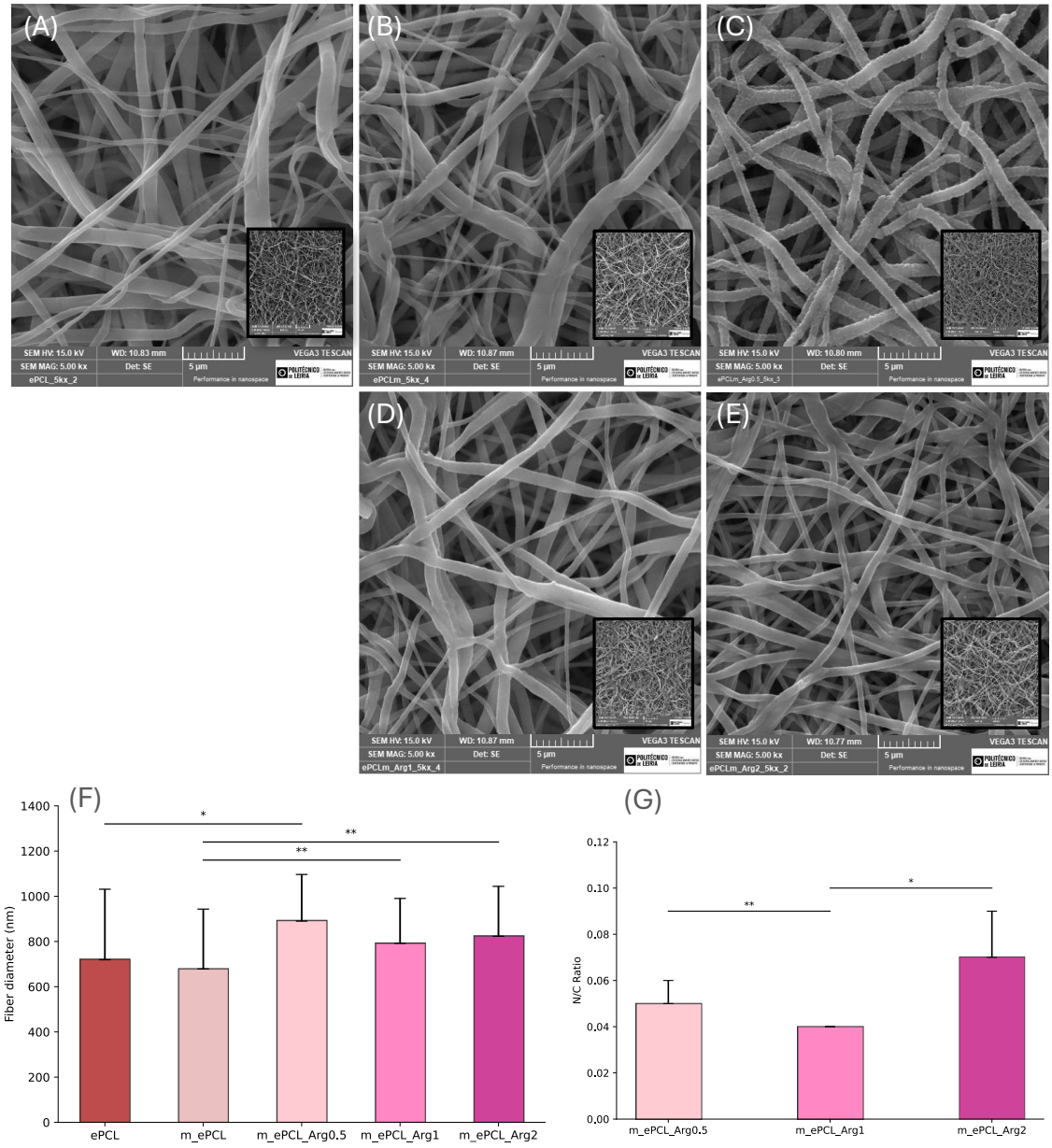

Figure 28 - SEM of ePCL (A): (B) – without biofunctionalization; (C) – with Arg 0.5 wt%; (D) – with Arg 1 wt%; (E) – with Arg 2 wt%; (F) comparative EDX analysis; (G) comparative fiber average diameter. Statistical significance for $p \leq 0.05$ (*) and $p \leq 0.01$ (**).

Comparative analysis (Figure 28 (F)) indicated average fiber diameters of 719 ± 311 nm for ePCL and 678 ± 264 nm for m_ePCL. Upon Arg incorporation, fiber diameter increased to 890 ± 206 nm, 792 ± 199 nm, and 823 ± 221 nm for 0.5 wt%, 1 wt%, and 2 wt%, respectively. Statistical significance was observed between the control groups and ePCL with Arg at 0.5 wt% and 2 wt%.

EDX analysis further confirmed the incorporation of Arg in the biofunctionalized samples. The N content (Figure 28 (G)) was measured as 0.05 ± 0.01, 0.04 ± 0.00, and 0.07 ± 0.02 for 0.5 wt%, 1 wt%, and 2 wt% Arg, respectively. The 1 wt% Arg sample exhibited a statistically lower N signal compared with the other concentrations. Overall,

the consistent detection of N atoms confirms the successful incorporation of Arg onto the fiber surface.

4.4.1.4. Water vapor transmission rate

The WVTR measurements of the fabricated meshes are presented in Table 10, demonstrating values consistent with those typically reported for electrospun based wound dressings.

Among the control groups, WVTR ranged from 3302.00 ± 24 g/m²/day for ePCL to 3369.88 ± 47.35 g/m²/day for m_ePCL. Incorporation of Arg showed a slight but progressive increase, with values of 3398.81 ± 62.55 g/m²/day (0.5 wt%), 3335.68 ± 25.78 g/m²/day (1 wt%), and 3344.10 ± 35.99 g/m²/day (2 wt%). Statistical analysis revealed a significant difference between modified ePCL and ePCL containing 0.5 wt% Arg, indicating that Arg content influenced vapor permeability.

Table 10 - WVTR of ePCL with different concentrations of Arg and controls.

Structure	WVTR (g/m²/day)
ePCL	3302.0 ± 24.0
m_ePCL	3369.88 ± 47.35
m_ePCL_Arg0.5	3398.81 ± 62.55 **
m_ePCL_Arg1	3335.68 ± 25.78
m_ePCL_Arg2	3344.10 ± 35.99

** Represent statistical differences between m_ePCL_Arg0.5 and ePCL ($p \leq 0.01$).

Despite these variations, all formulations exhibited WVTR values comparable to those reported in literature for electrospun systems and considerably higher than of those of conventional hydrocolloid or foam dressings, further reinforcing their suitability for TE applications. The slightly elevated WVTR of the Arg-functionalized meshes reflects the open fibrous structure and hydrophilic surface chemistry of these materials, ensuring balanced moisture exchange beneficial for TE.

4.4.1.5. Contact angle measurements

Wettability assessment through WCA measurements (Figure 29 (A)–(B)) revealed clear differences between the control and Arg biofunctionalized meshes.

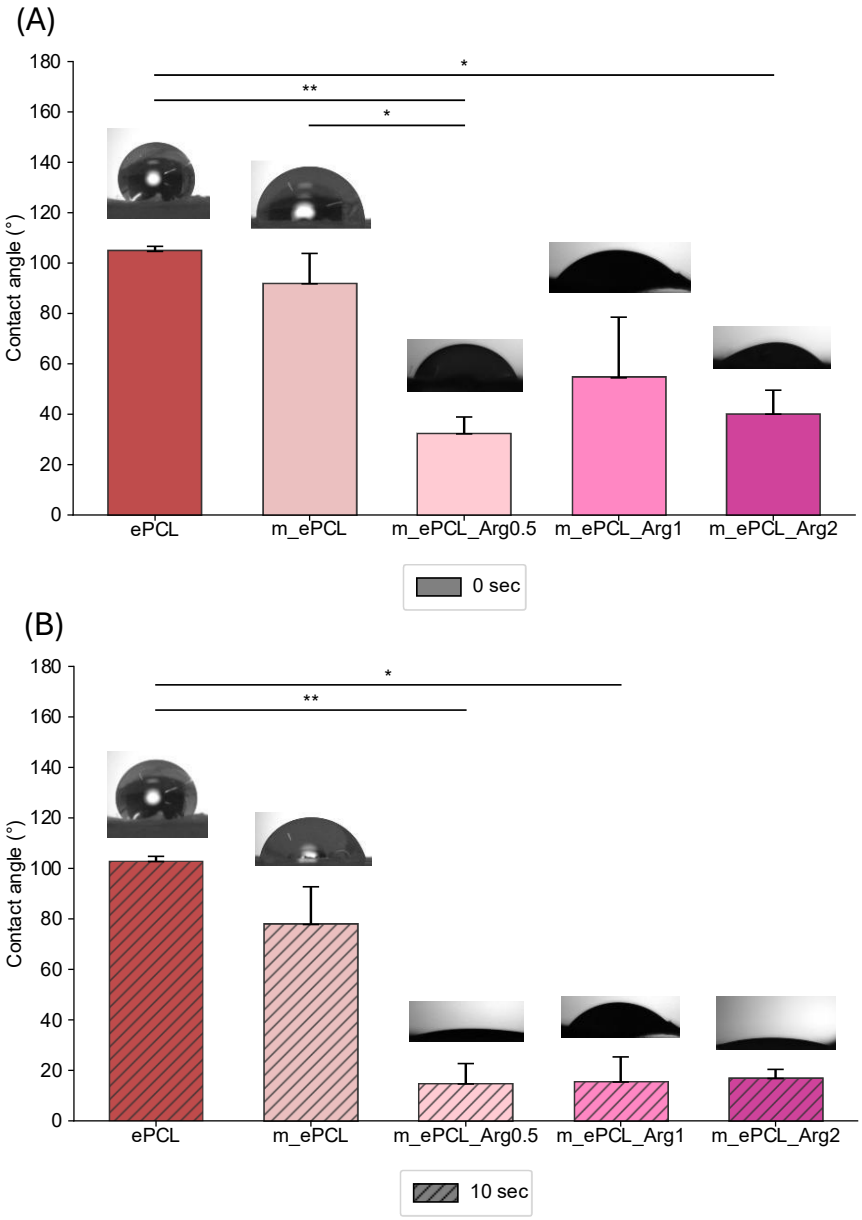

Figure 29 - WCA of ePCL with different concentrations of Arg and controls with corresponding images: (A) - at 0 sec; (B) - at 10 sec. Statistical significance for $p \leq 0.05$ (*) and $p \leq 0.01$ (**).

The ePCL meshes maintained a hydrophobic character, with contact angles above 90° at both 0 and 10 sec (104.64 ± 2.01° and 102.71 ± 2.06°, respectively). In contrast, hydrolyzed ePCL exhibited increased hydrophilicity at 10 sec (77.78 ± 14.94°), reflecting the surface modification associated with –OH and –COOH group exposure. Following Arg incorporation, all concentrations resulted in overall highly hydrophilic structures. At 0.5 wt%, 1 wt%, and 2 wt% Arg, the meshes presented very low contact angles both at 0 sec (32.19 ± 6.72°, 54.44 ± 24.08° and 40.03 ± 9.50°, respectively) and

at 10 sec (14.62 ± 8.07°, 15.39 ± 9.94° and 16.77 ± 3.62°, respectively). These values confirm rapid water spreading across the surface, strongly indicative of enhanced wettability. Therefore, Arg biofunctionalization promotes significant improvement in scaffold hydrophilicity compared to both untreated and hydrolyzed ePCL. This increased water affinity is of particular importance for biomedical applications, as higher surface wettability supports cell adhesion, proliferation, and migration, thereby optimising the scaffold's potential for TE and wound healing applications [90].

4.4.1.6. Biomolecule attachment quantification

A reverse quantification through NHN assay was assessed using UV/Vis for all Arg concentrations. As expected, higher Arg amount (wt%) incorporated into the modified ePCL meshes resulted in lower attachment efficiency (%), as can be observed in Table 11. For instance, at Arg 0.5 wt%, the biomolecule attachment quantification was 100%, since no waste was quantified after biofunctionalization. Therefore, assuming that the final mesh has precisely 0.5 wt% of Arg, it can be deduced that the amount of Arg in the final mesh is precisely 0.5 wt%. In the structure with 1 wt% Arg, a waste of 0.25 ± 0.05% was observed in the well, indicating an approximate mesh content of 0.75 ± 0.05% (0.0016g) Arg. This process results in a biomolecule attachment quantification of 75%. Finally, at the structure with 2 wt% Arg, a waste of 0.65 ± 0.24% was observed in the well, indicating that only 1.35 ± 0.24% (0.0023g) of Arg was present in the mesh. Conversely, this indicates that the attachment efficiency of the biomolecule was 67.5%.

Table 11 - Arg attachment quantification through the NHN assay.

Structure	Quantity of Arg (wt%)	Initial Arg mass (g)	Arg mass attached (g)	Attachment efficiency (%)
m_ePCL_Arg0.5	0.5	0.001	0.001	100
m_ePCL_Arg1	1	0.002	0.0016	75
m_ePCL_Arg2	2	0.004	0.0023	67.5

Arg incorporation without any waste may be optimal between Arg 0.5 wt% and Arg 1 wt%, since the biomolecule becomes wasteful when there are no more carboxylic groups available for conversion into amide groups. However, it should be noted that at Arg 2 wt%, a greater quantity of Arg is incorporated in grams.

4.4.2. Mechanical performance – Tensile test

Mechanical characterization of ePCL meshes incorporating different Arg concentrations is shown in Figure 30 (A)-(D). Human skin's mechanical attributes are highly variable, with benchmarks ranging from 0.05–150 MPa for YM, 17–207% for EB,

and1–32 MPa for TSB, as earlier reported [103–106]. The mechanical parameters for control and biofunctionalized ePCL meshes are illustrated in the stress–strain curves and corresponding graphs. The ePCL mesh displays optimal values (YM = 0.02 ± 0.0 MPa; EB = 323.16 ± 15.08%; TSB = 1.82 ± 0.10 MPa), and addition of Arg is intended to enhance its structural resilience, aligning its properties more closely with those of native skin.

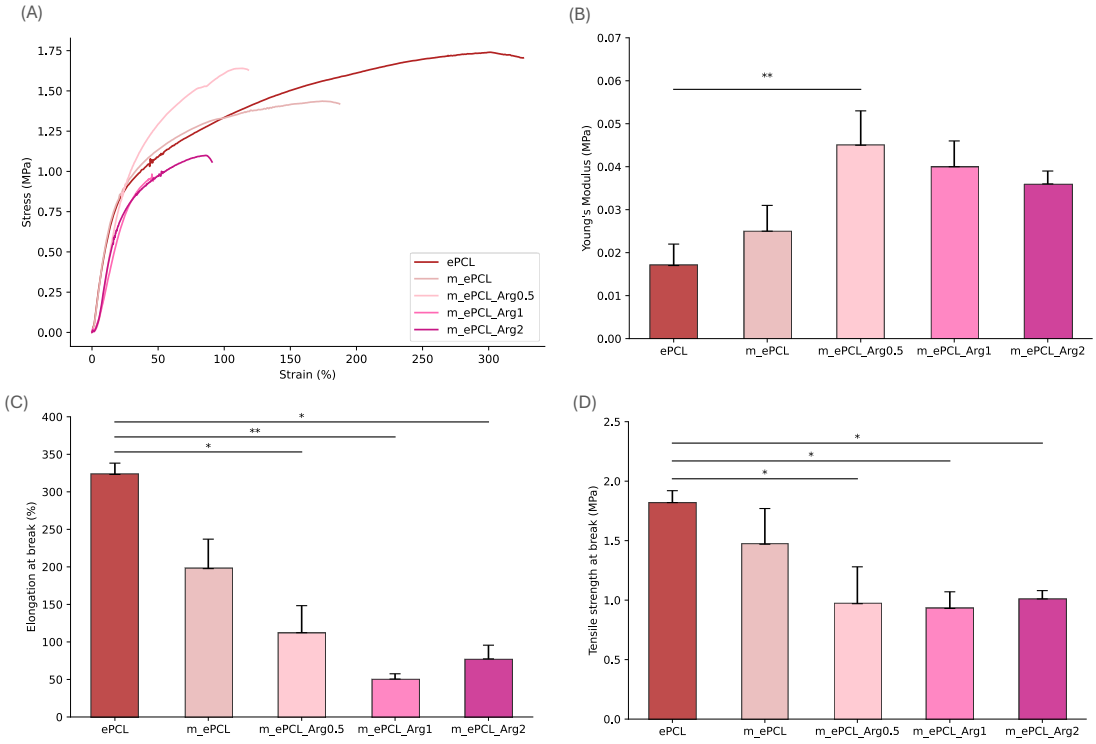

Figure 30 - Mechanical behaviour at wet state of ePCL with different concentrations of Arg and controls, (A) – Stress-strain representative curves; (B) – Young's Modulus (MPa); (C) – Elongation at break (%); (D) – Tensile strength at break (MPa). Statistical significance for p ≤ 0.05 (*) and p ≤ 0.01 (**).

The stress-strain curves (Figure 30 (A)) demonstrate that the incorporation of Arg modifies the mechanical response of the meshes. A quantitative analysis was conducted, which revealed a statistically significant augmentation in YM (0.05 ± 0.01 MPa; 0.04 ± 0.01 MPa; 0.04 ± 0.0 MPa) (Figure 30 (B)) in all Arg-containing samples (0.5 wt%; 1 wt%; 2 wt%, respectively). This augmentation was particularly evident at the lowest concentration of 0.5 wt%. This finding suggests that Arg incorporation leads to a less elastic structure, which may be attributed to the formation of intermolecular hydrogen bonds between the different conjugated Arg molecules and the ePCL matrix, which increases the material's resistance to elastic deformation. Similarly, EB (112.33 ± 36 %; 50.53 ± 7.03 %; 77.40 ± 18.27 %) (Figure 30 (C)) was found to be significantly reduced in all Arg-modified scaffolds (0.5 wt%; 1 wt%; 2 wt%, respectively), with the lowest elongation being observed in the 1 wt% sample. This reduction indicates that Arg

impedes the capacity of the scaffolds to stretch, presumably due to the disruption of polymer continuity.

All Arg-containing scaffolds (0.5 wt%; 1 wt%; 2 wt%) demonstrated a significant decline in mechanical strength in comparison to ePCL (*p < 0.05) when considering TSB (0.97 ± 0.31 MPa; 0.93 ± 0.14 MPa; 1.01 ± 0.07 MPa, respectively) (Figure 30 (D)) In this case, the TSB was maintained at different concentrations of Arg. Compared to the mechanical properties of human skin, the Arg samples (for all conditions) match the reference values for EB but are slightly below the target values for YM and TSB.

4.4.3. Antimicrobial activity – Disk diffusion

The antimicrobial properties of ePCL scaffolds containing 2 wt% Arg were analyzed using disk diffusion assays against *S. aureus* and *E. coli*, as previously described. Figures 31 and 32 illustrate the experimental setup, with images (A) depicting plates with the mesh samples and images (B) showing plates after mesh removal to assess bacterial interaction. No inhibition zones were observed for any of the sample, indicating that Arg incorporation at 2 wt% does not confer intrinsic antibacterial activity. This suggests the Arg concentration was insufficient to produce a visible inhibitory effect. It should also be noted that the amount of Arg in the drop applied was equivalent by mass to the Arg present in the mesh containing 2 wt% Arg. These results underscore the need for MIC assays to determine the threshold Arg content required for bacterial inhibition, and to clarify if inactivity stems from low Arg levels or limited availability of reactive amino groups.

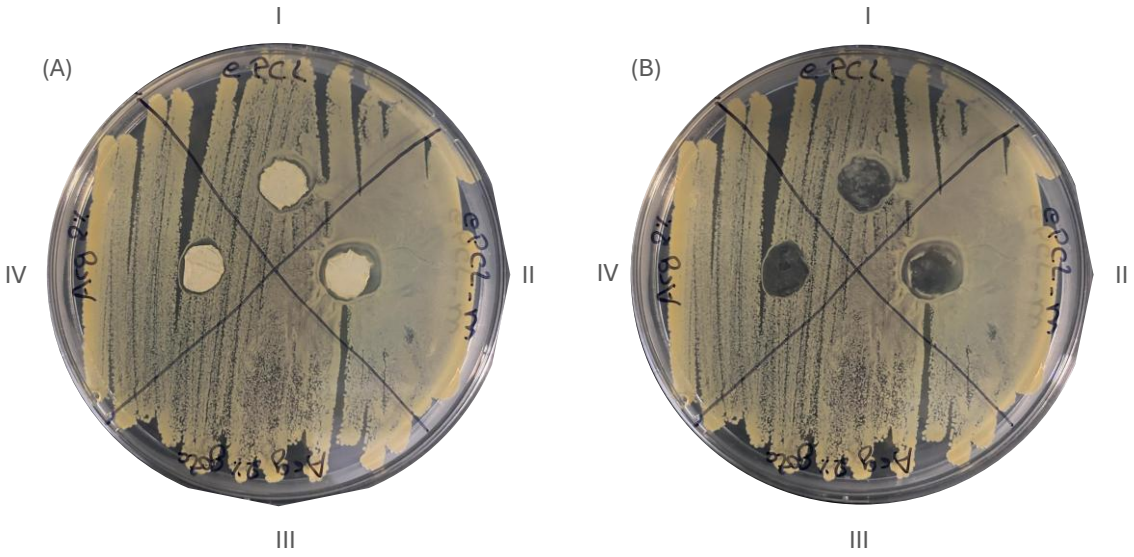

Figure 31 - Disk diffusion assay of (I) ePCL, (II) m_ePCL, (III) solution of Arg 2 wt%, (IV) ePCL with Arg 2 wt%, against *S. aureus*. (A) shows the plate with the mesh, and (B) shows the same plate without the mesh.

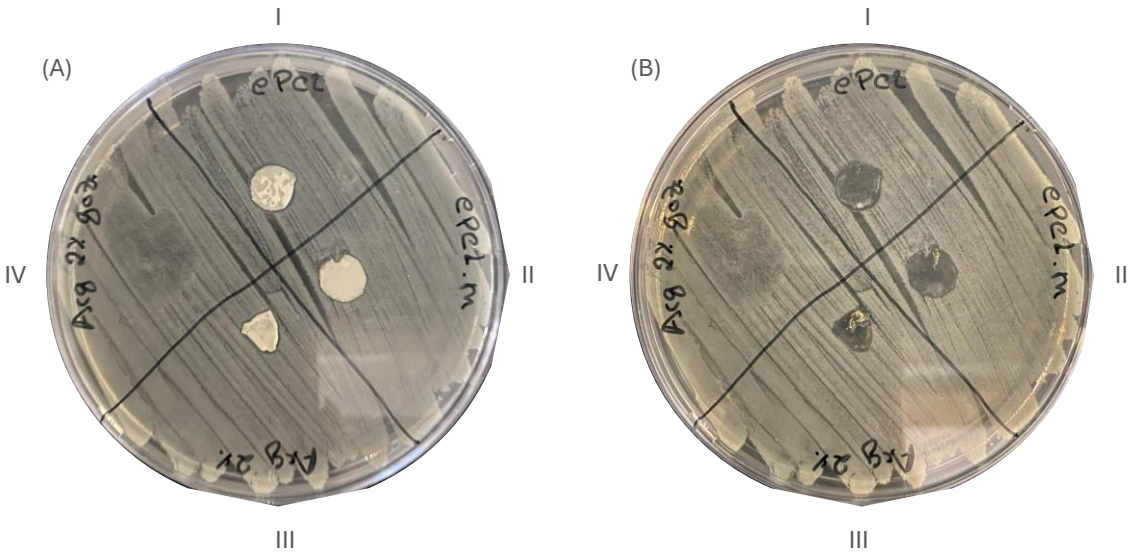

Figure 32 - Disk diffusion assay of (I) ePCL, (II) m_ePCL, (III) solution of Arg 2 wt%, (IV) ePCL with Arg 2 wt%, against *E. coli*. (A) shows the plate with the mesh, and (B) shows the same plate without the mesh.

4.4.4. *In vitro* studies

4.4.4.1. Cytotoxicity

The cytotoxicity evaluation focused on ePCL meshes with the highest Arg incorporation (2 wt%) as well as the relevant controls, since testing the maximum incorporation is sufficient to determine whether Arg addition introduces cytotoxicity. Assessment employed both IC and DC assays already described earlier, with results shown in Figure 33 (A)-(B), respectively.

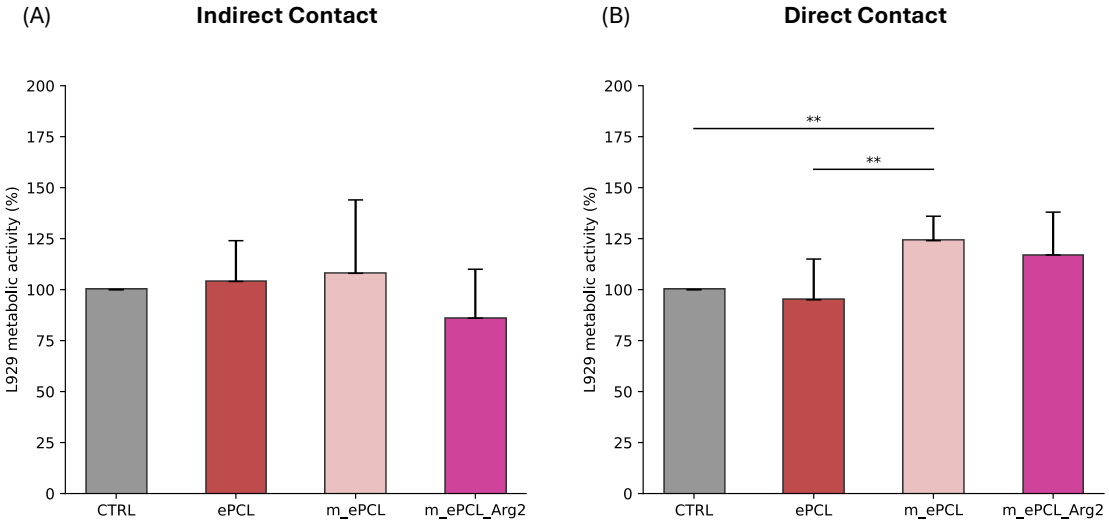

Figure 33 - Cytotoxicity assessment of ePCL with Arg at 2 wt% and controls. (A) IC and (B) DC with L929 cell line, for 24h. The positive control consisted of cells growing in the well without samples. Statistical significance for $p \leq 0.01$ (**).

Fibroblasts maintained metabolic activity across all tested conditions. In the IC assay (Figure 33 (A)), neither the control samples nor the biofunctionalized meshes with Arg 2 wt% showed cytotoxicity. Specifically, ePCL and modified ePCL controls recorded metabolic activities of 104 ± 20% and 108 ± 36%, respectively. Notably, the 2 wt% Arg-functionalized mesh also demonstrated non-cytotoxic behaviour, with 86 ± 24% metabolic activity. In the DC assay (Figure 33 (B)), all samples remained non-cytotoxic, with ePCL and modified ePCL showing 95 ± 20% and 124 ± 12% activity. Importantly, the Arg 2 wt% mesh exhibited a significant increase in metabolic activity (117 ± 21%), representing a ~17% enhancement compared to the positive control, highlighting a beneficial effect of Arg at this concentration.

4.4.4.2. Cell metabolic activity and proliferation

Cell proliferation on ePCL meshes modified with different concentrations of Arg, together with control samples, was assessed through metabolic activity measurements at 1, 3, 7, and 14 days post-seeding, as shown in Figure 34. Throughout the 14-day culture, the metabolic activity of L929 cells consistently increased, although it was relatively low at day 1, possibly reflecting initial cell attachment processes.

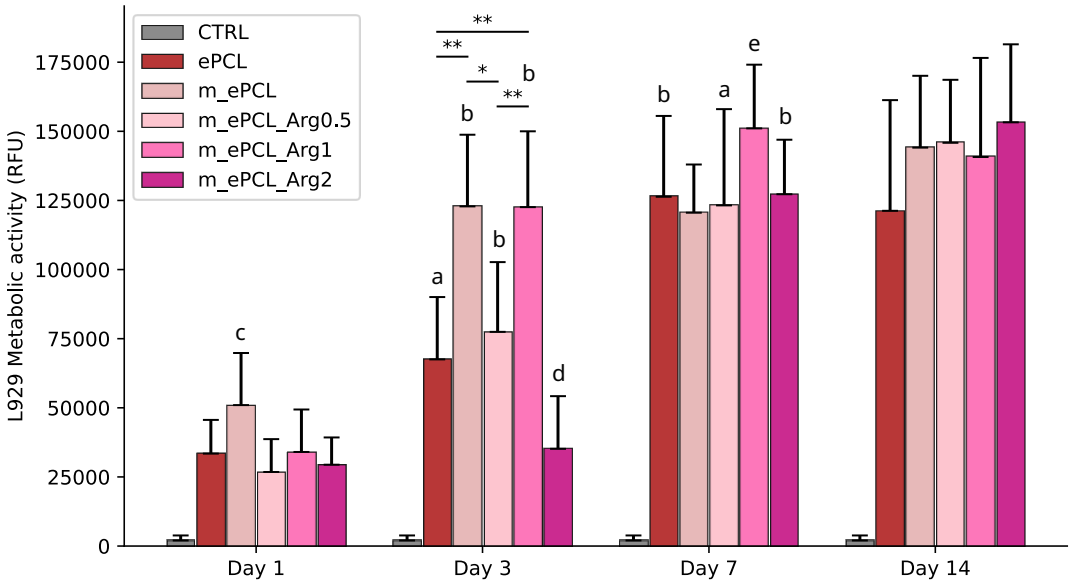

Figure 34 - Metabolic activity of L929 cells on ePCL with different concentrations of Arg and controls through 1, 3, 7 and 14 days after seeding, using an ePCL mesh without cells as a control for the experiment. Statistical significance for p ≤ 0.05 (*) and p ≤ 0.01 (**); Statistical significance with the previous time-point of p ≤ 0.05 (a); Statistical significance with the previous time-point of p ≤ 0.01 (b); Statistical significance with all other conditions (**) (c); Statistical significance with m_ePCL_Arg0.5/1 and m_ePCL (**) (d); Statistical significance with m_ePCL_Arg0.5/2 (*) and m_ePCL (**) (e).

Almost all samples showed statistical significance at day 3 compared to day 1 within their own condition, except for the 2 wt% Arg sample. At day 7, only the 1 wt% Arg and mPCL samples showed no significant differences compared to the previous time point. Additionally, none of the Arg-containing samples showed statistical significance at day 14 compared to day 7. These results may be explained by the fact that, up to day 7, cells tend to prefer samples with higher mechanical properties, whereas after that point, samples containing biological cues appear to be more attractive, leading to increased metabolic activity.

As reported earlier, the intrinsic hydrophobicity of ePCL impairs cell adhesion, which is evident from its lower metabolic activity compared to other conditions. On the other hand, the modified ePCL possesses polar functional groups that increase its hydrophilicity, thereby improving cell compatibility. This was reflected in higher metabolic activity relative to ePCL controls across all evaluated time points.

Arg is known to enhance cell proliferation and function by serving as a precursor for the synthesis of NO, which plays a critical role in cell signalling, wound healing, and tissue regeneration [80]. Across all time points, Arg incorporation resulted in enhanced cell metabolic activity compared to unmodified and modified ePCL controls. At day 3, the 1 wt% Arg condition exhibited the highest metabolic activity, significantly exceeding the other concentrations and the ePCL control group. Although Arg at 2 wt% exhibited significantly lower metabolic activity at day 3, the elevated response at early time points indicates that Arg biofunctionalization creates a more favourable microenvironment for cell adhesion, proliferation, and metabolic function. The tendency continues through days 7 and 14, with all Arg-functionalized samples exhibiting elevated activity, although differences between concentrations become less distinct as cell proliferation approaches a steady state.

Collectively, these findings highlight the beneficial effect of Arg incorporation at all concentrations into ePCL meshes, supporting improved biocompatibility and potential for TE applications.

4.4.4.3. Cell morphology and fibronectin deposition

SEM images of ePCL meshes biofunctionalized with different concentrations of Arg can be observed in Figure 35. On day 1, cells are sparsely distributed regardless of Arg concentration, reflecting initial attachment. By day 3, Arg functionalized samples (most notably on Arg 1 wt%) display increased cell density and it was possible to observe the development of an interconnected cellular network. Over longer culture periods (days 7 and 14), scaffolds containing Arg support robust cellular proliferation, forming a cell sheet under the sample. This evidence aligns with previously discussed metabolic and cytocompatibility assays, confirming that Arg modification improves cellular proliferation.

Additionally, the 2 wt% Arg sample, at day 14, presented a cell sheet integrated with the electrospun meshes, clearly demonstrating successful cell infiltration throughout the structure. Arg incorporation seems to substantially improve scaffold biocompatibility and support long-term cell proliferation, as visually tracked in SEM images and supported by prior quantitative data.

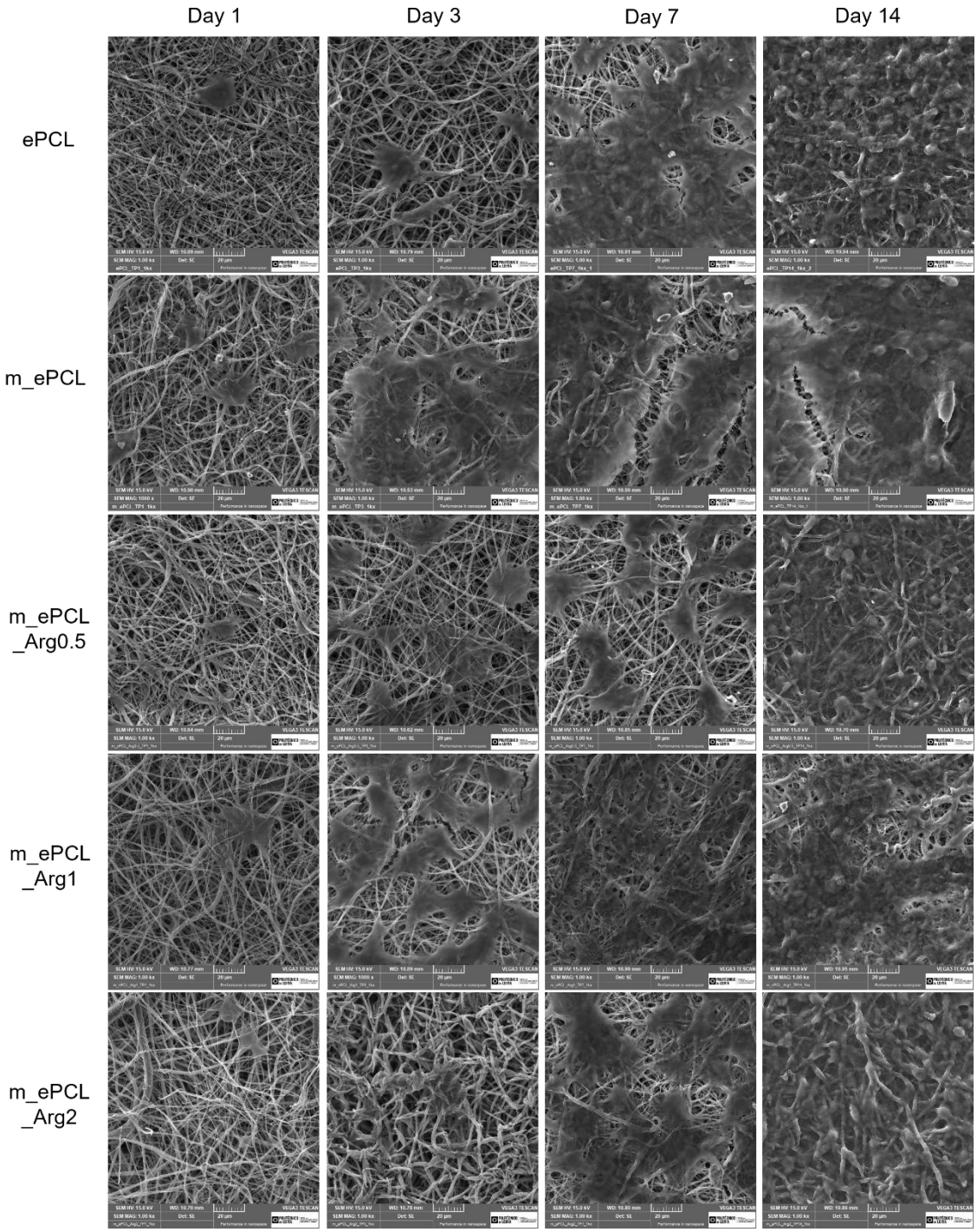

Figure 35 - Representative proliferation SEM images of L929 cells evaluated at 1, 3, 7 and 14 days of study after seeding in ePCL with different concentrations of Arg and controls. Scale bars correspond to 20 μm.

Figure 36 shows representative confocal microscopy images illustrating the evolution of L929 fibroblast proliferation and FN formation on ePCL meshes modified with different concentrations of Arg.

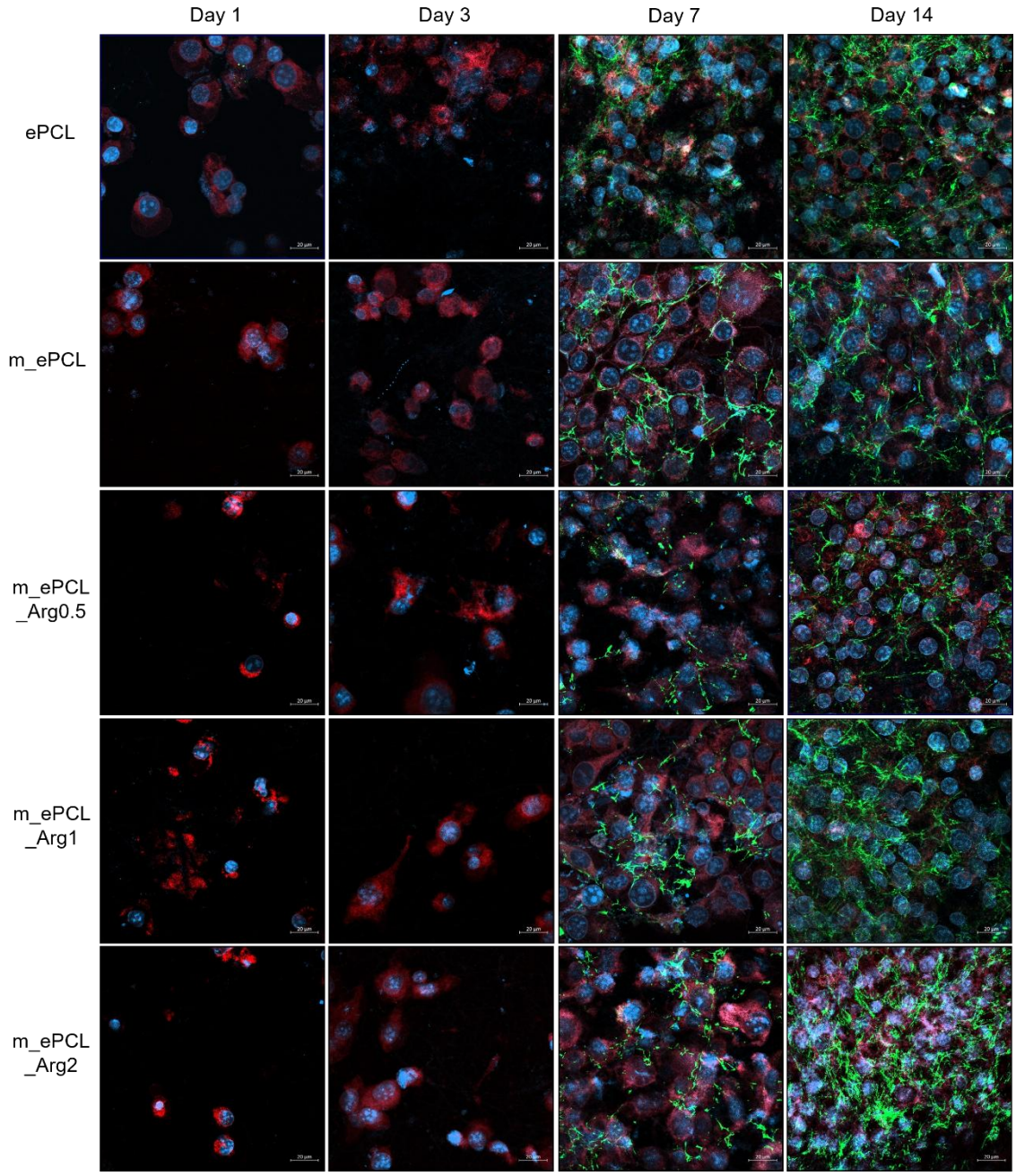

Figure 36 - Representative proliferation confocal images of L929 cells evaluated at 1, 3, 7 and 14 days of study after seeding in ePCL with different concentrations of Arg and controls (blue: nuclei; red: actin; green: FN). Scale bars correspond to 20 μm.

During the earliest stage (day 1), all scaffolds exhibit predominantly individual cells with blue-stained nuclei and slight cytoskeletal organization. By day 3, early cell spreading is observed across all samples, though mesh modifications with Arg do not yet show marked differences. From day 7 onward, Arg-enriched meshes exhibit substantially increased cell density, extensive actin cytoskeleton, and strong FN

deposition (mainly at day 14) compared to controls. These findings corroborate previous observations, indicating that Arg biofunctionalization significantly enhances cellular proliferation and facilitates extracellular matrix assembly. Confocal images illustrating individual stains for nuclei, actin, and FN can be found in Figures 37A - 37B and 45C - 47C of the appendix section.

For Arg, 1 wt% has been demonstrated to achieve the strongest biological effect, yielding the highest metabolic activity at early culture stages and maintaining superior cell response over time. However, it has been demonstrated that adding 2 wt% of Arg resulted in a reduction in both biofunctionalization efficiency and elongation when compared to lower loadings. Conversely, 0.5 wt% Arg has been shown to yield optimal attachment efficiency and slightly superior mechanical performance, although with less marked stimulation of cell proliferation on day 3. It can be concluded that 1 wt% Arg is the optimal concentration for maximizing cellular performance. However, 0.5 wt% is a more efficient alternative when material stability is prioritized.

Each biomolecule exhibited a unique optimal concentration at which point it demonstrated a distinct strength. It was demonstrated that a concentration of 0.1 wt% CS was the most effective in sustaining long-term proliferation, thereby maintaining the highest metabolic activity at later culture stages and supporting extended tissue integration. The results of the study demonstrated that Gel at 1 wt% exhibited mechanical properties that exhibited a stronger resemblance to those of native skin, whilst concurrently facilitating a uniform increase in metabolic activity throughout the culture period. Arg, at a concentration of 1 wt%, was found to generate the most hydrophilic surfaces, thereby enhancing the cell–material interface, yielding the highest metabolic activity overall. When considered as a whole, CS, Gel, and Arg each offer distinct advantages, including prolonged proliferation, early ECM deposition, and enhanced wettability. This collective effect demonstrates their potential for application in the design of structures for wound healing applications.

5. Conclusion and future work

This work demonstrated that through PCL electrospun meshes hydrolysis followed by EDC/NHS coupling, all biomolecules were immobilized without compromising scaffold porosity, which remained within the optimal range for TE applications. Moreover, the integration of these biomolecules onto the fiber surface, rather than within the fiber core, represents an advantage for enhancing cell–biomaterial interactions.

Surface wettability improved substantially, particularly with Arg, which rendered the meshes highly hydrophilic across all concentrations. CS at 0.5 wt% also produced marked hydrophilicity, while Gel displayed a concentration-dependent effect, with higher loads leading to increased hydrophobicity. Mechanical testing indicated moderate stiffening at intermediate Gel and Arg concentrations, although some loss of extensibility and tensile strength was observed compared with ePCL meshes. However, overall, all biofunctionalized samples exhibit mechanical properties within or close to the range of those of human skin.

Cytotoxicity assays confirmed that none of the formulations compromised cell viability, with all conditions being non-toxic. Proliferation assays revealed distinct cellular responses: Arg at 1 wt% promoted rapid initial cell growth, whereas Gel at 1 wt% and CS at 0.1 wt% maintained the highest proliferation levels over 14 days. These observations suggest that biomolecule type and concentration modulate cellular behaviour through different stimulatory mechanisms.

Future work should focus on quantifying biomolecule attachment efficiency for CS and Gel, assessing coating stability under physiologically relevant conditions, and extending biological analyses beyond viability to include extracellular matrix deposition quantification, inflammatory responses with hemocompatibility assays, and angiogenic markers such as NO release for Arg potential studies [80]. Studies under dynamic culture conditions, followed by *in vivo* wound-healing models, will be essential to validate these findings in clinically relevant environments. Furthermore, exploring combined biomolecules may enable synergistic effects.

Overall, this thesis establishes that CS, Gel, and Arg biofunctionalization can substantially improve the biological performance of ePCL wound dressings without compromising their fundamental physical properties CS at 0.1 wt%, Gel at 1 wt% and Arg at 1 wt% emerge as particularly promising conditions, offering a strong basis for the development of next-generation bioactive wound dressings.

References

[1] Sindhi K, Pingili RB, Beldar V, Bhattacharya S, Rahaman J, Mukherjee D. The role of biomaterials-based scaffolds in advancing skin tissue construct. J Tissue Viability 2025;34:100858. https://doi.org/10.1016/j.jtv.2025.100858.

[2] Blair NF, Frith TJR, Barbaric I. Regenerative Medicine: Advances from Developmental to Degenerative Diseases, 2017, p. 225–39. https://doi.org/10.1007/978-3-319-60733-7_12.

[3] Ongarora BG. Recent technological advances in the management of chronic wounds: A literature review. Health Sci Rep 2022;5. https://doi.org/10.1002/hsr2.641.

[4] Coleman S, Nelson EA, Vowden P, Vowden K, Adderley U, Sunderland L, et al. Development of a generic wound care assessment minimum data set. J Tissue Viability 2017;26:226–40. https://doi.org/10.1016/j.jtv.2017.09.007.

[5] Cho SK, Mattke S, Gordon H, Sheridan M, Ennis W. Development of a Model to Predict Healing of Chronic Wounds Within 12 Weeks. Adv Wound Care (New Rochelle) 2020;9:516–24. https://doi.org/10.1089/wound.2019.1091.

[6] Markiewicz-Gospodarek A, Kozioł M, Tobiasz M, Baj J, Radzikowska-Büchner E, Przekora A. Burn Wound Healing: Clinical Complications, Medical Care, Treatment, and Dressing Types: The Current State of Knowledge for Clinical Practice. Int J Environ Res Public Health 2022;19:1338. https://doi.org/10.3390/ijerph19031338.

[7] Wasiak J, Cleland H, Campbell F. Dressings for superficial and partial thickness burns. In: Wasiak J, editor. Cochrane Database of Systematic Reviews, Chichester, UK: John Wiley & Sons, Ltd; 2008. https://doi.org/10.1002/14651858.CD002106.pub3.

[8] Dias JR, Baptista-Silva S, Oliveira CMT de, Sousa A, Oliveira AL, Bártolo PJ, et al. In situ crosslinked electrospun gelatin nanofibers for skin regeneration. Eur Polym J 2017;95:161–73. https://doi.org/10.1016/j.eurpolymj.2017.08.015.

[9] Dong Y, Jaleh B, Ashrafi G, Kashfi M, Rhee KY. Mechanical properties of the hybrids of natural (alginate, collagen, chitin, cellulose, gelatin, chitosan, silk, and keratin) and synthetic electrospun nanofibers: A review. Int J Biol Macromol 2025;312:143742. https://doi.org/10.1016/j.ijbiomac.2025.143742.

[10] Kishan AP, Nezarati RM, Radzicki CM, Renfro AL, Robinson JL, Whitely ME, et al. In situ crosslinking of electrospun gelatin for improved fiber morphology

retention and tunable degradation. J Mater Chem B 2015;3:7930–8. https://doi.org/10.1039/C5TB00937E.

[11] Meli L, Miao J, Dordick JS, Linhardt RJ. Electrospinning from room temperature ionic liquids for biopolymer fiber formation. Green Chemistry 2010;12:1883. https://doi.org/10.1039/c0gc00283f.

[12] Feng P, Luo Y, Ke C, Qiu H, Wang W, Zhu Y, et al. Chitosan-Based Functional Materials for Skin Wound Repair: Mechanisms and Applications. Front Bioeng Biotechnol 2021;9. https://doi.org/10.3389/fbioe.2021.650598.

[13] Ito A, Mase A, Takizawa Y, Shinkai M, Honda H, Hata K-I, et al. Transglutaminase-mediated gelatin matrices incorporating cell adhesion factors as a biomaterial for tissue engineering. J Biosci Bioeng 2003;95:196–9. https://doi.org/10.1016/S1389-1723(03)80129-9.

[14] Bikiaris RE, Matschek NI, Koumentakou I, Niti A, Kyzas GZ. Synergistic effects of arginine and tannic acid on chitosan matrices: An approach for hemostatic sponge development. Int J Biol Macromol 2025;318:145105. https://doi.org/10.1016/j.ijbiomac.2025.145105.

[15] Dias JR, Granja PL, Bártolo PJ. Advances in electrospun skin substitutes. Prog Mater Sci 2016;84:314–34. https://doi.org/10.1016/j.pmatsci.2016.09.006.

[16] Structure and Function of Skin. Toxicology of the Skin, CRC Press; 2010, p. 15–32. https://doi.org/10.3109/9781420079180-3.

[17] &NA; Anatomy and Physiology of the Skin. J Dermatol Nurses Assoc 2011;3:214–5. https://doi.org/10.1097/JDN.0b013e31822bdc94.

[18] de Szalay S, Wertz PW. Protective Barriers Provided by the Epidermis. Int J Mol Sci 2023;24:3145. https://doi.org/10.3390/ijms24043145.

[19] Kolarsick PAJ, Kolarsick MA, Goodwin C. Anatomy and Physiology of the Skin. J Dermatol Nurses Assoc 2011;3:203–13. https://doi.org/10.1097/JDN.0b013e3182274a98.

[20] Lewis-Jones S, Murphy R, editors. Structure and function of the skin. Paediatric Dermatology, Oxford University Press; 2020, p. 3–14. https://doi.org/10.1093/med/9780198821304.003.0001.

[21] Valle M, Zamorani MP. Skin and Subcutaneous Tissue. Ultrasound of the Musculoskeletal System, Berlin, Heidelberg: Springer Berlin Heidelberg; n.d., p. 19–43. https://doi.org/10.1007/978-3-540-28163-4_2.

[22] Arribas-López E, Zand N, Ojo O, Snowden MJ, Kochhar T. The Effect of Amino Acids on Wound Healing: A Systematic Review and Meta-Analysis on Arginine and Glutamine. Nutrients 2021;13:2498. https://doi.org/10.3390/nu13082498.

[23] Reinke JM, Sorg H. Wound Repair and Regeneration. European Surgical Research 2012;49:35–43. https://doi.org/10.1159/000339613.

[24] Jonidi Shariatzadeh F, Currie S, Logsetty S, Spiwak R, Liu S. Enhancing wound healing and minimizing scarring: A comprehensive review of nanofiber technology in wound dressings. Prog Mater Sci 2025;147:101350. https://doi.org/10.1016/j.pmatsci.2024.101350.

[25] Gounden V, Singh M. Hydrogels and Wound Healing: Current and Future Prospects. Gels 2024;10:43. https://doi.org/10.3390/gels10010043.

[26] Peña OA, Martin P. Cellular and molecular mechanisms of skin wound healing. Nat Rev Mol Cell Biol 2024;25:599–616. https://doi.org/10.1038/s41580-024-00715-1.

[27] Spielman AF, Griffin MF, Parker J, Cotterell AC, Wan DC, Longaker MT. Beyond the Scar: A Basic Science Review of Wound Remodeling. Adv Wound Care (New Rochelle) 2023;12:57–67. https://doi.org/10.1089/wound.2022.0049.

[28] Sarrazy V, Billet F, Micallef L, Coulomb B, Desmoulière A. Mechanisms of pathological scarring: Role of myofibroblasts and current developments. Wound Repair and Regeneration 2011;19. https://doi.org/10.1111/j.1524-475X.2011.00708.x.

[29] WHO - World Health Organization - Burns 2023.

[30] Roy S, Mukherjee P, Kundu S, Majumder D, Raychaudhuri V, Choudhury L. Microbial infections in burn patients. Acute and Critical Care 2024;39:214–25. https://doi.org/10.4266/acc.2023.01571.

[31] Opriessnig E, Luze H, Smolle C, Draschl A, Zrim R, Giretzlehner M, et al. Epidemiology of burn injury and the ideal dressing in global burn care – Regional differences explored. Burns 2023;49:1–14. https://doi.org/10.1016/j.burns.2022.06.018.

[32] Abraham J, Whiteman B, Coad J, Kneafsey R. Development and implementation of non-medical practitioners in acute care. British Journal of Nursing 2016;25:1129–34. https://doi.org/10.12968/bjon.2016.25.20.1129.

[33] Deng X, Gould M, Ali MA. A review of current advancements for wound healing: Biomaterial applications and medical devices. J Biomed Mater Res B Appl Biomater 2022;110:2542–73. https://doi.org/10.1002/jbm.b.35086.

[34] Freedman BR, Hwang C, Talbot S, Hibler B, Matoori S, Mooney DJ. Breakthrough treatments for accelerated wound healing. Sci Adv 2023;9. https://doi.org/10.1126/sciadv.ade7007.

[35] Dahan A, Hoffman A. Rationalizing the selection of oral lipid based drug delivery systems by an in vitro dynamic lipolysis model for improved oral bioavailability of poorly water soluble drugs. Journal of Controlled Release 2008;129:1–10. https://doi.org/10.1016/j.jconrel.2008.03.021.

[36] Vig K, Chaudhari A, Tripathi S, Dixit S, Sahu R, Pillai S, et al. Advances in Skin Regeneration Using Tissue Engineering. Int J Mol Sci 2017;18:789. https://doi.org/10.3390/ijms18040789.

[37] Negut I, Dorcioman G, Grumezescu V. Scaffolds for Wound Healing Applications. Polymers (Basel) 2020;12:2010. https://doi.org/10.3390/polym12092010.

[38] Colazo JM, Evans BC, Farinas AF, Al-Kassis S, Duvall CL, Thayer WP. Applied Bioengineering in Tissue Reconstruction, Replacement, and Regeneration. Tissue Eng Part B Rev 2019;25:259–90. https://doi.org/10.1089/ten.teb.2018.0325.

[39] Dimatteo R, Darling NJ, Segura T. In situ forming injectable hydrogels for drug delivery and wound repair. Adv Drug Deliv Rev 2018;127:167–84. https://doi.org/10.1016/j.addr.2018.03.007.

[40] Binder KW, Zhao W, Aboushwareb T, Dice D, Atala A, Yoo JJ. In situ bioprinting of the skin for burns. J Am Coll Surg 2010;211:S76. https://doi.org/10.1016/j.jamcollsurg.2010.06.198.

[41] Leitner J, Sedmidubský D, Lojka M, Jankovský O. The Effect of Nanosizing on the Oxidation of Partially Oxidized Copper Nanoparticles. Materials 2020;13:2878. https://doi.org/10.3390/ma13122878.

[42] Markhoff J, Krogull M, Schulze C, Rotsch C, Hunger S, Bader R. Biocompatibility and Inflammatory Potential of Titanium Alloys Cultivated with Human Osteoblasts, Fibroblasts and Macrophages. Materials 2017;10:52. https://doi.org/10.3390/ma10010052.

[43] Adel IM, ElMeligy MF, Elkasabgy NA. Conventional and Recent Trends of Scaffolds Fabrication: A Superior Mode for Tissue Engineering. Pharmaceutics 2022;14:306. https://doi.org/10.3390/pharmaceutics14020306.

[44] Capuana E, Lopresti F, Carfì Pavia F, Brucato V, La Carrubba V. Solution-Based Processing for Scaffold Fabrication in Tissue Engineering Applications: A Brief Review. Polymers (Basel) 2021;13:2041. https://doi.org/10.3390/polym13132041.

[45] Lee B Il, Chung YJ, Park CB. Photosensitizing materials and platforms for light-triggered modulation of Alzheimer's β-amyloid self-assembly. Biomaterials 2019;190–191:121–32. https://doi.org/10.1016/j.biomaterials.2018.10.043.

[46] Walmsley AM, Doran PM. Foreign protein production using plant cells: Opportunities and challenges. Biotechnol Adv 2012;30:385–6. https://doi.org/10.1016/j.biotechadv.2011.08.002.

[47] Planz V, Seif S, Atchison JS, Vukosavljevic B, Sparenberg L, Kroner E, et al. Three-dimensional hierarchical cultivation of human skin cells on bio-adaptive hybrid fibers. Integrative Biology 2016;8:775–84. https://doi.org/10.1039/C6IB00080K.

[48] Dias JR, Sousa A, Augusto A, Bártolo PJ, Granja PL. Electrospun Polycaprolactone (PCL) Degradation: An In Vitro and In Vivo Study. Polymers (Basel) 2022;14:3397. https://doi.org/10.3390/polym14163397.

[49] Cui C, Sun S, Wu S, Chen S, Ma J, Zhou F. Electrospun chitosan nanofibers for wound healing application. Engineered Regeneration 2021;2:82–90. https://doi.org/10.1016/j.engreg.2021.08.001.

[50] Syed MH, Khan MMR, Zahari MAKM, Beg MDH, Abdullah N. Current issues and potential solutions for the electrospinning of major polysaccharides and proteins: A review. Int J Biol Macromol 2023;253:126735. https://doi.org/10.1016/j.ijbiomac.2023.126735.

[51] Vlachou M, Siamidi A, Kyriakou S. Electrospinning and Drug Delivery. Electrospinning and Electrospraying - Techniques and Applications, IntechOpen; 2019. https://doi.org/10.5772/intechopen.86181.

[52] Henriques C, Vidinha R, Botequim D, Borges JP, Silva JAMC. A Systematic Study of Solution and Processing Parameters on Nanofiber Morphology Using a New Electrospinning Apparatus. J Nanosci Nanotechnol 2009;9:3535–45. https://doi.org/10.1166/jnn.2009.NS27.

[53] Pelipenko J, Kristl J, Janković B, Baumgartner S, Kocbek P. The impact of relative humidity during electrospinning on the morphology and mechanical properties of nanofibers. Int J Pharm 2013;456:125–34. https://doi.org/10.1016/j.ijpharm.2013.07.078.

[54] Nezarati RM, Eifert MB, Cosgriff-Hernandez E. Effects of Humidity and Solution Viscosity on Electrospun Fiber Morphology. Tissue Eng Part C Methods 2013;19:810–9. https://doi.org/10.1089/ten.tec.2012.0671.

[55] Tucker N, Stanger JJ, Staiger MP, Razzaq H, Hofman K. The History of the Science and Technology of Electrospinning from 1600 to 1995. J Eng Fiber Fabr 2012;7. https://doi.org/10.1177/155892501200702S10.

[56] Xue J, Wu T, Dai Y, Xia Y. Electrospinning and Electrospun Nanofibers: Methods, Materials, and Applications. Chem Rev 2019;119:5298–415. https://doi.org/10.1021/acs.chemrev.8b00593.

[57] Zhang K, Fang X, Zhu J, Yang R, Wang Y, Zhao W, et al. Effective Reconstruction of Functional Urethra Promoted With ICG-001 Delivery Using Core-Shell Collagen/Poly(Llactide-co-caprolactone) [P(LLA-CL)] Nanoyarn-Based Scaffold: A Study in Dog Model. Front Bioeng Biotechnol 2020;8. https://doi.org/10.3389/fbioe.2020.00774.

[58] Nguyen HH, Kim M. An Overview of Techniques in Enzyme Immobilization. Applied Science and Convergence Technology 2017;26:157–63. https://doi.org/10.5757/ASCT.2017.26.6.157.

[59] Smith S, Goodge K, Delaney M, Struzyk A, Tansey N, Frey M. A Comprehensive Review of the Covalent Immobilization of Biomolecules onto Electrospun Nanofibers. Nanomaterials 2020;10:2142. https://doi.org/10.3390/nano10112142.

[60] Niemczyk-Soczynska B, Gradys A, Sajkiewicz P. Hydrophilic Surface Functionalization of Electrospun Nanofibrous Scaffolds in Tissue Engineering. Polymers (Basel) 2020;12:2636. https://doi.org/10.3390/polym12112636.

[61] Cui D, Li M, Zhang P, Rao F, Huang W, Wang C, et al. Polydopamine-Coated Polycaprolactone Electrospun Nanofiber Membrane Loaded with Thrombin for Wound Hemostasis. Polymers (Basel) 2023;15:3122. https://doi.org/10.3390/polym15143122.

[62] Zuppolini S, Cruz-Maya I, Guarino V, Borriello A. Optimization of Polydopamine Coatings onto Poly–ε–Caprolactone Electrospun Fibers for the Fabrication of Bio-Electroconductive Interfaces. J Funct Biomater 2020;11:19. https://doi.org/10.3390/jfb11010019.

[63] Liu X, Zhou C, Xie Q, Xia L, Liu L, Bao W, et al. Recent advances in layer-by-layer assembly scaffolds for co-delivery of bioactive molecules for bone regeneration: an updated review. J Transl Med 2024;22:1001. https://doi.org/10.1186/s12967-024-05809-0.

[64] Yao T, Chen H, Wang R, Rivero R, Wang F, Kessels L, et al. Thiol-ene conjugation of a VEGF peptide to electrospun scaffolds for potential applications in angiogenesis. Bioact Mater 2023;20:306–17. https://doi.org/10.1016/j.bioactmat.2022.05.029.

[65] Grim JC, Marozas IA, Anseth KS. Thiol-ene and photo-cleavage chemistry for controlled presentation of biomolecules in hydrogels. Journal of Controlled Release 2015;219:95–106. https://doi.org/10.1016/j.jconrel.2015.08.040.

[66] Xu J, Liu Y, Hsu S. Hydrogels Based on Schiff Base Linkages for Biomedical Applications. Molecules 2019;24:3005. https://doi.org/10.3390/molecules24163005.

[67] Shi J, Lian H, Huang Y, Zhao D, Wang H, Wang C, et al. *In vitro* genotoxicity evaluation and metabolic study of residual glutaraldehyde in animal-derived biomaterials. Regen Biomater 2020;7:619–25. https://doi.org/10.1093/rb/rbaa041.

[68] Dulnik J, Jeznach O, Sajkiewicz P. A Comparative Study of Three Approaches to Fibre's Surface Functionalization. J Funct Biomater 2022;13:272. https://doi.org/10.3390/jfb13040272.

[69] Palazon F, Montenegro Benavides C, Léonard D, Souteyrand É, Chevolot Y, Cloarec J-P. Carbodiimide/NHS Derivatization of COOH-Terminated SAMs:

Activation or Byproduct Formation? Langmuir 2014;30:4545–50. https://doi.org/10.1021/la5004269.

[70] Yaseri R, Fadaie M, Mirzaei E, Samadian H, Ebrahiminezhad A. Surface modification of polycaprolactone nanofibers through hydrolysis and aminolysis: a comparative study on structural characteristics, mechanical properties, and cellular performance. Sci Rep 2023;13:9434. https://doi.org/10.1038/s41598-023-36563-w.

[71] Dupuy S, Salvador J, Morille M, Noël D, Belamie E. Control and interplay of scaffold–biomolecule interactions applied to cartilage tissue engineering. Biomater Sci 2025;13:1871–900. https://doi.org/10.1039/D5BM00049A.

[72] Lv B, Wu J, Xiong Y, Xie X, Lin Z, Mi B, et al. Functionalized multidimensional biomaterials for bone microenvironment engineering applications: Focus on osteoimmunomodulation. Front Bioeng Biotechnol 2022;10. https://doi.org/10.3389/fbioe.2022.1023231.

[73] Chan BP, Leong KW. Scaffolding in tissue engineering: general approaches and tissue-specific considerations. European Spine Journal 2008;17:467–79. https://doi.org/10.1007/s00586-008-0745-3.

[74] Rajinikanth B S, Rajkumar DSR, K K, Vijayaragavan V. Chitosan-Based Biomaterial in Wound Healing: A Review. Cureus 2024. https://doi.org/10.7759/cureus.55193.

[75] Pasini C, Re F, Trenta F, Russo D, Sartore L. Gelatin-Based Scaffolds with Carrageenan and Chitosan for Soft Tissue Regeneration. Gels 2024;10:426. https://doi.org/10.3390/gels10070426.

[76] Mansur AAP, Carvalho SM, Brito RM de M, Capanema NS V., Duval I de B, Cardozo ME, et al. Arginine-Biofunctionalized Ternary Hydrogel Scaffolds of Carboxymethyl Cellulose–Chitosan–Polyvinyl Alcohol to Deliver Cell Therapy for Wound Healing. Gels 2024;10:679. https://doi.org/10.3390/gels10110679.

[77] Biswal T. Biopolymers for tissue engineering applications: A review. Mater Today Proc 2021;41:397–402. https://doi.org/10.1016/j.matpr.2020.09.628.

[78] Qiao C, Ma X, Zhang J, Yao J. Molecular interactions in gelatin/chitosan composite films. Food Chem 2017;235:45–50. https://doi.org/10.1016/j.foodchem.2017.05.045.

[79] Alexander JW, Supp DM. Role of Arginine and Omega-3 Fatty Acids in Wound Healing and Infection. Adv Wound Care (New Rochelle) 2014;3:682–90. https://doi.org/10.1089/wound.2013.0469.

[80] Jiang H, Xu Q, Wang X, Shi L, Yang X, Sun J, et al. Preparation of Antibacterial, Arginine-Modified Ag Nanoclusters in the Hydrogel Used for Promoting Diabetic, Infected Wound Healing. ACS Omega 2023;8:12653–63. https://doi.org/10.1021/acsomega.2c07266.

[81] Holecek M, Sispera L. Effects of Arginine Supplementation on Amino Acid Profiles in Blood and Tissues in Fed and Overnight-Fasted Rats. Nutrients 2016;8:206. https://doi.org/10.3390/nu8040206.

[82] ASTM, Standard test methods for water vapor transmission of materials E96/ E96M-10 n.d.

[83] Dias J, Bártolo P. Morphological Characteristics of Electrospun PCL Meshes – The Influence of Solvent Type and Concentration. Procedia CIRP 2013;5:216–21. https://doi.org/10.1016/j.procir.2013.01.043.

[84] Wang C, Niu X, Bao S, Shen W, Jiang C. Distribution Patterns and Antibiotic Resistance Profiles of Bacterial Pathogens Among Patients with Wound Infections in the Jiaxing Region from 2021 to 2023. Infect Drug Resist 2024;Volume 17:2883–96. https://doi.org/10.2147/IDR.S470401.

[85] Karakecili AG, Demirtas TT, Satriano C, Gümüsderelioglu M, Marletta G. Evaluation of L929 fibroblast attachment and proliferation on Arg-Gly-Asp-Ser (RGDS)-immobilized chitosan in serum-containing/serum-free cultures. J Biosci Bioeng 2007;104:69–77. https://doi.org/10.1263/jbb.104.69.

[86] Elzein T, Nasser-Eddine M, Delaite C, Bistac S, Dumas P. FTIR study of polycaprolactone chain organization at interfaces. J Colloid Interface Sci 2004;273:381–7. https://doi.org/10.1016/j.jcis.2004.02.001.

[87] Ali S, Khatri Z, Oh KW, Kim I-S, Kim SH. Preparation and characterization of hybrid polycaprolactone/cellulose ultrafine fibers via electrospinning. Macromol Res 2014;22:562–8. https://doi.org/10.1007/s13233-014-2078-x.

[88] Valente JFA, Carreira TS, Dias JR, Sousa F, Alves N. Arginine-Modified 3D-Printed Chromatographic Supports. Pharmaceutics 2022;14:2266. https://doi.org/10.3390/pharmaceutics14112266.

[89] Mukasheva F, Adilova L, Dyussenbinov A, Yernaimanova B, Abilev M, Akilbekova D. Optimizing scaffold pore size for tissue engineering: insights across various tissue types. Front Bioeng Biotechnol 2024;12. https://doi.org/10.3389/fbioe.2024.1444986.

[90] Ferreira CAM, Januário AP, Félix R, Alves N, Lemos MFL, Dias JR. Multifunctional Gelatin/Chitosan Electrospun Wound Dressing Dopped with Undaria pinnatifida Phlorotannin-Enriched Extract for Skin Regeneration. Pharmaceutics 2021;13:2152. https://doi.org/10.3390/pharmaceutics13122152.

[91] Almeida A, Araújo M, Novoa-Carballal R, Andrade F, Gonçalves H, Reis RL, et al. Novel amphiphilic chitosan micelles as carriers for hydrophobic anticancer drugs. Materials Science and Engineering: C 2020;112:110920. https://doi.org/10.1016/j.msec.2020.110920.

[92] Özdabak Sert AB, Bittrich E, Uhlmann P, Kok FN, Kılıç A. Monitoring Cell Adhesion on Polycaprolactone–Chitosan Films with Varying Blend Ratios by

Quartz Crystal Microbalance with Dissipation. ACS Omega 2023;8:17017–27. https://doi.org/10.1021/acsomega.3c01055.

[93] S. Dassanayake R, Acharya S, Abidi N. Biopolymer-Based Materials from Polysaccharides: Properties, Processing, Characterization and Sorption Applications. Advanced Sorption Process Applications, IntechOpen; 2019. https://doi.org/10.5772/intechopen.80898.

[94] Stani C, Vaccari L, Mitri E, Birarda G. FTIR investigation of the secondary structure of type I collagen: New insight into the amide III band. Spectrochim Acta A Mol Biomol Spectrosc 2020;229:118006. https://doi.org/10.1016/j.saa.2019.118006.

[95] Kievit FM, Cooper A, Jana S, Leung MC, Wang K, Edmondson D, et al. Aligned Chitosan-Polycaprolactone Polyblend Nanofibers Promote the Migration of Glioblastoma Cells. Adv Healthc Mater 2013;2:1651–9. https://doi.org/10.1002/adhm.201300092.

[96] Xu R, Xia H, He W, Li Z, Zhao J, Liu B, et al. Controlled water vapor transmission rate promotes wound-healing via wound re-epithelialization and contraction enhancement. Sci Rep 2016;6:24596. https://doi.org/10.1038/srep24596.

[97] Chen H-W, Lin M-F. Characterization, Biocompatibility, and Optimization of Electrospun SF/PCL/CS Composite Nanofibers. Polymers (Basel) 2020;12:1439. https://doi.org/10.3390/polym12071439.

[98] Mosallanezhad P, Nazockdast H, Ahmadi Z, Rostami A. Fabrication and characterization of polycaprolactone/chitosan nanofibers containing antibacterial agents of curcumin and ZnO nanoparticles for use as wound dressing. Front Bioeng Biotechnol 2022;10. https://doi.org/10.3389/fbioe.2022.1027351.

[99] Wang W, Caetano G, Ambler W, Blaker J, Frade M, Mandal P, et al. Enhancing the Hydrophilicity and Cell Attachment of 3D Printed PCL/Graphene Scaffolds for Bone Tissue Engineering. Materials 2016;9:992. https://doi.org/10.3390/ma9120992.

[100] Chen L, Liu K, Ye J-R, Shen Q. Controlled formation of surface hydrophilicity enhanced chitosan film by layer-by-layer electro-assembly. Materials Science and Engineering: C 2015;56:518–21. https://doi.org/10.1016/j.msec.2015.07.021.

[101] Gu J, Jing Xia, Fan X, Chen P, Zhou X, Huang J, et al. Electrospun chitosan-graft-poly (ε-caprolactone)/poly (ε-caprolactone) nanofibrous scaffolds for retinal tissue engineering. Int J Nanomedicine 2011:453. https://doi.org/10.2147/IJN.S17057.

[102] Jansen LH, Rottier PB. Some Mechanical Properties of Human Abdominal Skin Measured on Excised Strips. Dermatology 1958;117:65–83. https://doi.org/10.1159/000255569.

[103] Jacquemoud C, Bruyere-Garnier K, Coret M. Methodology to determine failure characteristics of planar soft tissues using a dynamic tensile test. J Biomech 2007;40:468–75. https://doi.org/10.1016/j.jbiomech.2005.12.010.

[104] Pan J, Liu N, Sun H, Xu F. Preparation and Characterization of Electrospun PLCL/Poloxamer Nanofibers and Dextran/Gelatin Hydrogels for Skin Tissue Engineering. PLoS One 2014;9:e112885. https://doi.org/10.1371/journal.pone.0112885.

[105] Pawlaczyk M, Lelonkiewicz M, Wieczorowski M. Age-dependent biomechanical properties of the skin. Advances in Dermatology and Allergology 2013;5:302–6. https://doi.org/10.5114/pdia.2013.38359.

[106] Yilmaz Atay H. Antibacterial Activity of Chitosan-Based Systems. Functional Chitosan, Singapore: Springer Singapore; 2019, p. 457–89. https://doi.org/10.1007/978-981-15-0263-7_15.

[107] Ardean C, Davidescu CM, Nemeş NS, Negrea A, Ciopec M, Duteanu N, et al. Factors Influencing the Antibacterial Activity of Chitosan and Chitosan Modified by Functionalization. Int J Mol Sci 2021;22:7449. https://doi.org/10.3390/ijms22147449.

[108] Rodríguez-Vázquez M, Vega-Ruiz B, Ramos-Zúñiga R, Saldaña-Koppel DA, Quiñones-Olvera LF. Chitosan and Its Potential Use as a Scaffold for Tissue Engineering in Regenerative Medicine. Biomed Res Int 2015;2015:1–15. https://doi.org/10.1155/2015/821279.

[109] Dias JR, Baptista-Silva S, Sousa A, Oliveira AL, Bártolo PJ, Granja PL. Biomechanical performance of hybrid electrospun structures for skin regeneration. Materials Science and Engineering: C 2018;93:816–27. https://doi.org/10.1016/j.msec.2018.08.050.

[110] Hielscher A, Ellis K, Qiu C, Porterfield J, Gerecht S. Fibronectin Deposition Participates in Extracellular Matrix Assembly and Vascular Morphogenesis. PLoS One 2016;11:e0147600. https://doi.org/10.1371/journal.pone.0147600.

[111] Gomes SR, Rodrigues G, Martins GG, Roberto MA, Mafra M, Henriques CMR, et al. In vitro and in vivo evaluation of electrospun nanofibers of PCL, chitosan and gelatin: A comparative study. Materials Science and Engineering: C 2015;46:348–58. https://doi.org/10.1016/j.msec.2014.10.051.

[112] Guerreiro SFC, Leal F, Dias AG, Granja PL, Dias JR. Polycaprolactone (PCL)-Gelatin Electrospun Meshes for Accelerated Gastric Wound Healing. Colloids Surf B Biointerfaces 2025;250:114572. https://doi.org/10.1016/j.colsurfb.2025.114572.

[113] Nashchekina Y, Chabina A, Nashchekin A, Mikhailova N. Polycaprolactone Films Modified by L-Arginine for Mesenchymal Stem Cell Cultivation. Polymers (Basel) 2020;12:1042. https://doi.org/10.3390/polym12051042.

Appendices

Appendix A

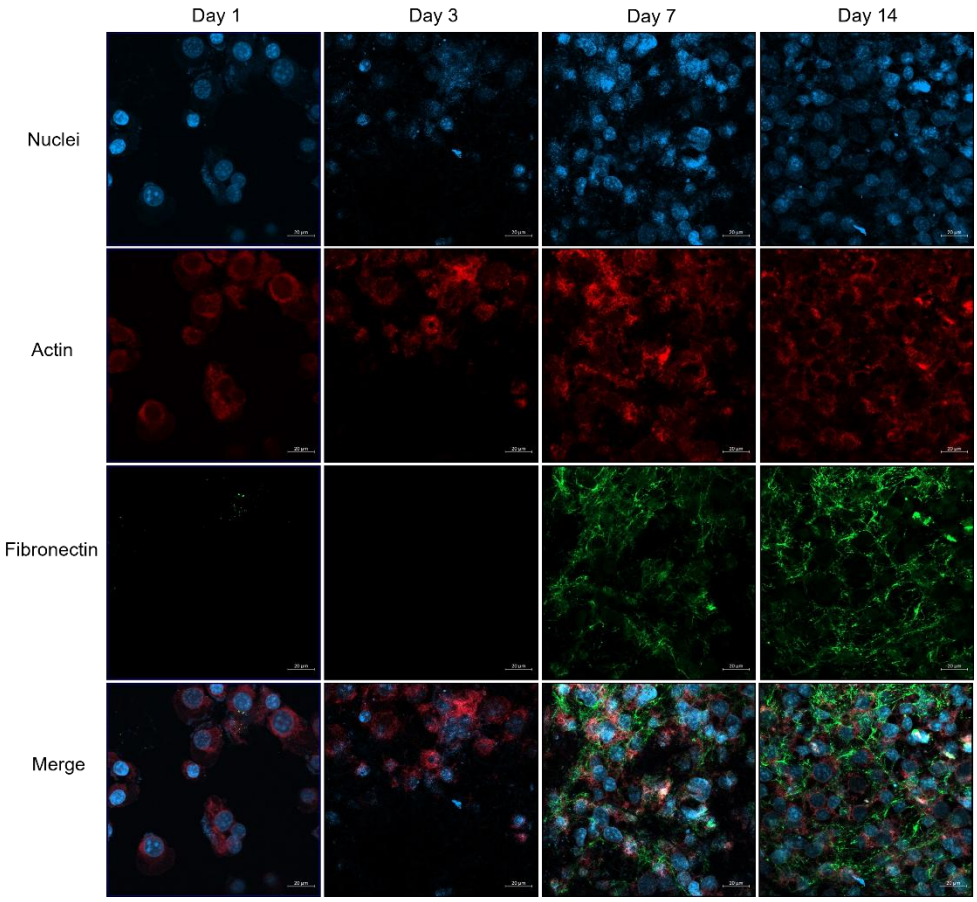

Figure 37A - Representative proliferation confocal images of L929 cells evaluated at 1, 3, 7 and 14 days of study after seeding in ePCL (blue: nuclei; red: actin; green: FN; Merge). Scale bars correspond to 20 μm.

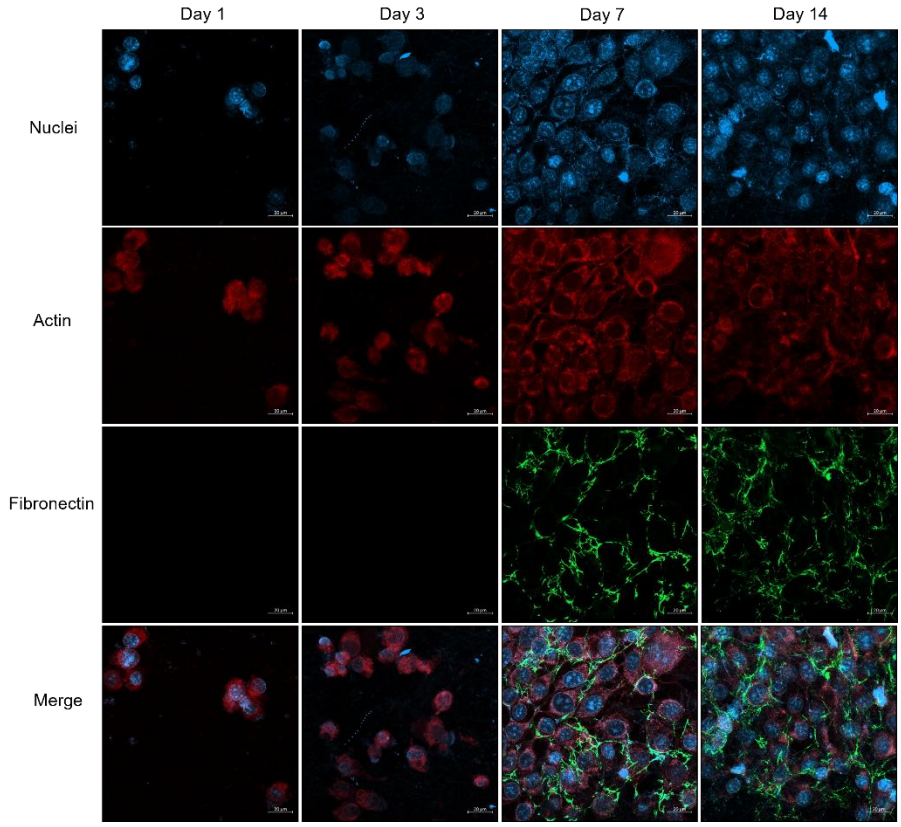

Figure 38A -Representative proliferation confocal images of L929 cells evaluated at 1, 3, 7 and 14 days of study after seeding in m_ePCL (blue: nuclei; red: actin; green: FN; Merge). Scale bars correspond to 20 μm.

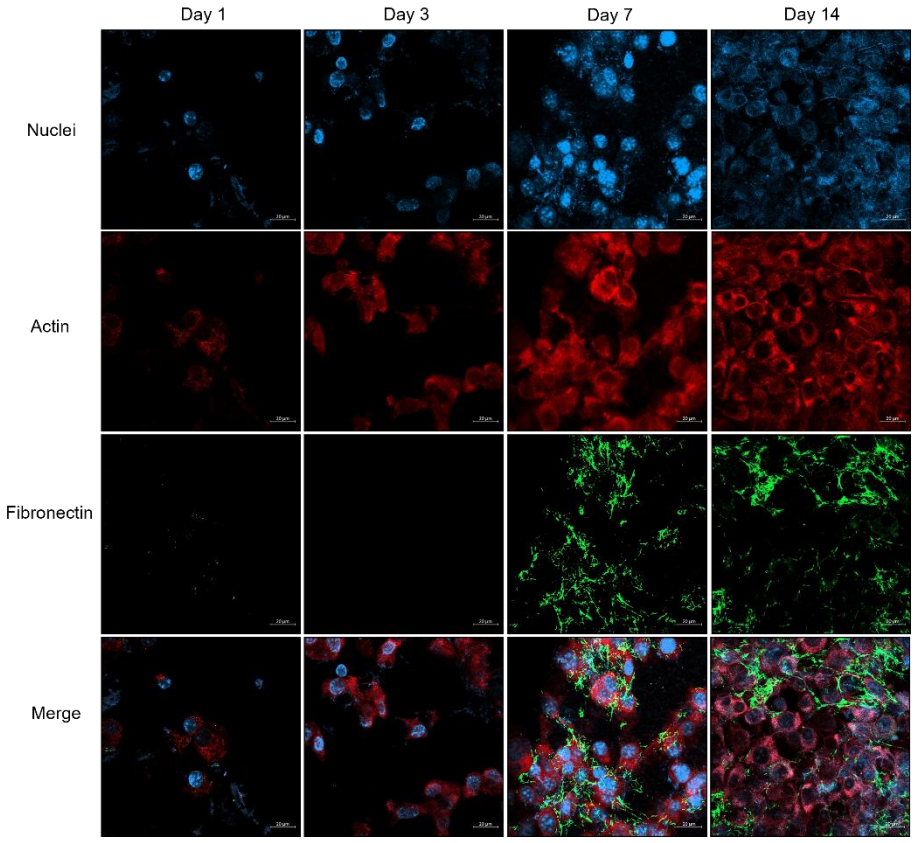

Figure 39A - Representative proliferation confocal images of L929 cells evaluated at 1, 3, 7 and 14 days of study after seeding in m_ePCL_CS0.05 (blue: nuclei; red: actin; green: FN; Merge). Scale bars correspond to 20 μm.

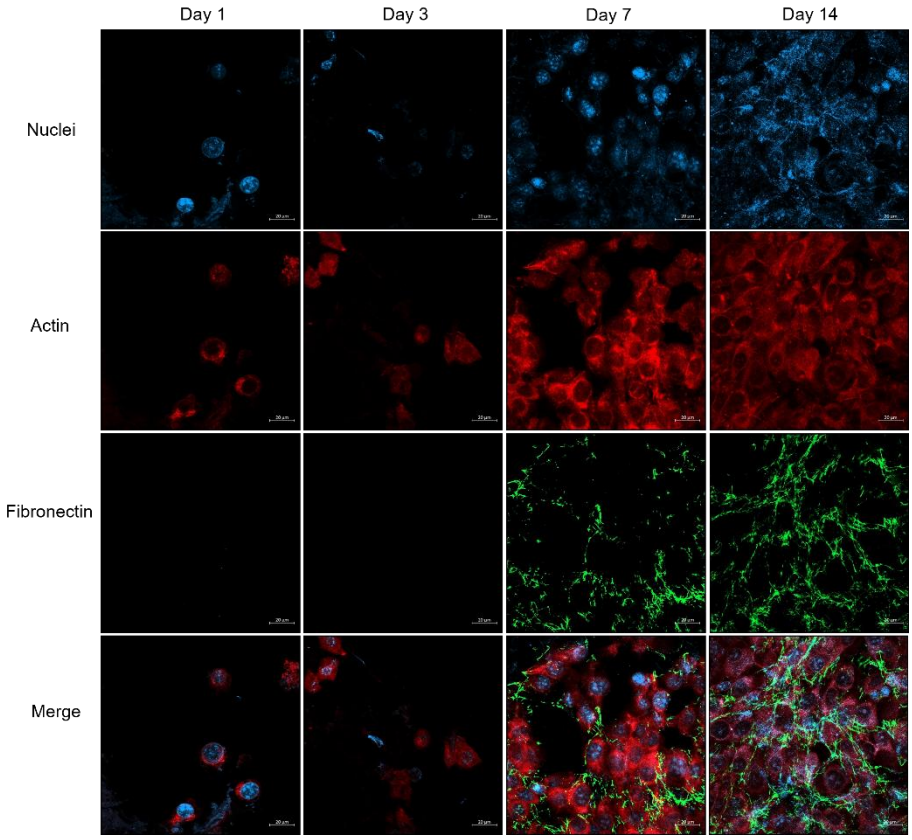

Figure 40A- Representative proliferation confocal images of L929 cells evaluated at 1, 3, 7 and 14 days of study after seeding in m_ePCL_CS0.1 (blue: nuclei; red: actin; green: FN; Merge). Scale bars correspond to 20 μm.

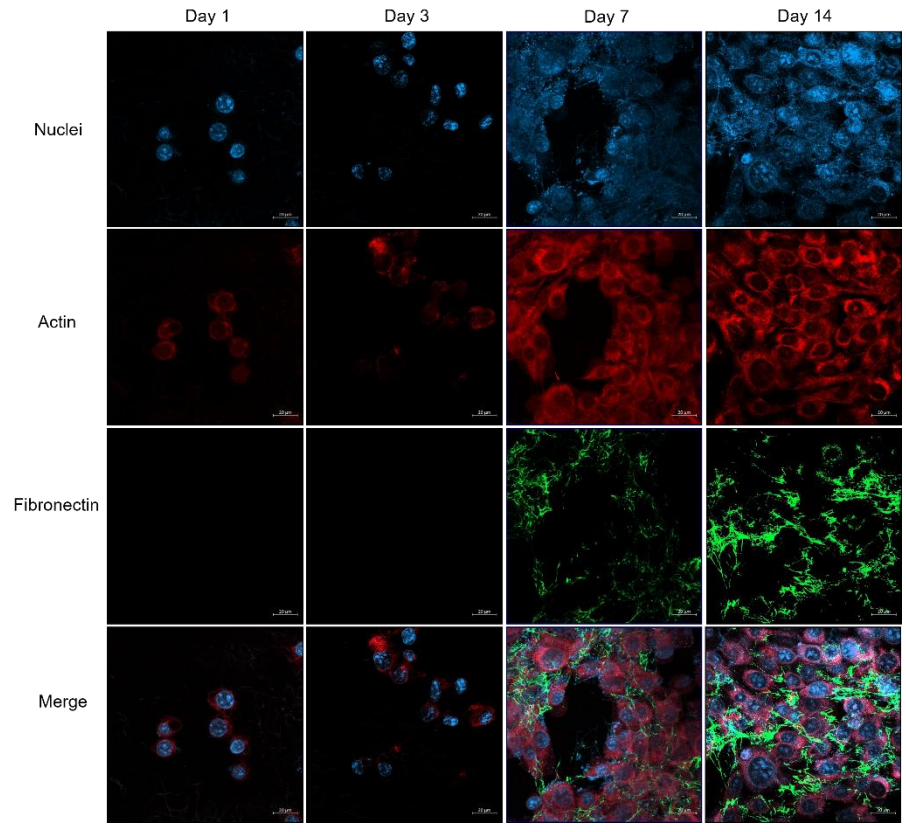

Figure 41A - Representative proliferation confocal images of L929 cells evaluated at 1, 3, 7 and 14 days of study after seeding in m_ePCL_CS0.5 (blue: nuclei; red: actin; green: FN; Merge). Scale bars correspond to 20 μm.

Appendix B

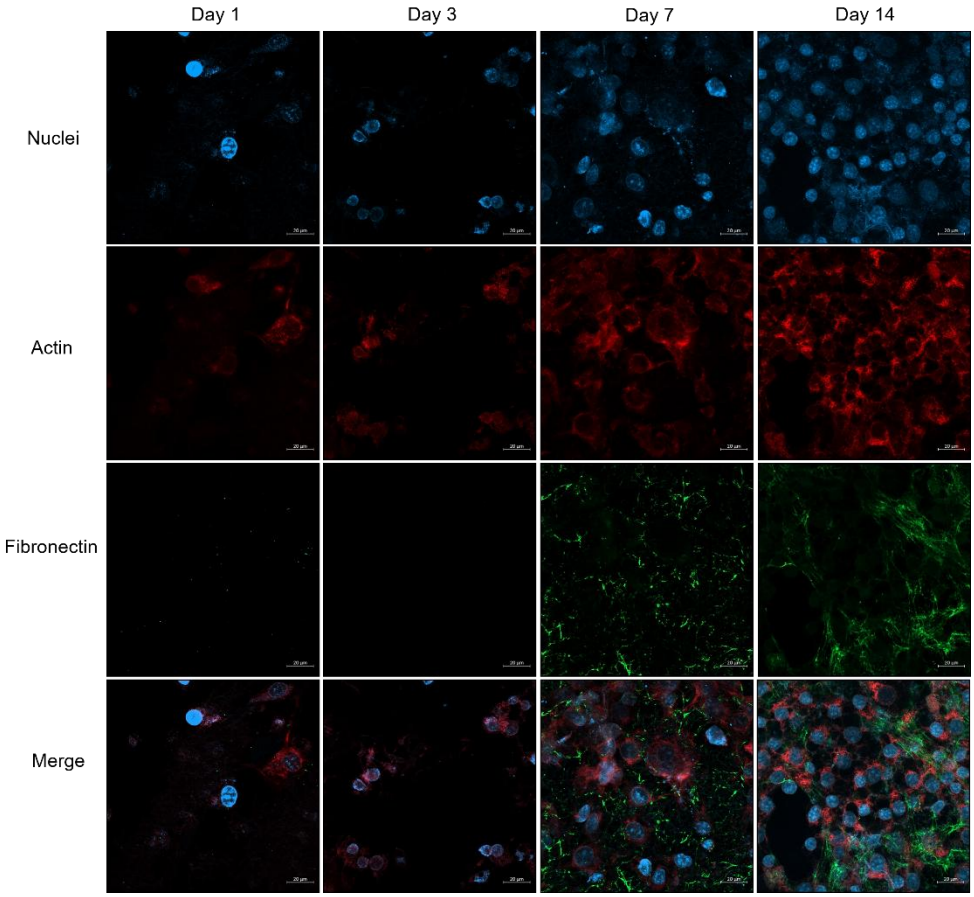

Figure 42B - Representative proliferation confocal images of L929 cells evaluated at 1, 3, 7 and 14 days of study after seeding in m_ePCL_Gel0.1 (blue: nuclei; red: actin; green: FN; Merge). Scale bars correspond to 20 μm.

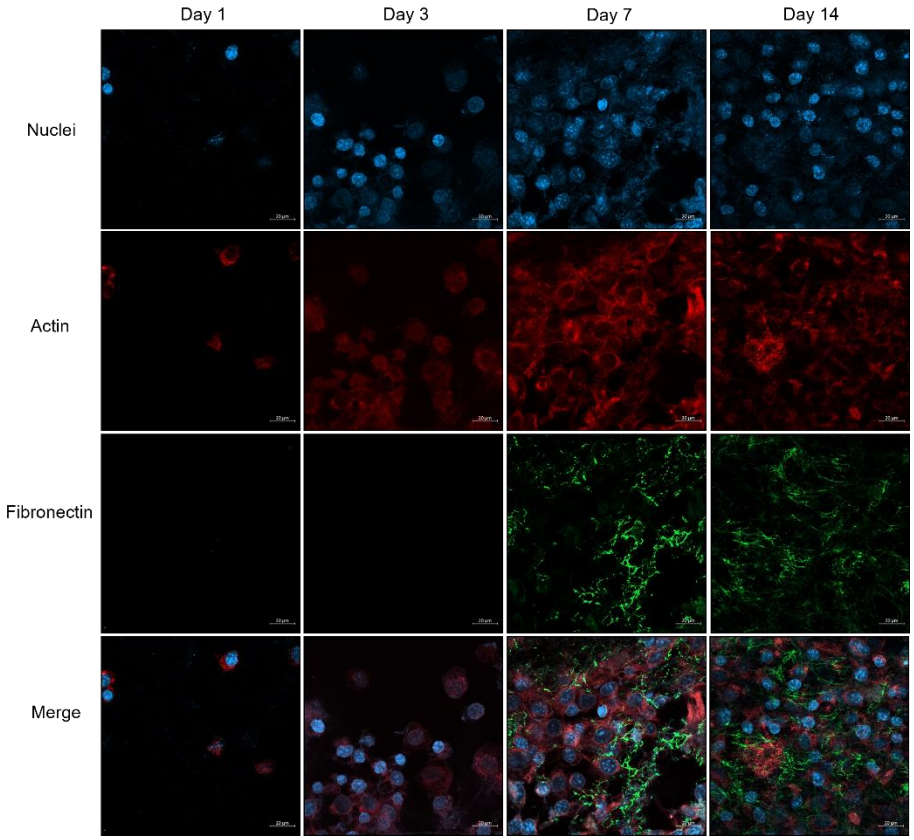

Figure 43B - Representative proliferation confocal images of L929 cells evaluated at 1, 3, 7 and 14 days of study after seeding in m_ePCL_Gel0.5 (blue: nuclei; red: actin; green: FN; Merge). Scale bars correspond to 20 μm.

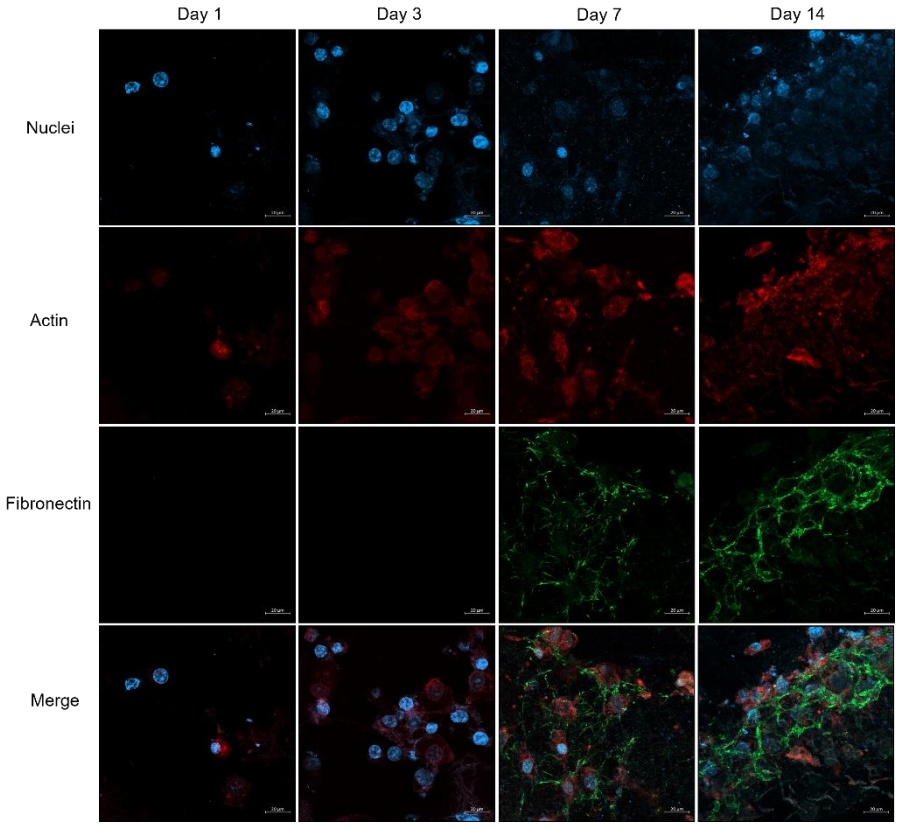

Figure 44B- Representative proliferation confocal images of L929 cells evaluated at 1, 3, 7 and 14 days of study after seeding in m_ePCL_Gel1 (blue: nuclei; red: actin; green: FN; Merge). Scale bars correspond to 20 μm.

Appendix C

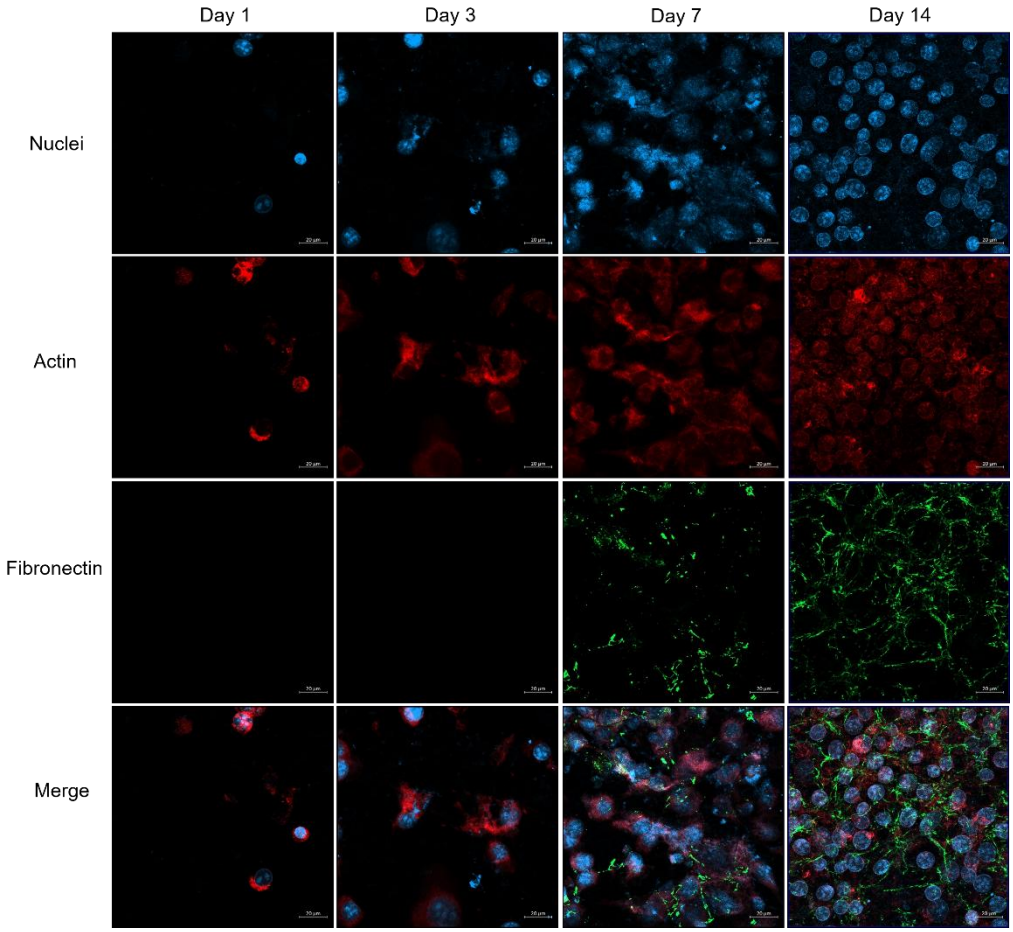

Figure 45C - Representative proliferation confocal images of L929 cells evaluated at 1, 3, 7 and 14 days of study after seeding in m_ePCL_Arg0.5 (blue: nuclei; red: actin; green: FN; Merge). Scale bars correspond to 20 μm.

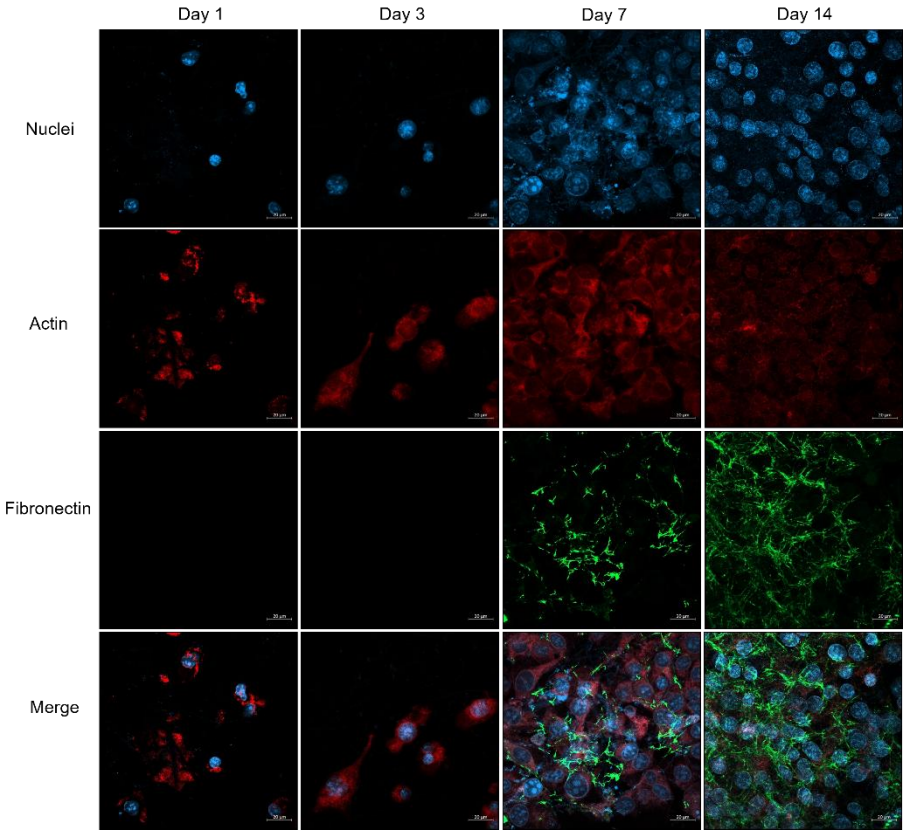

Figure 46C - Representative proliferation confocal images of L929 cells evaluated at 1, 3, 7 and 14 days of study after seeding in m_ePCL_Arg1 (blue: nuclei; red: actin; green: FN; Merge). Scale bars correspond to 20μm.

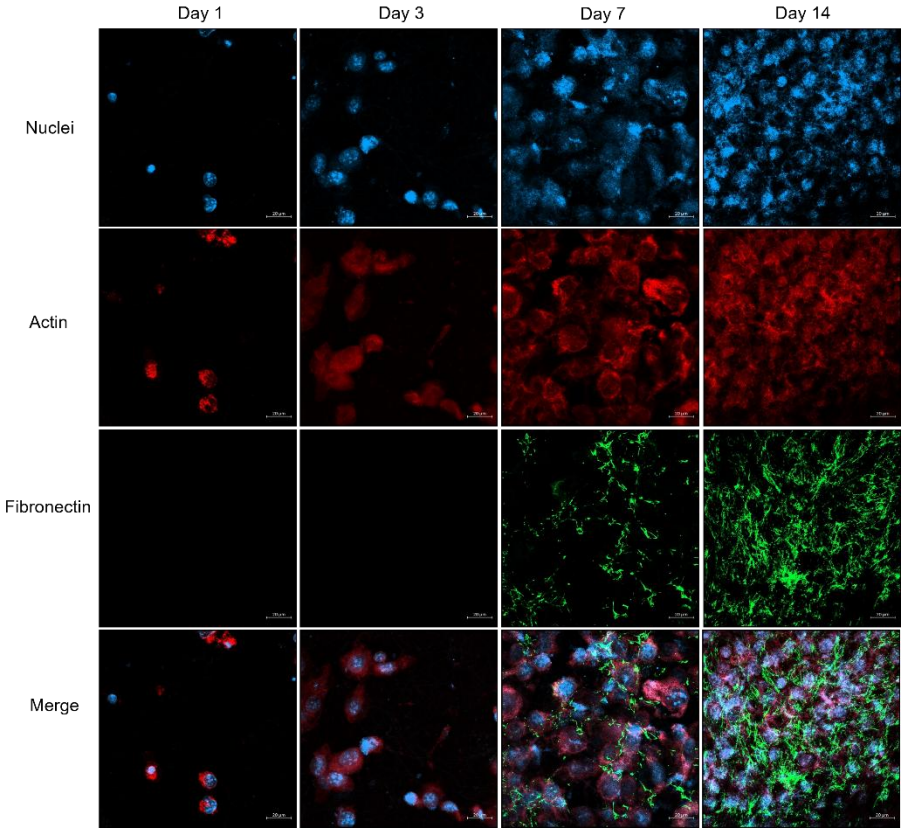

Figure 47C -Representative proliferation confocal images of L929 cells evaluated at 1, 3, 7 and 14 days of study after seeding in m_ePCL_Arg2 (blue: nuclei; red: actin; green: FN; Merge). Scale bars correspond to 20 μm.